Computational Framework for Identification of Cancerous Nodules in Prostate Based on Instrumented Palpation

Antonio Candito

Submitted for the degree of Doctor of Philosophy

Heriot-Watt University

School of Engineering and Physical Sciences

September 2019

Abstract

The interplay between engineering and medical research plays a major role in advancing the healthcare technologies. Novel medical devices have been developed to improve the diagnosis and treatment plans for patients with pathological conditions such as prostate cancer (PCa). In this context, in silico modelling has been a valuable tool as it is complementary to traditional trial-and-error approaches, particularly in the area of nodule identification in soft tissue. The goal of this thesis is to develop a computational framework of detecting and characterizing the presence of PCa, based on instrumented probing. The proposed methodologies involve Finite-Element simulations, inverse analysis and probability-based methods, using models reconstructed from medical imaging and histological data. The proposed methods are later validated using experimental measurements from instrumented probing on *ex-vivo* prostates. It is expected that the in-silico framework can serve as a complementary tool to the medical devices and to improve the effectiveness of current methods for early PCa diagnosis.

ACKNOWLEDGEMENTS

I would like to thank my Supervisors Dr. Yuhang Chen and Prof. Robert L. Reuben for the opportunity given of joining Heriot-Watt University as a Phd student. They guided me with patience from day one until the finish of the thesis providing continuous support and valuable advices. The guidance was not just about the progress for the project, however, they helped me in becoming a more mature and responsible person.

I would like to thank the collaborators Dr. Steven Hammer (Heriot-Watt University, Edinburgh, UK), Dr. Daniel W. Good and Prof. S. Alan McNeill (Western General Hospital, NHS Lothian, Edinburgh, UK). They supported the research project providing experimental data, biomedical images and suggestions for improving the achievements.

I am grateful to Heriot-Watt University who awarded to me the James-Scott Scholarship. The doctoral thesis without their support could not have been carried out. I would like to thank the Annual Fund who awarded to me a grant that I used for attending international conferences.

In the past three years, I shared the office with wonderful people. Therefore, I would like to thank the colleagues Javi, Ben, Jess, Solenn and Frank. Since day one they gave me many suggestions for the research project and life as a Phd student. I had the opportunity to know them also outside the office where we shared fantastic moments all together.

I would like to thank my friends Markos and Davide who helped for the improvement of the figures and images in the thesis.

I had the opportunity to meet many people at the Heriot-Watt University and in Edinburgh over my time as my Phd student. I would like to thank Stefano, Edwin, Micaela, Ata, my

roommates and all the other friends who helped me anytime I asked for and in many circumstances.

I would like to thank the football club Currie F.C who gave me the opportunity to know more about the fantastic community in Currie and Balerno and enjoy the training sessions and matches with the other coaches and the ‘Currie Boys’.

I would like to thank my friends in Italy who always care about me.

Last, but certainly not least, I would like to thank my family for their unconditional support.

DEDICATION

To my family.

‘’Nothing in life is to be feared, it is only to be understood. Now is the time to understand more, so that we may fear less.’’

Marie Curie

LIST OF PUBLICATIONS

Journal Publications

1. **A Candito**, J Palacio-Torralba, R L. Reuben, and Y Chen (2018). "Identification of Tumor Nodules in Soft Tissue – An Inverse Finite-element Framework based on Mechanical Characterization", *Int. j. numer. method. biomed. eng. (Submitted)*

2. **A Candito**, R L. Reuben, and Y Chen (2018). A Novel Histology based Computational Framework for Tumor Detection – Application to Prostate Cancer Diagnosis (*To be submitted).*

3. S J Hammer, O Johnson, D W Good, J Palacio-Torralba, **A Candito**, Y Chen, S Phipps, W Shu, S A McNeill, R L Reuben (2019). "Mechanical mapping of the prostate in vivo using Dynamic Instrumented Palpation; towards an in vivo strategy for cancer assessment", *Journal of Engineering in Medicine (Submitted).*

Conferences and Presentations

1. **A Candito**, J Palacio-Torralba, R L Reuben, and Y Chen. "Mechanics-based Quantitative Tissue Diagnosis", *4th IMPEE Internal Conference.* Sep 2016, Edinburgh, UK

2. **A Candito**, J Palacio-Torralba, R L Reuben, and Y Chen. "Mechanics-based Quantitative Tissue Diagnosis", *EPS 1st Year PhD poster event.* October 2016, Edinburgh, UK

3. **A Candito**, J Palacio-Torralba, R L Reuben, and Y Chen. "Mechanics-based Quantitative Tissue Diagnosis", *23th Congress of the Europeans Society of Biomechanics (ESB).* Jul 2017, Seville, Spain

4. **A Candito**, R L Reuben, and Y Chen. "Mechanics-based Quantitative Tissue Diagnosis", *Third Soft Tissue Modelling. Centre for Multiscale Soft Tissue Mechanics (SoftMech)*. Jun 2017, Glasgow, UK

5. **A Candito**, J Palacio-Torralba, R L Reuben, and Y Chen. "Mechanics-based Quantitative Tissue Diagnosis", *5th IMPEE Internal Conference.* Sep 2017, Edinburgh, UK

6. **A Candito**, J Palacio-Torralba, R L Reuben, and Y Chen. "Mechanics-based Quantitative Tumor Identification and Characterization", *Sixth National Congress of Bioengineering (GNB)*. June 2018, Milan, Italy

7. Multiscale Hierarchy and Heterogeneity in biological tissue. UK-India Education and Research Initiative *(UKIERI)* | Dec 2015, Edinburgh, UK

8. 'The Dialogues on Cancer '– between clinicians, biologists and modellers | Nov 2016, Edinburgh, UK

9. Imaging to Modelling: Workflows for Clinical Practice. Predictive Modelling for Healthcare through Maths *(POEMS)* | Jun 2016, Glasgow, UK

10. Third Soft Tissue Modelling. Centre for Multiscale Soft Tissue Mechanics *(SoftMech)* | Jun 2017, Glasgow, UK

ACADEMIC REGISTRY

Research Thesis Submission

Please note this form should be bound into the submitted thesis.

Name:	Antonio Candito		
School:	Engineering and Physical Sciences		
Version: *(i.e. First, Resubmission, Final)*	Final	Degree Sought:	Ph.D. Mechanical Engineering

Declaration

In accordance with the appropriate regulations I hereby submit my thesis and I declare that:

1. The thesis embodies the results of my own work and has been composed by myself
2. Where appropriate, I have made acknowledgement of the work of others
3. Where the thesis contains published outputs under Regulation 6 (9.1.2) these are accompanied by a critical review which accurately describes my contribution to the research and, for multi-author outputs, a signed declaration indicating the contribution of each author (complete Inclusion of Published Works Form – see below)
4. The thesis is the correct version for submission and is the same version as any electronic versions submitted*.
5. My thesis for the award referred to, deposited in the Heriot-Watt University Library, should be made available for loan or photocopying and be available via the Institutional Repository, subject to such conditions as the Librarian may require
6. I understand that as a student of the University I am required to abide by the Regulations of the University and to conform to its discipline.
7. Inclusion of published outputs under Regulation 6 (9.1.2) shall not constitute plagiarism.
8. I confirm that the thesis has been verified against plagiarism via an approved plagiarism detection application e.g. Turnitin.

* *Please note that it is the responsibility of the candidate to ensure that the correct version of the thesis is submitted.*

Signature of Candidate:	Antonio Candito	Date:	

Submission

Submitted By *(name in capitals)*:	Antonio Candito
Signature of Individual Submitting:	Antonio Candito
Date Submitted:	

For Completion in the Student Service Centre (SSC)

Received in the SSC by *(name in capitals)*:			
Method of Submission *(Handed in to SSC; posted through internal/external mail)*:			
E-thesis Submitted ***(mandatory for final theses)***			
Signature:		Date:	

ACADEMIC REGISTRY

Inclusion of Published Works

Declaration

This thesis contains one or more multi-author published works. In accordance with Regulation 6 (9.1.2) I hereby declare that the contributions of each author to these publications is as follows:

Citation details	e. g. Author 1 and Author 2, Title of paper, Title of Journal, X, XX-XX (20XX)
Author 1	Contribution….
Author 2	Contribution….
Signature:	
Date:	

Citation details	e. g. Author 1 and Author 2, Title of paper, Title of Journal, X, XX-XX (20XX)
Author 1	Contribution….
Author 2	Contribution….
Signature:	
Date:	

Citation details	e. g. Author 1 and Author 2, Title of paper, Title of Journal, X, XX-XX (20XX)
Author 1	Contribution….
Author 2	Contribution….
Signature:	
Date:	

LIST OF CONTENTS

LIST OF FIGURES

LIST OF TABLES

LIST OF ABBREVIATIONS

ANN	Artificial Neural Network
BPH	Benign Prostate Hyperplasia
CT	Computed tomography
CZ	Central Zone
DCE	Dynamic Contrast-Enhanced
DRE	Digital Rectal Examination
DWI	Diffusion-Weighted Imaging
FE	Finite-Element
FSR	Force-Resistor Sensor
iDRE	Instrumented Digital Rectal Examination
KVFD	Kelvin Voigt Fractional Derivative
LM	Levenberg-Marquardt
MIS	Minimal Invasive Surgery
mpMRI	Multiparametric Magnetic Resonance Imaging
MRE	Magnetic Resonance Elastography
MRI	Magnetic Resonance Imaging
PCa	Prostate Cancer
PET	Positron Emission Tomography
PSA	Prostate Specific Antigen
PZ	Peripheral zone
SNR	Signal-to-Noise Ratio
TRUS	Transrectal Ultrasound
TZ	Transitional Zone
US	Ultrasound

Chapter 1

Introduction

Contents

1.1 Motivation

Biomedical Engineering is a discipline which has the aim of combining the design and problem-solving skills of engineering with medical and biological sciences to advance healthcare treatment, including diagnosis, monitoring and therapy. Nowadays, the impact of the biomedical engineering in the scientific communities increases significantly with the strong development of the capacity of computational modelling [1]. However, the understanding of the mechanical bahaviour of biological tissues and their interaction at diverse scale levels is still a challenge. The reasons mainly reside in the inability or impracticality of carrying out experiments especially in many in vivo scenarios. In contrast, computational modelling has the advantage of overcoming the aforementioned problems, in somewhat simplified but representative scenarios which would eventually help the experimental efforts. In the past decade, computational modelling has been exploited in research areas as biomechanics, biomaterial, artificial organs and medical

devices [2]–[5]. One example of using computational modelling in the biomechanics and medical device research areas will be validated in the thesis.

Diagnosing prostate cancer (PCa) is not a trivial task. The current diagnostic techniques for PCa include the blood test for Prostate-Specific Antigen (PSA), Digital Rectal Examination (DRE), medical imaging methods including Magnetic Resonance Imaging (MRI) and transrectal ultrasound (TRUS) and biopsy [6]. The PSA is a protein which is produced by normal cells in the prostate and it raises due to the presence of cancer [7]. However, the test shows low specificity [8]. The DRE consists of palpating the posterior surface of the prostate through the rectum wall to detect abnormalities, a sign of PCa nodules [9]–[11]. However, the method provides a qualitative outcome, and it relies highly on the practitioners' experience [12], [13]. MRI is frequently used for PCa detection and treatment planning. However, the method is incapable of detecting PCa nodules which are smaller than 10mm [14]. TRUS, although providing quantitative imaging for the clinicians [15], [16], it has certain limitation in distinguishing between PCa nodules and benign condition such as benign prostatic hyperplasia (BPH) [17]. Biopsy allows the examination of the sample tissue from the prostate, however it is vulnerable to a high probability of false negative due to the random nature of sample locations [18]. To complement to the current early screening methods of PCa, medical devices that could deploy instrumented DRE (iDRE) have been developed, with an aim of providing quantitative analysis to the PCa identification while maintaining the non-invasive nature of the palpation procedure [19].

In addition to the development of the iDRE devices, there is a lack of a diagnostic framework, either mathematical or numerical, to interpret and make sense of the palpation feedback data. The palpation feedback, either static or dynamic, is heavily influenced by the cancer heterogeneity and the inter-patient differences such as the diverse anatomical

structures and the mechanical properties of the healthy tissue [20], [21]. In addition, the heterogeneities in the tissue structure could significantly increase the uncertainty in how the palpation data can be interpreted. Therefore, a mathematical and/or numerical framework that is capable of making sense of the palpation data with predictive capability is urgently needed. This thesis will address exactly this.

1.2 Thesis scope and structure

The main goal of this thesis is to develop a computational framework which is able to detect and characterize cancerous nodules in prostate and compatible to instrumented palpation device either *ex-vivo* or *in-vivo*, without a *priori* knowledge of the physiopathological condition of the patients.

Specifically, the objectives of the thesis include

- To develop a novel computational framework for evaluating force feedback and detecting cancerous nodules, without a *priori* knowledge of the tissue composition;
- To perform a sensitivity analysis for assessing the influence of the cancer heterogeneity in the mechanical response of prostate tissue;
- To develop a predictive model based on a probabilistic approach for identifying cancerous nodule(s) and estimating its position, depth, dispersion and volume within a confidence interval;
- To evaluate the accuracy of the predicting model in classifying between cancerous and healthy prostate tissues and estimating the nodule depth, size and geometry, based on a large volume of histological data-set;

- To validate the novel predictive model using the *ex-vivo* experimental measurements on whole prostate using iDRE devices and assess the sensitivity and specificity of the proposed method.

The rest of this thesis is structured to elaborate how these objectives are met, as follows:

Chapter 2: Mechanics-based Quantitative Tissue Diagnosis and Nodule Identification: State of the Art

This chapter contains a literature survey of all major topics relevant to the thesis, including i) a review on the tissue morphology and microstructure given rise by the presence of physiopathological conditions such as cancer; ii) a description of the biological tissues mechanical characterization exploiting non-linear elasticity theory and modelling; iii) a review on the limitations in cancer detection of current diagnostic techniques for various types of soft tissues; iv) a justification of the need of developing a novel diagnostic framework for identifying and characterizing the presence/absence of cancer in soft tissue based on mechanical palpation measurements; v) a review of the challenges which the thesis will address; and finally vi) a summary of the potential impact of the thesis.

Chapter 3: Identification of Tumor Nodules in Soft Tissue – An Inverse Finite-Element Framework based on Mechanical Characterization

In this chapter, a novel computational diagnostic framework is developed for detecting the presence of a tumor nodule in soft tissue using quasi-static palpation. The methodology relies on solving an inverse FE problem with the purpose of estimating the volume of the examined prostate (target). Therefore, an error function between the reaction force values obtained by probing the target and the synthetic model is minimized. The methodology has been hypothesized and later validated using simplified 2D models.

A sensitivity analysis for quantifying the accuracy of the method for a diverse range of initial guesses and number of parameters is performed. To validate the model, the methodology is tested using a feasibility study where a prostatic tissue is reconstructed from an MRI image with and without the presence of a tumor nodule. The results show how the estimated target volumes, which are obtained performing multiple probing depths, can be used as an indicator for tumor nodule detection without the a *priori* knowledge of its presence in the soft tissue. A sensitivity analysis for evaluating the influence of the cancer heterogeneity, when the methodology is applied, will be investigated in the next chapter.

Chapter 4: Sensitivity Analysis of Inverse FE Framework

This chapter further carried out the sensitivity analysis, regarding the influence of heterogeneity in tumor nodule in the instrumented palpation procedure when the novel computational framework developed in Chapter 3 is applied. The inverse FE method is tested using a simplified 2D target model characterized by the presence of tumor nodule with diverse combinations of size, depth and stiffness. Therefore, the limits in the detectability are quantified as a function of the nodule parameters such as size, depth and stiffness ratio. The method is validated using a feasibility study where MRI-reconstructed prostate models with cancerous nodules are used. The cancerous nodules have diverse ranges of location, depth, geometry and size in the prostate slices. The results confirm the capability of the framework in detecting the presence of cancerous nodule using the estimated target volumes and multiple probing depths without a priori knowledge of the physiopathological conditions of the patient. However, the detectability depends on the interplay between the size, depth and stiffness of the cancerous nodule. Decoupling the effect of those parameters using elasticity as biomarker remains challenging. Therefore, a probabilistic approach will be proposed in the following chapter.

Chapter 5: Probability-based Predictive Methods for PCa Nodule Identification

In this chapter, a predictive model based on a probabilistic approach is developed for tumor identification purpose. The clinical outcomes are the identification of the presence/absence of tumor nodule and the estimation of the position, depth, dispersion and suspicious area of the cancerous regions in the soft tissue. The proposed method utilises a probabilistic approach in order to decouple the influence of the nodule parameters, i.e. size and depth, in the force feedback. The prostate is probed first at several probing points so that a reaction force profile is obtained. An identifiable peak in the force profile occurs due to the presence of one or more cancerous nodules. A large dataset of force profiles is generated using a simplified model with a tumor nodule of random position, depth and size. The statistical analysis of the data shows how the shape of the peak is sensitive to the nodule depth and size. Therefore, the features of the peak are exploited as a diagnostic index. There are some limitations in the proposed model which are also identified and quantified. The capability of the method is first tested using synthetic reaction force profiles generated from finite element modelling of random prostate models. The prediction shows promising accuracy in the nodule features estimation. However, the simplified 2D FE models may not represent, in reality, the cancer heterogeneity and the diverse anatomical details of the prostates. Therefore, the proposed model will be further tested using prostate models reconstructed from prostatic histological slices in the next chapter.

Chapter 6: Validation of Predictive Methods – Stage 1: Models Reconstructed from Histological Images and FE-Simulated Instrumented Probing

This chapter further explores the capability of the predictive model proposed in Chapter 5. A clinical study of 30 patients, who are diagnosed with PCa and treated with radical proctectomy, provides a large data-set of histological examinations where the outlines of the cancerous nodules are underlined by a consultant pathologist. They are converted into FE models where the outlines of the prostate and cancerous nodules are preserved. The reaction force profiles are obtained by probing the posterior surface of the prostate models. A peak occurs as consequence of the presence of a stiffer nodule and the predicted model provides a diagnosis based on the characterization of the peak shape. The sensitivity and specificity are evaluated at three different levels, i.e. patient, slice and nodule levels. A quantification of the limitations of the predicted model in the cancer identification is evaluated. The statistical analysis of the accuracy in predicting the nodule(s) location and suspicious area(s) is carried out. The conclusions suggest a promising sensitivity and specificity of the predicted model at the patient and slice scale. However, it is still challenging detecting cancerous nodule in the anterior surface of the prostate and when the tumor volume fraction is too small to have detectable influence in the stress field. This model will be further validated, and its capability explored in the next chapter using *ex-vivo* experimental data.

Chapter 7: Validation of Predictive Methods – Stage 2: Measurements on Ex-vivo Prostate

In this chapter, the proposed model is assessed using *ex-vivo* experimental measurements, where a palpation device is deployed on the posterior surface of the prostate following the removal of the prostate in a radical proctectomy surgery. The proposed model is applied to the measurement data, specifically, to the peak of the force profile. The results show that the proposed method is capable of predicting the presence and location of the cancerous nodules with promising accuracy. Similar levels of sensitivity and specificity are found, consistent with the results shown in Chapter 6. Therefore, the proposed model could be used as a computational tool for PCa identification and characterization, complementary to the iDRE measurements, with the ultimate aim of improving the diagnosis accuracy and may serve to decrease the number of unnecessary biopsies.

Chapter 8: Looking back / working forward

In this chapter, the main conclusions obtained in this thesis are summarized, and the contribution and impact of the research are highlighted. The limitations of the current work are also discussed. Furthermore, a research proposal is suggested as future work.

Chapter 2

Mechanics-based Quantitative Tissue Diagnosis and Nodule Identification: State of the Art

Contents

2.1 Summary

Section title	Objectives
2.2 Microstructure heterogeneity in soft tissue	Explore the variation in the microstructure of the biological soft tissues due to the presence of physiopathological conditions and how this influence their mechanical behaviour
2.3 Mechanical characterization and modelling of soft tissue	Review the material properties and the models exploited for characterizing the biological soft tissues particularly the hyperelastic theory and the prostatic tissue
2.4 Tumour detection – current diagnostic techniques	Survey of the diagnostic techniques exploited for detection of PCa and their limitations in PCa diagnosis
2.5 Instrumented palpation– using elasticity as biomarker	Illustrate the characteristics of the instrumented palpation devices and their advantages in the tumour detection using mechanical probing
2.6 Computational framework for diagnosis purpose based on instrumented palpation	Review the diagnostic frameworks developed in the literature for identifying and characterizing tumor nodule(s) in soft tissue based on palpation; their limitations in providing an accurate detection and diagnosis for the patients
2.7 Concluding remarks	Identify the challenges that this thesis will address

2.2 Microstructure heterogeneity in soft tissue

All biological tissues have heterogeneous and hierarchical microstructures [22]. Moreover, the microscopic morphology of tissue can be varied by the presence of certain pathological conditions. As a result, their mechanical properties may change, across both spatial (nm ~ m) and temporal (seconds ~ years) length scales.

There are numerous experimental evidence which emphasized how the mechanical properties of soft tissue, e.g. elasticity, can be varied due to the presence of, for example, solid tumour or other pathological conditions. In the breast tissue, when breast cancer occurs, there occurs solid lesions in the microstructure which are usually stiffer than the healthy counterpart [23], [24].In the recently published studies has been shown that these different elasticity moduli help differentiate between healthy, benign and malignant solid breast lesions [25], [26]. For the brain tissue, evidence has shown that the tissue morphology can be greatly affected by such conditions as multiple sclerosis [27]. Furthermore, Chauvet et al. have proven how elasticity can be exploited as a biomarker to distinguish between tumor and benign brain tissue [28]. In addition, the fibrosis, could vary the mechanical response of the liver. Physiologically, fibrosis acts to deposit connective tissue, which can interfere with or totally inhibit the normal architecture and function of the underlying organ or tissue [29]. Therefore, the diseases can be identified measuring the variation of the elasticity values [30]. For human artery, it has been shown that the mechanical properties and distensibility of the arteries can vary due to ageing as the vessel is affected by the decrease of elastin leading to a reduced load bearing capacity [31], [32]. Furthermore, the stiffness of the artery changes too due to pathological condition as the atherosclerosis [33]. The microstructure of the muscles presents (hyper)-elastic components and Basford et al. [34] described how the increasing of the stiffness in the muscles is caused by neuromuscular disease. Bensamoun et al. [35] described how

stiffness measurements can be an index for the characterization in the renal damage in order to detect malignant tumors.

The thesis is focused mainly around the topic of detection and characterization of the prostatic tissue and PCa, which presents an excellent exemplar system for studying the tissue mechanics and its application in clinical cancer diagnosis. The mechanical properties could vary when a benign condition occurs, for instance an inflammation, calcification or when there is an enlargement of the prostatic tissue, benign condition called Benign Prostate Hyperplasia (BPH) [36], [37]. Moreover, the mechanical response could be significantly altered due to the presence of PCa. Fig. 1 compares two prostatic histological slices. In Fig. 1a the prostatic tissue is healthy so that a normal morphology is showed. There are visible gland units (characterized by lumens and epithelial cells) which are surrounding by the stroma. The lumens (or acini) are small, fluid-filled cavities surrounded by epithelial cells. There are approximately half a million acini in the prostate. The acini are lined by secretory epithelial cells. Each cell secretes a small amount of fluid which is about 20% of the ejaculatory volume. The prostatic stroma is composed of collagen fibres (type I), fibroblast and smooth muscle [38]. The size of the lumens for a healthy prostate can vary between 15000 and 18000 μm^2 [39]. However, Fig. 1b shows a prostatic tissue with cancer as the lumens are smaller and distance between each other increased and replaced by the stroma tissue [38], [40]. The size of the lumens for tissues which show presence of PCa can drop to as low as 7000 μm^2 [39]. In Fig. 1c is showed an example of PCa which is more aggressiveness of the one in Fig. 1b. In this case, the lumens been filled with cancer epithelial cells and the stroma almost disappears by the prostatic structure composition [41]. Clinically, PCa is classified using the Gleason Score system [42]. In the system, the tissue is classified into five grades, numbered 1 through 5. Gleason grade characterizes tumor differentiation, i.e. the degree of tumor which

resembles to a normal tissue. Grade 1 corresponds to well-differentiation tissue, while grade 5 corresponds to poorly differentiated tissue and indicates a more aggressive cancer. In conclusion, when PCa occurs, there is a stroma reaction which causes an increasing of collagen deposition in the stroma surrounding the prostate. When the cancer becomes more aggressive, the epithelial cells replicate in an uncontrolled way so that the regular glandular structure no longer exist, replaced by a highly irregular structure with little sign of prostatic glands. More importantly, these morphology variations such as the decrease of the acini, replaced by the stroma and/or the cancer epithelial cells at various cancer stages, may lead to increase in the prostate elasticity [39]. For instance, such changes in the acini size would influence the amount of fluid within the prostatic tissue. Therefore, the variation of the acini distribution, the amount and the size could be closely related to the variation of the mechanical properties. Palacio-Torralba and co-workers [43] quantified the relationship between tissue microstructure and its apparent mechanical properties. The stiffness values were higher for a cancerous tissue compared with the non-cancerous tissue. As hypothesized, the acini area in the cancerous tissue is less, smaller and less recognisable compared with the non-cancerous tissue. Therefore, the mechanical properties of the prostate tissue may be exploited as a biomarker index to help identify the PCa nodules in the prostate. This will be further discussed below in the following sections.

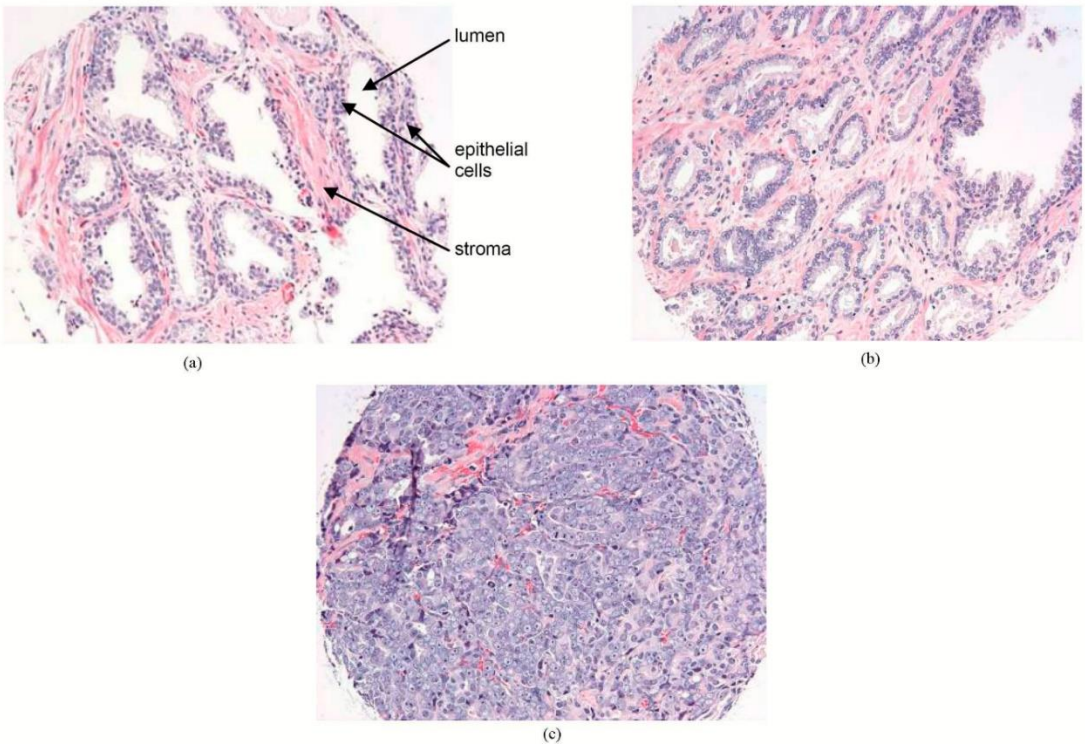

Fig. 2-1. Histological prostatic slices with which describe the morphology variation in the microstructure due to the presence of cancer. The tissue samples were stained using H&E. The images were captured using a light microscope at 20x magnification. 1a) Healthy tissue characterized by normal gland units. 2b) Prostatic tissue characterized by the presence of PCa with Gleason grade 2. The lumens are smaller due to the increment of the stroma tissue. 2c) PCa with Gleason score 5 where the normal arrangements of the gland units are lost due to an increment of the cancer cells density [44].

2.3 Soft tissue mechanical characterization and modelling

The knowledge of mechanical behaviour of biological tissues have been utilised in clinical practice for many purposes, including surgical planning, design and optimization of prothesis implant or a point-of-care medical devices, and diagnostic methods for tissues such as prostate [45]–[48]. However, the biological tissues are non-linear, heterogeneous, anisotropic, time-dependent materials and the characterization of their mechanical behaviour is not a trivial task.

2.3.1 Non-linearity of the biological tissue under large displacement

Significant experimental results showed that the elasticity alone is not adequate to fit the stress-strain relationship obtained testing mechanically a biological tissue. In order to characterise the non-linear response of the tissue, as illustrated in Fig. 2, particularly the responses under large strain deformation, the theory of the nonlinear elasticity was developed. The pioneers of such theories include Fung, Veronda and Westmann [49], [50], who demonstrated the theoretical basis for characterizing the non-linear elasticity in elastomers, which show similar characteristics with the biological tissue. Their theories were later used in the applications of soft tissue mechanics [51]. Such nonlinear behaviour, often referred to as 'hyper-elasticity', is commonly seen in most soft tissues such as prostate, breast and liver [52].

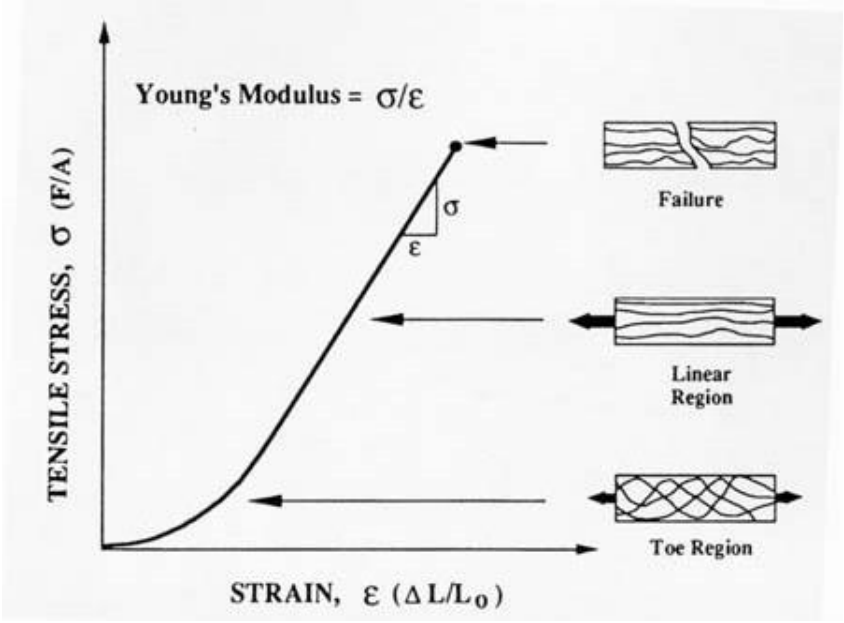

Fig. 2-2. Mechanical behaviour of the cartilage solid matrix undergoing to uniaxial test. The stress and strain values show a non-linear elastic response which is determined by the amount of solid matrix and crimp of collagen in the matrix[1].

[1] http://sites.bsyse.wsu.edu/pitts/be120/Handouts/animal%20tssue%20descriptions%20and%20mechanical%20proprties.htm

2.3.2 Strain energy functions for hyperelastic materials

Hyperelastic materials rely on strain energy functions (U) of the deviatoric strain invariants $\bar{I}_1, \bar{I}_2 \; and \; \bar{I}_3$ as described below

$$\bar{I}_1 = tr(\boldsymbol{B}) = \bar{\lambda}_1^2 + \bar{\lambda}_2^2 + \bar{\lambda}_3^2 \tag{2.1}$$

$$\bar{I}_2 = \frac{1}{2}\left(\bar{I}^2{}_1 - tr(\boldsymbol{B}^2)\right) = \bar{\lambda}_1^2\bar{\lambda}_2^2 + \bar{\lambda}_1^2\bar{\lambda}_3^2 + \bar{\lambda}_2^2\bar{\lambda}_3^2 \tag{2.2}$$

$$\bar{I}_3 = \det(\boldsymbol{B}) = \bar{\lambda}_1^2\,\bar{\lambda}_2^2\,\bar{\lambda}_3^2 \tag{2.3}$$

$$\boldsymbol{B} = \boldsymbol{F} \cdot \boldsymbol{F}^T \tag{2.4}$$

where λ_i are the principal stretches, B is the left Cauchy-Green deformation tensor and F is the deformation gradient.

Assuming an isotropic, homogenous and hyperelastic material [53], the constitutive equation, for finite strain, is defined as follows

$$\sigma = \frac{2}{\bar{I}_3}\left[\left(\frac{\partial U}{\partial \bar{I}_1} + \bar{I}_1\,\frac{\partial U}{\partial \bar{I}_2}\right)\boldsymbol{B} - \frac{\partial U}{\partial \bar{I}_2}\,\boldsymbol{B}\cdot\boldsymbol{B} - \bar{I}_3\,\frac{\partial U}{\partial I_3}\,I\right] \tag{2-5}$$

where σ is the Cauchy stress tensor and I is the identity matrix. A range of strain energy models have been developed with the aim of characterizing the hyperelasticity of biological soft tissue and they will be briefly introduced below.

- The neo-Hookean model [54] can predict the mechanical behaviour of material such as plastics and rubber-like substances, which show a non-linear stress-strain behaviour undergoing large deformations. However, the model only shows high accuracy for predicting the increase in the modulus of the material within a strain less than 20%. Furthermore, the method shows poor accuracy in predicting the mechanical behaviour of hyperelastic materials undergoing biaxial stress of states.

$$U = C_1(\bar{I}_1 - 3) + \frac{1}{D_1}(J-1)^2 \tag{2.6}$$

where C_1 represents the hyperelastic parameter of interest, J is the total volume ratio, and D_1 is a compressibility coefficient.

$$\bar{I}_1 = J^{-\frac{2}{3}} I_1 , \quad C_1 = \frac{\mu_0}{2} , \quad D_1 = \frac{2}{K_0} \tag{2.7}$$

where I_1 is the first strain invariant of the left Cauchy-Green deformation tensor, μ_0 is the initial shear modulus and K_0 is the initial bulk modulus. For incompressible materials the function is dependent by only the hyperelastic parameters.

- The Mooney-Rivlin [55], [56] model shows high accuracy in predicting the nonlinear behaviour of isotropic rubber-like material. The model can predict the non-linear behaviour for deformations which are higher in comparison with the limits mentioned for the neo-Hookean model. Furthermore, the strain energy function contains a second invariant which guarantees an improvement in the prediction of the mechanical behaviour for material undergoing biaxial and shear stress of states.

$$U = \frac{C_1}{2}(\bar{I}_1 - 3) + \frac{C_2}{2}(\bar{I}_2 - 3) + \frac{1}{D_1}(J-1)^2 \tag{2.8}$$

$$\bar{I}_2 = J^{-\frac{4}{5}} I_2 , \quad C_1 + C_2 = \mu_0 \tag{2.9}$$

where I_2 is the second strain invariant of the left Cauchy-Green deformation tensor, C_1 and C_2 are the material constants.

- The Ogden model [57] is used to describe the non-linear stress-strain behaviour of complex materials such as rubbers, polymers and biological tissues. From experiments, to model rubber at strain which is higher 70%, the Ogden model shows a good accuracy in predicting the non-linearity of the material in a higher

strain range in comparison with the accuracy achieved using the neo-Hookean and Mooney-Rivlin models. In the Ogden material model, the strain energy density is expressed in terms of the principal stretches.

$$U = \sum_{i=1}^{N} \frac{2\mu_i}{\alpha_i^2} \left(\bar{\lambda}_1^{\alpha_i} + \bar{\lambda}_2^{\alpha_i} + \bar{\lambda}_3^{\alpha_i} - 3\right) + \sum_{i=1}^{N} \frac{1}{D_i} (J-1)^{2i} \tag{2-10}$$

$$2\mu = \sum_{1}^{N} \mu_i \alpha_i \tag{2.11}$$

where N, μ and α are material constants.

- The Arruda-Boyce model [58] is based on the statistical mechanics of a material characterized by a representative network structure. The primary element of the network is a unit cell containing eight chains. The chains are located along the diagonals of the cell. The eight chains model accurately captures the cooperative nature of the network deformation of a soft material. For an incompressible material the strain energy function of the Arruda-Boyce model assumes the following expression

$$U = N k_B \theta \sqrt{n} \left[\beta \lambda_{chain} - \sqrt{n}\, ln \left(\frac{\sinh \beta}{\beta}\right)\right] \tag{2-12}$$

where n is the number of chain segments, k_B is the Boltzmann constant, θ is the temperature in kelvins, N is the number of chains in the network of a cross-linked polymer.

$$\lambda_{chain} = \sqrt{\frac{I_1}{3}}, \quad \beta = \mathcal{L}^{-1}\left(\frac{\lambda_{chain}}{\sqrt{n}}\right) \tag{2.13}$$

where $\mathcal{L}^{-1}$ in the inverse Langevin function which can be approximated by

$$\mathcal{L}^{-1}(x) \begin{cases} 1.31 \tan(1.59x) + 0.91x & for\ |x| < 0.841 \\ \frac{1}{sgn(x) - x} & for\ 0.841 \leq x < 1 \end{cases} \tag{2.14}$$

For further details of the formulation and application of the mentioned hyperelastic models see Millard [59], Boyce [60], Ali [52], Beda [61], Bergström [58] and co-workers.

2.3.3 Mechanical behaviour of prostatic tissue

In the literature, there are studies which have attempted to characterize the material properties of the prostatic tissue and quantitatively classify the statistical variations between different tissue conditions with the aim of distinguish between normal and pathological conditions. However, it is worth pointing out that the mechanical parameters can vary, sometimes greatly, based on the mechanical test performed, boundary conditions, tissue size and the source of the tissue samples etc, and these factors will be reviewed and discussed below.

Carson et al. [62] performed mechanical characterisation for 26 prostate specimens obtained by prostatectomy and 6 specimens from autopsy. The system included a spherical indenter (whose tip is 12 mm in diameter) which can load up to 30% of the prostatic tissue thickness with an indentation velocity of 1mm/s. The force-displacement data were recorded and the Oliver–Pharr method was exploited for estimating the elastic moduli of the cancerous and healthy regions of the prostate. The force-displacement curves showed the nonlinear response of the prostatic tissue under large deformation. More importantly, this study suggested a significant difference between the Young's modulus of cancerous tissue compared with the healthy - the stiffness increased with the pathological stage of the cancer (T2 and T3). Details of the pathological stage of PCa will be provided later. Furthermore, a large variability in the Young's modulus between the samples can be found, which indicated a high degree of heterogeneity in both cancer and healthy tissues. Ahn et al. [63] developed an indentation device which was exploited for measuring the elastic moduli of the prostatic regions which showed the presence/absence

of cancer. The samples were obtained from 46 patients who underwent prostatectomy. A total of 552 sites were probed with an indentation depth of 3 mm and a velocity of 1mm/s. The elastic moduli were estimated by the force values and the Hertz-Sneddon equation. The results again showed the Young's modulus variation between cancerous and healthy regions. Furthermore, the modulus was higher for cancer with Gleason score 8 and with a volume greater than 5 mm^3.

Dynamic indentation tests were also performed with the aim of improve the mechanical characterization of the prostatic tissue. Krouskop et al. [64] evaluated the mechanical response of a prostate specimen when a compression loading was applied. The indenter size was 4.83mm, the pre-compression of 2 and 4% with excitation frequency of 0.1-4Hz. The results suggested a non-significant variation between the Young's modulus of the anterior and posterior parts of the prostate. However, once again, the cancerous regions have higher Young's modulus compared with the healthy. The BPH regions are softer comparing with the normal tissue. Phipps et al. [39] also proved the variation of the mechanical properties between healthy and cancerous prostatic tissues and a correlation with the tissue morphology. The tissues evaluated in the study were collected from 22 patients who underwent transrectal resection of the prostate (TRUS). Individual TRUS chipping were analysed performing dynamic measurements with excitation frequencies ranging between 5-10Hz. The mechanical test allowed the measurements of the dynamic modulus, which is defined by the amplitude ratio and the phase difference. The results showed a slight variation of the amplitude ratio for cancerous samples compared with healthy. Hoyt et al. [65] claimed the stiffness ratio between cancerous and healthy prostatic tissue to be 2.5. A stress relaxation test was performed in 8 prostates and the data were fitted using a viscoelastic tissue model method, Kelvin–Voigt fractional derivative (KVFD). The frequency range was between 0.1 and 250Hz and the results

showed an increasing Young's modulus between cancerous and healthy tissues with respect to increasing frequency values. Zhang et al. [66] performed a stress relaxation test in 17 cylindrical samples, which underwent a compression rate and strain value of 5mm/s and 5%, respectively. The relaxation data were fitted using KVFD method. The statistical analysis of the results showed a significant difference in the Young's moduli between cancerous and healthy prostatic tissues. Hammer [19] at al. developed a deployable palpation device which is able to distinguish between cancerous and healthy prostatic tissues performing a dynamic palpation with the aim of measuring the quasi-static and dynamic modulus values. The mechanical measurements were performed using multiple indentation depths and a frequency of 1 and 5Hz. The probe has a size of 6 mm and the distance between the indentation points was set up at 6 mm for avoid overlapping in the measurements. The number of whole *ex-vivo* prostates and indentation points assessed in the experiment were 11 and 359, respectively.

In conclusion, the mechanical properties of the prostatic tissue could vary with the presence of cancer. Furthermore, the stage and aggressiveness of the disease also influence the mechanical response. In Table 2-1 summarises those studies mentioned above and the elasticity values measured for healthy, BPH and PCa tissues. The quantification of the material properties promotes the development of diagnostic tools, which are based on the tissue elasticity, for distinguishing cancerous and healthy prostate tissues.

Table 2-1. Summary of the studies which measured the prostatic tissue stiffness characterized by diverse physiopathological conditions [6].

Authors	Year	Ex/in vivo	Study design	Patient/Specimen number	Mechanical properties
Carson et al. [62]	2010	Ex vivo	Spherical indentation device (12 mm diameter tip), indentation of 30% depth and 0.1mm/s velocity	23 prostatectomy specimens, 6 autopsies	**Young's modulus (kPa)** **Normal 41.1** **BPH 36.8** **PCa 135** **PCa(T2) 30.09** **PCa(T3) 71.0**
Ahn et al. [63]	2010	Ex vivo	Indentation device, 3mm and 1mm/s indentation depth and velocity	46 prostatectomy specimens	**Young's modulus (kPa)** **Normal 17±9** **PCa 24±14.5**
Krouskopet al. [64]	1998	Ex vivo	Indenter method, pre-compression 2-4%, excitation 0.1-4Hz	1 prostate specimen	**Young's modulus (kPa)** **Normal 55-71** **BPH 36-41** **PCa 96-241**
Phipps et al. [39]	2005	In vitro	TURP chipping specimens	83 samples from 22 patients	**Dynamic modulus (kPa)** **BPH 100** **PCa 118**
Hoyt et al. [65]	2008	In vitro	Mechanical testing device, excitation frequency 0.1-250Hz, 5% pre-compression	8 prostate specimens, 17 cylinders samples	**Young's modulus (kPa)** **Normal 3.8-25** **PCa 7.8-40.6** **(frequency dependent)**
Zhang et al. [66]	2008	In vitro	5% pre-compression, 150Hz excitation frequency	8 proctectomy prostate (posterior region), 17 cylinders samples	**Young's modulus (kPa)** **Normal** **15.9±5.9** **PCa 40±15.7**
Hammer et al. [19]	2017	Ex vivo	Sinusoidal indentation, frequency of oscillation 1 and 5Hz, indentation depth 3, 5 and 8mm	11 prostate specimens	**Dynamic modulus (kPa)** **Normal** **14.2±0.2** **PCa 14.4±0.2**

2.4 PCa – current diagnostic techniques

The current screening protocols for PCa include techniques such as medical imaging, blood test and biopsy. However, the protocol is not optimized and consistent between healthcare sectors, and is severely limited by the funding, equipment and practitioners available. Typically, the screening procedures for PCa diagnosis include Prostate Specific Antigen (PSA) blood test, Digital Rectal Examination (DRE), Magnetic Resonance Imaging (MRI) and biopsy. This section will review the current diagnostic framework for PCa, with a focus on mechanics-related techniques that are relevant to this thesis work.

2.4.1 Prostate – Anatomical Structure

The classical description of a healthy human prostate portrays it as slightly larger than a walnut. The mean weight of the normal prostate in adult males is about 11 grams, usually ranging between 7 and 16 grams [67]. The prostate resides in the male pelvic cavity which contains the end part of the large intestine, the urinary bladder, the seminal vesicles and the pelvic bone plus some other minor structures (Fig. 2-3).

Traditionally, the prostate is divided into anatomical lobes (anterior, posterior, right and left laterals and median) by the urethra, which runs through the centre of the prostate. However, more important clinically is the histological division of the prostate into three zones:

Central zone (CZ) – surrounds the ejaculatory ducts, comprising approximately 25% of normal prostate volume.

Transitional zone (TZ) – located centrally and surrounds the urethra, comprising approximately 5-10% of normal prostate volume. The glands of the transitional zone are those that typically undergo benign hyperplasia (BPH).

Peripheral zone (PZ) – makes up the main body of the gland (approximately 65%) and is located posteriorly. The compartment shows a high incidence of acute and chronic inflammation which may link to the high incidence of prostate carcinoma at the peripheral zone. The peripheral zone is mainly the area felt against the rectum on digital rectal examination.

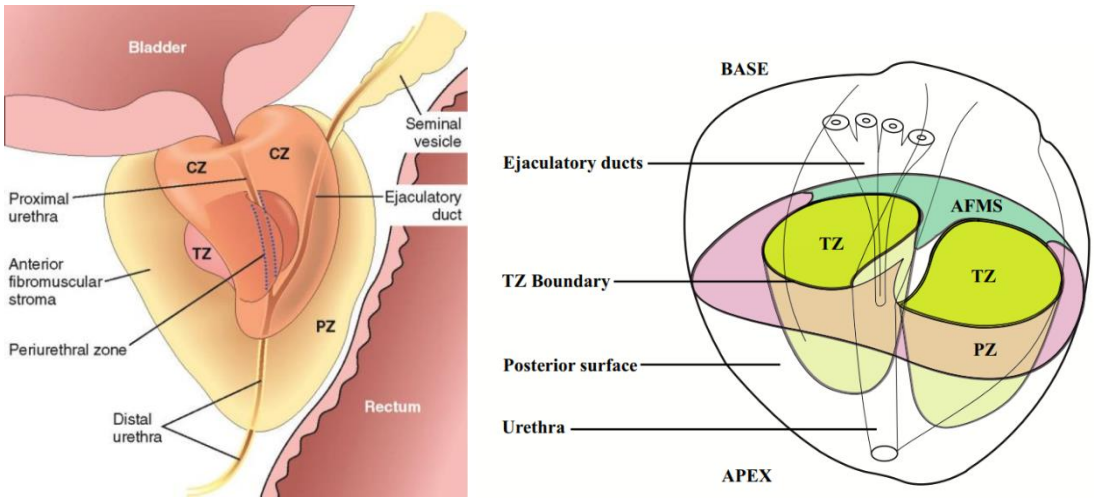

Fig. 2-3. The image illustrates organs which surrounding the prostate and the histological division which are important clinically (3D posterolateral view) [68].

2.4.2 Blood Test

A significant improvement in the detection and decreasing in the deaths due to prostate cancer has been made in the last years. The major reason has to be found in the introduction, in the screening protocol, of the PSA blood test. The prostate specific antigen (PSA) is a not invasive test and inexpensive which is applied to large scale of patients [69]. Therefore, the clinician often is guided by the PSA results at the first instance to decide if further investigations are needed. The test expects measuring the amount of PSA in the blood. PSA is a protein produced by normal cells in the prostate

and also by prostate cancer cells. It is normal to have a small amount of PSA in the blood; however, a raised PSA level may suggest a problem with the prostate, but not necessarily cancer. Therefore, The PSA presents a low specificity which will lead to misdiagnosis due to the detection of false positive [8]. The major causes for false positive detection using PSA test are the presence in the prostatic tissue of calcifications, inflammations and BPH. These symptoms can increase the value in the blood of the PSA protein which is released generally in more quantities when there is the presence of cancer [7]. The chances of showing these symptoms also increase significantly with the age of the patients [70]. The PSA is a protein which can have two basic states, it might be bound to another protein or float freely. Besides, the quantification of the free percentage of PSA might increase the specificity for prostate cancer detection [71].

2.4.3 Digital Rectal Examination (DRE)

In clinical practice, the elasticity as a biomarker can be defined as an old method as the DRE performed by the practitioners to detect PCa since decades ago. The DRE consists of palpating the tissue with the aim of identifying abnormalities and stiff nodules in the prostatic tissue which could be the signs of PCa [9]. As mentioned above, the cancerous tissue becomes stiffer than the surrounding healthy due to a variation in the morphology. The DRE shows many advantages such as the less-invasive nature of the procedure, painlessness, ease to perform and less cost compared to other early diagnosis methods. However, it has limitations such as the lack of quantitative assessment of the tissue quality and the subjectivity in the diagnosis [12]. Therefore, novel mechanical palpation devices have been developed with the aim of overcoming the limitations of the DRE. Details of the devices and their performance in overcoming the DRE limitations for PCa detection using elasticity as biomarker will be discussed later.

2.4.4 Medical Imaging - Magnetic Resonance

MRI is a medical imaging technique used in radiology to form pictures of the anatomy and the physiological processes of the body in both health and disease. It is frequently used for PCa diagnosis, capable of initial detection, treatment planning and follow-up. MRI scanners use strong magnetic fields, magnetic field gradients, and radio waves to generate images of the organs in the body. MRI does not involve X-rays or the use of ionizing radiation, which distinguishes it from computerised tomography (CT) and positron emission tomography (PET) scans. Moreover, MRI has a limitation in detection tumor nodules of < 10mm and in classifying cancerous regions from benign conditions such as BPH. Therefore, the diagnostic technique is limited in assessing the cancer volume fraction.

Recently, interested results and improvements in the early detection and characterization of prostate cancer, especially of high-grade tumors, has been made with the developing of multiparametric MRI (mpMRI) [72], [73]. mpMRI combining the morphological assessment, which is obtained by performing a MRI, with diffusion-weighted imaging (DWI) [74] and dynamic contrast-enhanced (DCE) perfusion imaging [75]. This novel diagnostic method could help in identifying where the cancer is in the prostate and reducing the number of men without cancer having a biopsy. The technique showed promising for biopsy decision for men referred with high PSA level (Fig. 2-4). However, the technique remains challenging both in the acquisition of images and in their interpretation.

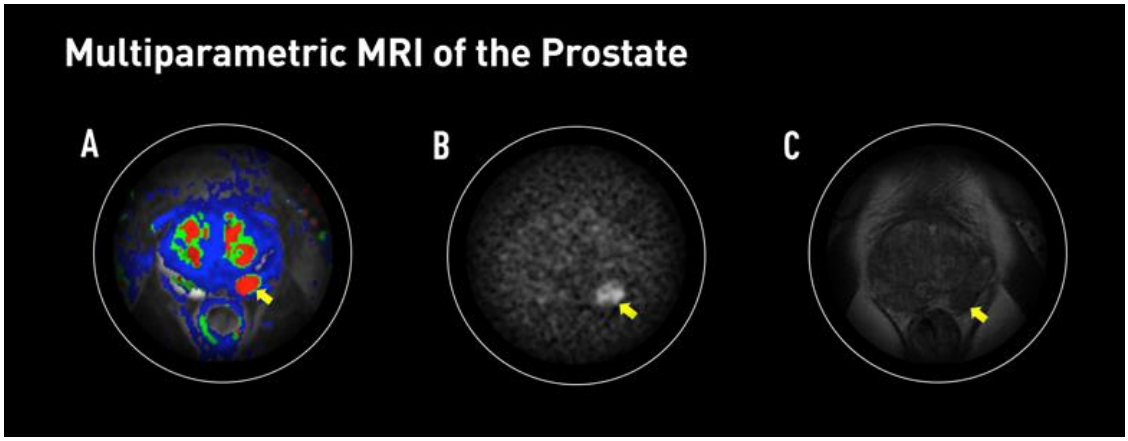

Fig. 2-4. mpMRI for prostate cancer detection. 5a) dynamic contrast enhancement colour map which allows the identification of the tumor nodule as it shows higher perfusion of the contrast compared with the surrounding. 5b) The T2-weighted image [76] which allows the classification of the tumor nodule from the normal tissue based on the diverse tissue structure morphology. 5c) The Diffusion-weighted image which shows the rate of water diffusion in the tissue[2].

A diagnostic technique generally used by the clinicians for PCa detection is the Magnetic Resonance Elastography (MRE). The MRE is a non-invasive technique which can map and calculate the shear modulus of the prostatic tissue based on inducing shear waves through the prostate and imaging their propagation using MRI. The shear waves are produced by a manual exciter which can 'palpate' the prostatic tissue [77]. The main idea is that whether the tissue is hard or soft will give diagnostic information about the presence or status of disease. As mentioned, tumor nodules will often be harder than the surrounding tissue. The major limitations are the high Signal-to-noise ratio (SNR) due to the MR signal a 1.5 T (the scanner of the MR system generates a magnetic field which is quantified in Tesla (T) [76]) and the shear wave might not have enough amplitude to propagate deeper through the prostatic tissue when their values are within the non-dangerous range [78]–[80].

[2] http://sites.bsyse.wsu.edu/pitts/be120/Handouts/animal%20tssue%20descriptions%20and%20mechanical%20proprties.htm

2.4.5 Medical Imaging - Ultrasound

The PCa detection using ultrasound (US) is performed via the transrectal route (TRUS) [81]. A small device called an ultrasound probe is used for generating high-frequency sound waves. When sound waves bounce off the prostatic tissue, they create "echoes" which are picked up by the probe and turned into an image. The stiffer areas in prostate due to the presence of cancer cause a decreasing in the property of reflective index which leads to the hypoechoic areas visible in a US scan [15], as illustrated in Fig. 2-5. The method is not invasive, provides to the clinicians a quantitative diagnosis measuring the stiffness of the soft tissue, does not expose the patients to ionizing radiation, is less expensive than other techniques such as MRI, mpMRI and MRE. However, the US has been found to have low sensitivity and specificity as the cancerous lesions can appear isoechoic and hyperechoic [17], [82].

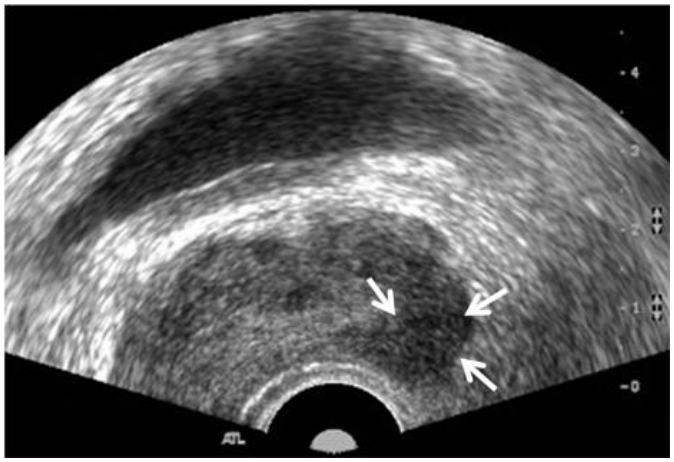

Fig. 2-5. Prostatic tissue characterized by the presence of a tumor nodule which is detectable using Ultrasound image as it shows a hypoechoic area[3].

[3] https://www.sonoslinks.com/service/prostaterectal-ultrasound

Based on US technique, the Sonoelastography can map the stiffness of the prostate based on a US image captured before and after the application of a compression [83], [84]. The major limitation of the Sonoelastography is the high rate of false positive due to the presence of BPH in the prostatic tissue [85]. The manual compression and uncompressing of the soft tissue can produce variability and poor reproducible analysis [86]. In addition, the colour map obtained performing the Sonoelastography lack of an objective assessment [66]. The cancerous and healthy tissues show a high grade of heterogeneity intra- and inter-patient which cause an ambiguity in stiffness values observed. The clinician might deal with tissues which are healthy and cancerous, however, they may show same stiffness values. Another technique based on Elastrography is the Crawling Wave Sonoelastography. In this case, the waves are obtained by mechanical vibrations from two different sources at two distinct frequencies [87], [88]. This technique allows the real-time visualization of the prostate stiffness map, as shown in Fig. 2-6). However, the technique is less capable of detecting small tumor nodules and are prone to issues such as the influence of the stiffness ratio between the cancerous and healthy regions, the false positive due to the BPH, calcifications and image artefacts [89], [90].

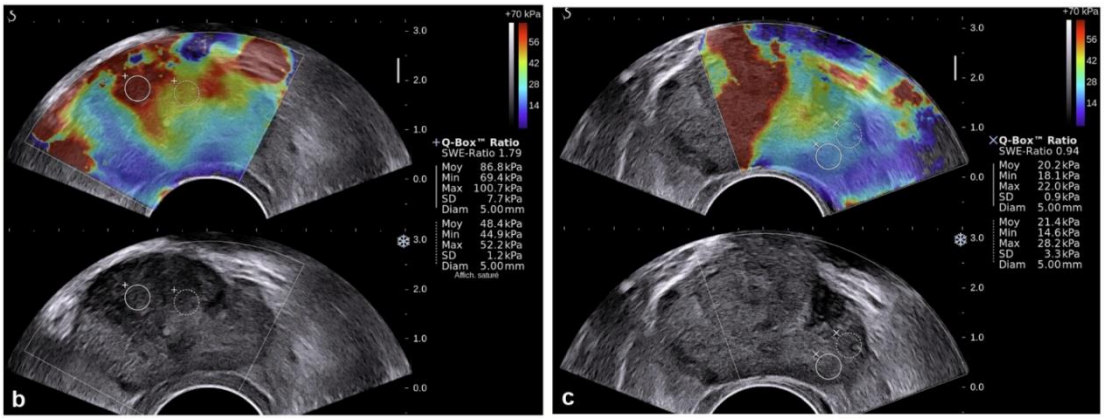

Fig. 2-6. Prostate with a tumor nodule located in the anterior right base. The Sonoelastography shows higher stiffness values in the region where there is the presence of the tumor (a), instead, a 'normal' stiffness distribution on the left side of the prostate (b) [16].

In conclusion, the medical imaging diagnostic techniques present important limitations in the PCa identification, in particular, in detecting small tumor nodules, and can also be significantly influenced by the stiffness ratio between healthy and cancerous tissues which are unknown at the point of diagnosis. They are also prone to such issues as the high probability of false positive due to calcification, inflammation and presence of BPH nodules into prostate. The artefacts in the stiffness map images due to the noise in the input signals and the uncontrolled manual mechanical generation of the waves. More importantly, the lack of objectivity in the assessment of the imaging for a quantitative diagnosis. These reasons and the expensive nature of the machines leads to a variability and poor reproducible analysis of detecting PCa using diagnostic techniques based on medical imaging.

2.4.6 Biopsy

Biopsy is a procedure which allows the examination of the sample tissue morphologies. The procedure has been improved as the tissues were taken using a needle which was guided just by the surgeon's experience in recognize the anatomy of the patients [91].

Nowadays, the procedure is performed using Ultrasound (TRUS) and sextant approach to guide the clinicians in the identification of the suspicious areas useful for the tissue quality assessment. The samples are examined using histological techniques. The procedure is repeated 10-12 times (up to 20) in diverse locations of the prostate [92]. However, the successful detection rate for the biopsy procedure is only 20% even with an increase of the samples which can lead to an improvement in the accuracy procedure [93]. The motivations can be found in the PSA low specificity and in the lack of a diagnostic tools which can distinguish between 'not significant' and 'significant' tumor nodules. Furthermore, there are false positive in the biopsy outcomes as the knowledge a priori of the locations for the suspicious areas is still challenging even with the Ultrasound image [94] (Fig. 2-7). Moreover, the biopsy is an invasive technique which can cause pain and discomfort for the patient and the chance of side-effects as rectal bleeding, haematuria and acute urinary retention [95].

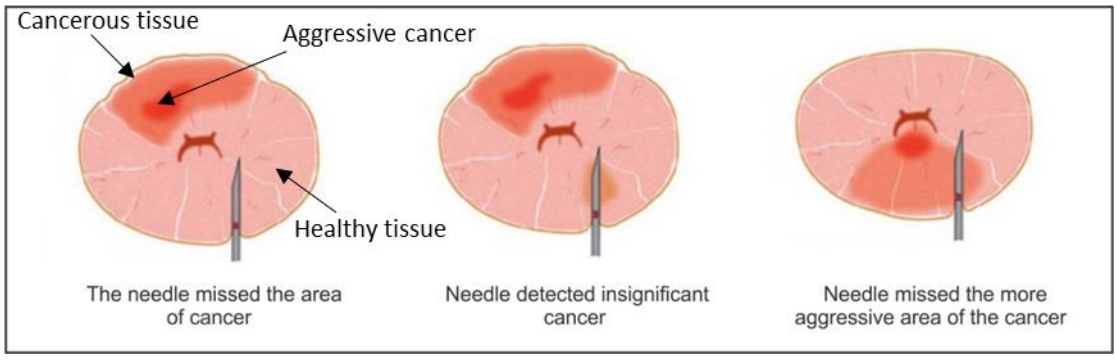

Fig. 2-7. Illustration of the biopsy procedure possible issues which can cause a false positive and provide a mistaken grade for the cancer aggressiveness[4].

[4] https://partnersprostate.com/prostate-biops

2.4.7 How to stage Prostate Cancer

The diagnostic techniques for detecting PCa described previously can be exploited by the clinicians for assessing the cancer stage.

There are 2 types of staging for prostate cancer[5] :

- Clinical staging. This is based on the results of DRE, PSA testing, medical imaging and Gleason score
- Pathologic staging. This is based on the histopathological examination of the prostatic tissues obtained after removing the entire prostate and some lymph nodes using laparoscopy surgery.

In clinics the TNM system is used for describing the cancer stage. The clinicians could provide the details of where the cancer is located, if it has spread and if it affects other parts of the body. Using the TNM system, the ‘’T’’ plus a letter or number (0 to 4) is used to describe the size and location of the tumor. The ‘’N’’ stands for lymph nodes and the ‘’M’’ indicates whether the prostate cancer has spread to other parts of the body.

Specific tumor stage information is listed below

- T0: there is no evidence of a tumor in the prostate.
- T1: the tumor cannot be felt during a DRE and is not seen during imaging tests.
- T2: the tumor is found only in the prostate, not other parts of the body. It is large enough to be felt during a DRE
- T3: the tumor has grown through the prostate
- T4: the tumor is growing through the prostate and into nearby structures other such as, the rectum, the bladder or the pelvic wall.

[5] https://www.cancer.net/cancer-types/prostate-cancer/stages-and-grades

2.5 Mechanical palpation device – elasticity as biomarker

The elasticity as biomarker, for classifying cancerous tissue from healthy ones, has been proved to be a candidate for overcoming the shortcomings in the existing PCa diagnostic framework [96].

In literature, there have been devices developed with the aim of detecting solid tumour in soft tissue based on instrumented palpation. Hammer and co-workers [19] developed a device, as shown in Fig. 2-8, capable of detecting the appearance of PCa, complementary to the existing DRE procedure. The device has been validated using ex-vivo measurements. The device is also deployable so that in-vivo assessments can be performed. In addition, Robotic devices were developed by Ahn [97] and Li [98] However, the dimensions and palpation procedure reduce drastically the in-vivo performance of these devices (Figs. 2-9 and 2-10). The devices aimed to maintain the advantages of the DRE and overcome its limitations. Therefore, they need to reduce the time and cost of the procedure, discomfort for the patient, avoiding any damage to the prostate and organs which surrounding it due to deep palpation and find a robust contact detection for improving the sensitivity of the procedure. The mechanical palpation for diagnosis purpose can be performed for identifying presence of cancer in other biological tissues. The localization of tumor nodule(s) in liver and lung can be performed using tactile sensors during minimally invasive surgery (MIS) [99]. In minimally invasive approaches, small incisions are made on the body and tissue damage is much less than that of the invasive method (Fig. 2-11). In the cited papers, the diagnosis is obtained with the assessment of elastic and viscoelastic parameters which are subjected to variation when the three is presence of cancerous tissues in the organ under investigation.

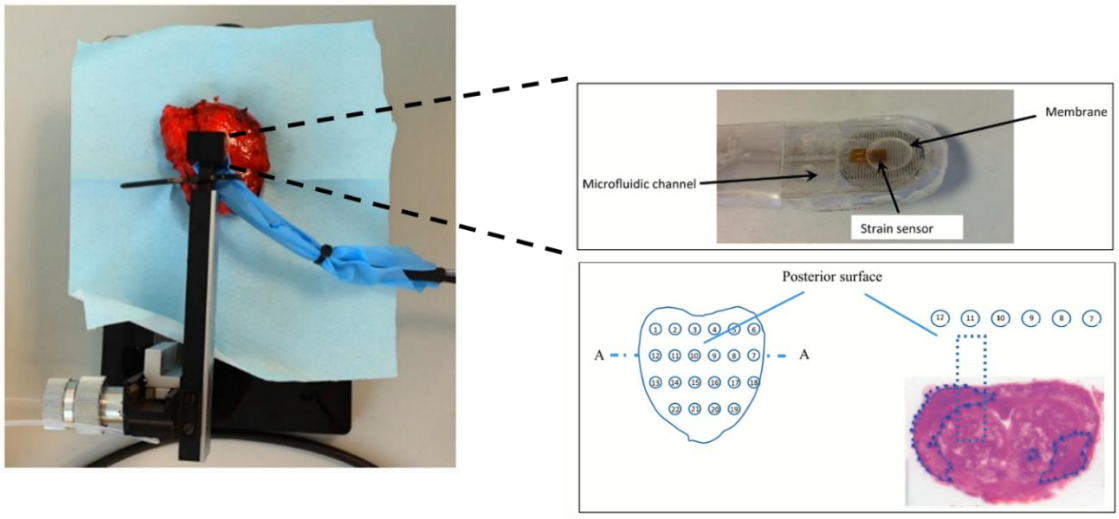

Fig. 2-8. Deployable palpation device which is able to distinguish between cancerous and healthy prostatic tissues based on dynamic palpation [19].

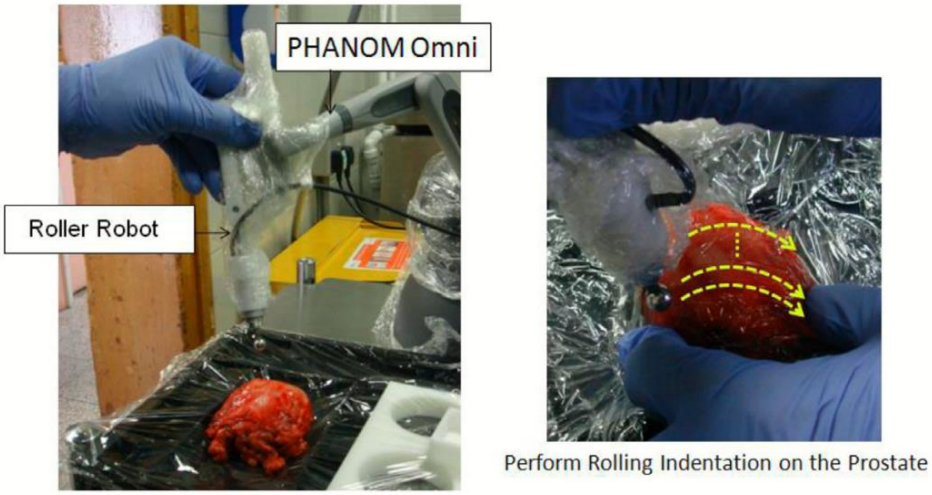

Fig. 2-9. Mechanical palpation device which provides a classification between cancerous and healthy prostatic tissue based on force feedback values obtained performing a rolling indentation [98].

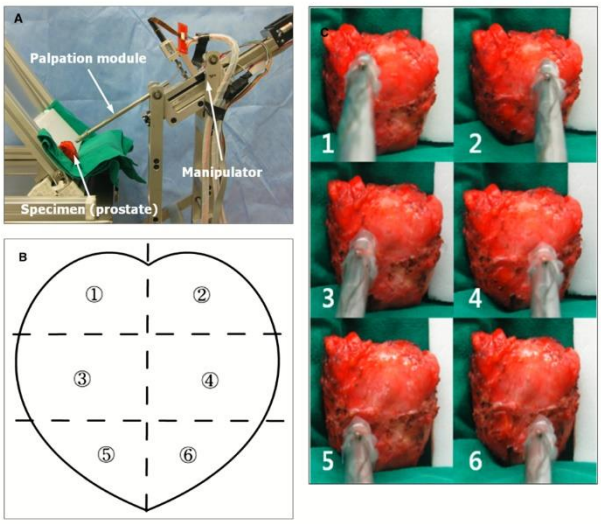

Fig. 2-10. Robot system for prostate cancer detection. The robot performs a sweeping palpation in the prostatic tissue and based on the characterization of the tissue mechanical response is able to identify the presence of a tumor nodule. The system has a biopsy module which allows the taking of a tissue sample along the direction of the detected tumor nodule [97].

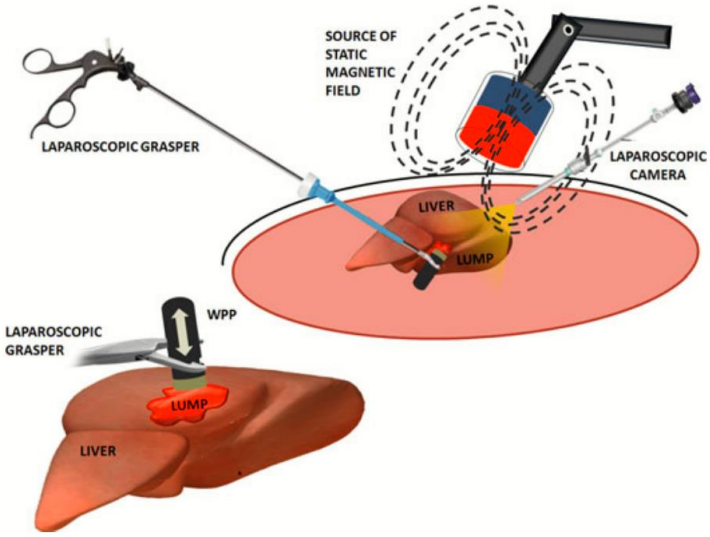

Fig. 2-11. Tissue palpation procedure during MIS exploiting a wireless probe for identifying abnormalities in the soft tissue [99].

2.6 Computational and numerical methods for tumour detection

The palpation devices can provide a quantitative assessment of the tissue quality [100].

However, the accuracy of the palpation procedure can be strongly influenced by the

heterogeneity of the cancer and inter-patient variations [20], [101]. Furthermore, the characteristics of the indenting/probing procedures can cause variation in the sensitivity [102]. Therefore, computational diagnostic frameworks were necessary in order to make sense of the data acquired from the instrumented palpation [103], [104].

2.6.1 Inverse analysis - mechanical characterization of biological soft tissue

The palpation device allows the measurement of mechanical behaviour of soft tissue, such as elastic response, by probing the tissue sample. In the case of indentation, the measurements can be characterised by fitting the force-displacement data with a suitable model, such as the Hertz-Sneddon [105]. However, most existing analytical models are based on many hypotheses and assumptions including a flat surface of the sample, a frictionless contact between the indenter and sample, infinite sample thickness and elasticity properties of tissue [21], which may not readily available at the point of analysis Therefore, various inverse methods have been developed in order to overcome such limitations. In most cases, finite element method is employed and integrated in the inverse methods. Such inverse FE approaches are often capable of modelling more realistic interaction between indenter and sample, more accurate non-linear mechanical response of the soft tissue even for complex geometry and boundary conditions. The strategy of such inverse methods is usually to employ an optimisation algorithm and drive a set of unknown parameters iteratively so that the modelled scenarios match closely to the experimental measurements. The following section will review studies in literature that proposed and employed inverse methods for the purpose of tissue characterisation and nodule identification.

Mechanical indentation *ex-vivo* and inverse analysis were performed to characterize the mechanical properties of animal biological tissue as liver, lung and cornea [53], [106],

[107]. Martinez and co-workers [108] developed an inverse optimization procedure to assess the mechanical properties of human liver ex-vivo. The procedure aimed to iteratively minimize an error function formulated by the comparison of two 3D images. One was obtained from CT of the liver and it represented the reference, whilst the other one was from the results of the FE simulation. The material parameters are obtained when their variation led to a 'matching' between two models. Moreover, material properties of soft tissues change in time and the results obtained from ex-vivo measurements can be misleading. Dead organ and muscle tissues typically become stiffer [109]. Therefore, attempts at measuring the material properties in-vivo were preferred. Samur [110] and Kim [111] developed a robot indenter and force transducer to measure and record the mechanical output which were coupled with inverse FE model to characterize the mechanical properties of porcine liver and kidney. The inverse FE model expects iteratively compared the relaxation response of the soft tissue to an equivalent FE model, until the error function was minimized and the material properties were estimated. Kauer [112] and Nava [113] used the same mathematical and numerical tools but conducted experiments using a hand-held device to collect the experimental data to study the mechanical behaviours of human uteri and liver.

The mechanical response of the tissue can also vary when certain pathological conditions appear. Specifically, an inverse method can be formulated to determine the unknown material properties of the tumor nodule from the measured response. Mousavi and co-workers [114] developed a framework that relies on prostate TRUS or MRI image is capable of identifying the presence of hardness, a sign of pathological condition, in phantom systems which mimic the mechanical behaviours of a prostate. Samani [115], [116] developed a diagnostic framework to assess the breast tissue quality. The experimental measurements were performed by indenting the tissue samples. In both

studies, the mechanical properties are estimated using an inverse procedure based on the segmentation of the inclusion. The inverse procedure iteratively minimized an error function which is defined by the elastic response of the breast sample obtained by indenting the soft tissue and simulating the procedure using an equivalent FE model. The stiffness of the cancerous and healthy regions was obtained when the difference in the experimental and simulated force values was less than a threshold. Moreover, the accuracy of the method depends on the quality of the medical imaging and image segmentation methods, especially outlining the tumour boundary. Kim [21] and Ahn [117] used a mechanical palpation device to investigate the presence of cancer nodule in prostate and in a phantom with similar mechanical properties. The experimental *ex-vivo* measurements are coupled with inverse FE models which guarantee the quantitative identification of the cancer nodule in the tissue. The inverse FE model was optimised toward the target, in this case, the stiffness of the tumor nodule, following the same strategy mentioned earlier, using the comparison between experimental and simulated force response when an indentation procedure was performed. However, in the last two studies, to evaluate the relative change of the stiffness, the diagnostic framework requires geometry and volume of the normal and tumor nodule and their elastic properties, which would limit their applicability in clinical applications. An inverse FE method which utilised data from rolling indentation probe to evaluate the mechanical properties of healthy and diseased tissue has been developed [118], [119]. This method allowed estimating *ex-vivo* the cancer nodule's depth, however, it is necessary to know *a priori* the force feedback of the healthy tissue, which is almost impossible to obtain since pathological condition of the tissue is unknown.

In conclusion, the inverse FE methods, coupled with mechanical measurements, have the potential to predict the presence/absence of tumor nodule in soft tissue and its mechanical

parameters. However, most methods require certain information that is hard to obtain for clinical applications, therefore their potential use can be limited.

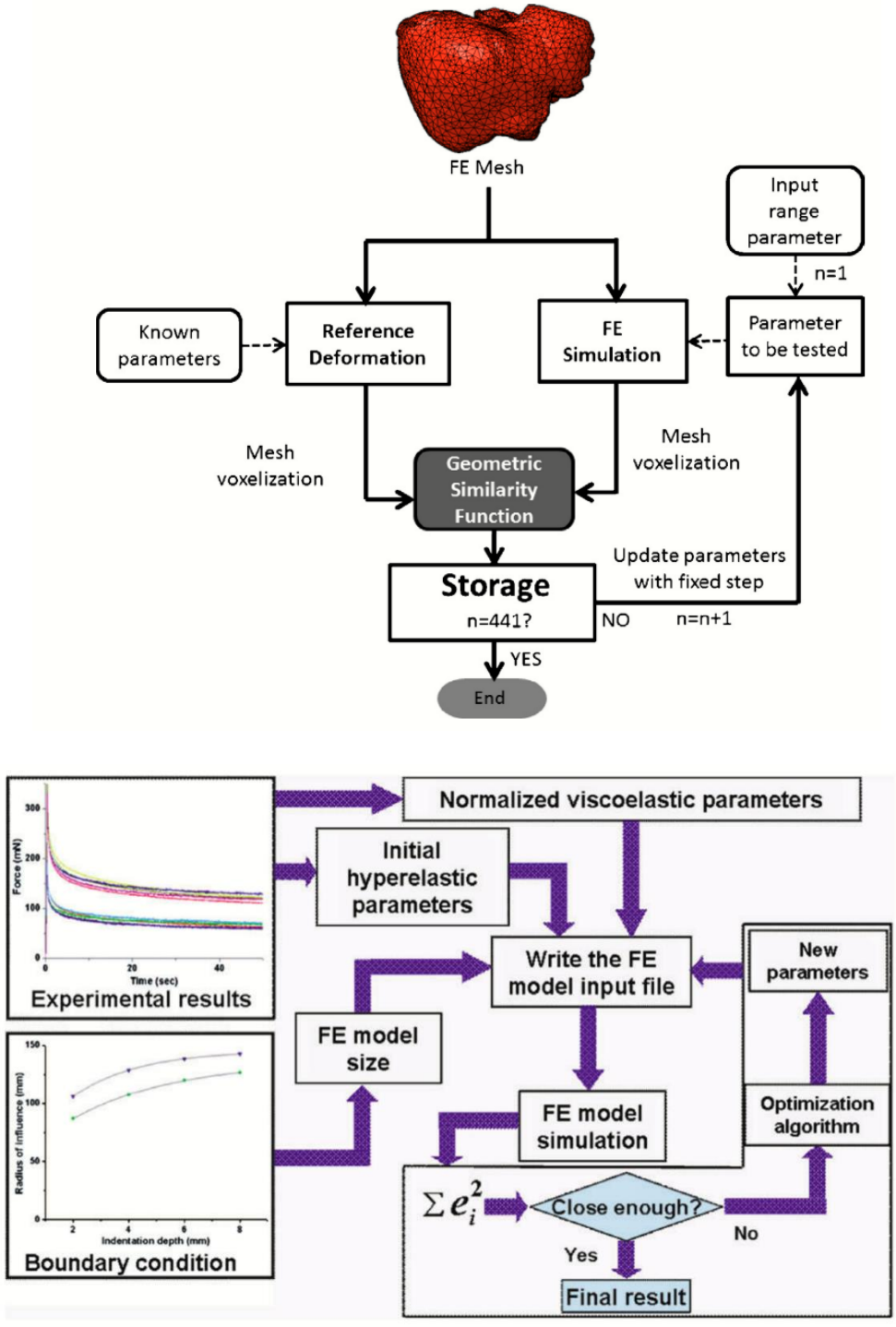

Fig. 2-12. Flowchart of the inverse analysis procedure for estimating the elastic parameters of human liver (top figure) [108] and surface deformation and force response of porcine livers (bottom figure) [120].

2.6.2 Force feedback - identification of tumor nodule

Ahn [96] and Jalkane [121] validated the strategy of distinguishing cancerous tissue from its healthy background based on the variation of reaction force values after performing a static or dynamic indentation. In particular, the presence of cancer leads to an increase in the reaction force. In addition, the force feedback has been validated as an index to identify the presence of stiffer inclusions embedded into ex-vivo animal tissues as porcine, bovine and lamb kidney [122]–[124]. However, the force feedback measurements are heavily influenced by the tumor nodule depth, size and the stiffness ratio between healthy and cancerous tissue [125]. For example, Ahn [117] measured the force feedback values performing a sweeping palpation using a phantom with a stiffer inclusion. The outcome confirms the significant influence of the nodule depth in the reaction force values.

Some interesting studies utilised the 'mechanical imaging' of soft tissue obtained from tactile sensing array, instead of using a rigid probe. These devices are able to produce a fine measurement of the pressure distribution of the soft tissue palpated [126], [127]. The pressure distribution usually is converted in a colour map for better visualization of the suspicious areas for the clinician. Beccani and co-workers [128] developed a palpation device to localize tumor nodules based on pressure distribution measurements. They validated the device using phantom systems with embedded stiffer inclusions and showed how higher pressure was measured at the position of the inclusions and how the pressure values decrease when inclusions located deeply into the phantom. Li and co-workers [129] have also developed a highly compliant tactile sensing array, and similarly, they applied the sensor to measure the pressure distribution in a phantom with a stiffer inclusion. The results showed how the accuracy of the predicted suspicious area depends on the nodule size and depth as well as the indentation depth applied. The accuracy

reduces if the nodule depth increases and/or if the nodule size and indentation depth decrease, as shown in Fig. 2-13.

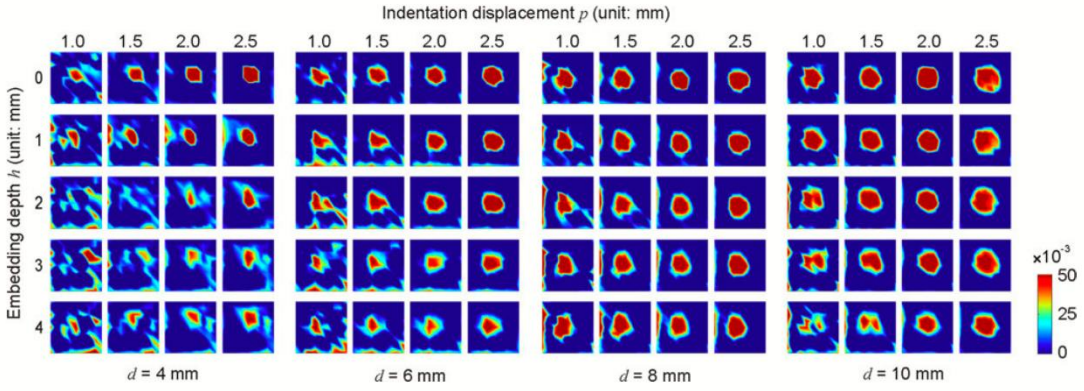

Fig. 2-13. Pressure distribution measured using a tactile sensor array and phantom with embedded stiffer nodule. The results show an improvement of tissue nodule identification for higher indentation displacements and when the nodule has a larger size. However, the detectability decreases significantly when the nodule is located deeply in the phantom. The values of the pressure were normalized by the authors (colour bar unit: %) [129].

In conclusion, the evaluation of force feedback values allows an identification of the presence of tumor nodule(s). However, the sensitivity of the procedure depends strongly by the nodule features as its depth, size and modulus [130]. Similarly, the diverse palpation procedures, size of the probe and indention depth also influence the sensitivity and effectiveness of the proposed identification methods.

2.6.3 Identification of tumor nodules

It is important, clinically, to detect the presence of cancerous nodules, often in a binary fashion, which is not a trivial task. Further to that, it is also interesting, inevitably more challenging, to detect the dispersion and distribution of the cancerous nodules. At this front, little success has been achieved by using instrumented palpation. Sangpradit et al.

attempted to predict the position and depth of the inclusion exploiting a rolling indentation and FE simulations [118]. The indentation was performed in phantom and kidney tissues where stiffer inclusions were embedded. The position of the nodule was predicted based on the peak identified in the reaction force profile. However, the peak force depends by the nodule depth and a downtrend is obtained when max reaction forces vs. nodule depths are plotted. The analytical fitting of the trend guarantees to predict the nodule depth based on the reaction force measurements. Kim [21] developed an analytical solution for the nodule depth, size and property ratio using similar methodologies to Sangpradit et al. research. However, the cited papers present a limitation in the prediction. Decoupling the effect of nodule size and depth using elasticity and force feedback values is still challenging as, for instance, a big and deep nodule can generate same force values than smaller nodule located close to the indented surface. Kim [131] developed a sweeping palpation device with the aim of measuring the force response of the soft tissue, as example prostate. The identification of suspicious regions is determined based on a comparison between the modulus estimated and stiffness values measured for a healthy prostatic tissue. However, the prostatic tissue even when it is healthy has a high degree of heterogeneity. For this reason, the method can be subjected to misdiagnosis.

The prediction of the nodule depth and size has been attempted to achieved using artificial neural network (ANN). Yen and co-workers [132] suggest a neural network which is trained using FE simulations. In particular, the prediction is made based on the peak features as amplitude, width and base which are obtained performing the indentation using a max depth value of 14 mm. Jon-Ha Lee [133] developed a tactile imaging system and an artificial neural network to predict nodule depth, size and modulus embedded in breast tissue. However, in both cited studies a *prior* knowledge of the presence of the inclusion is needed. Kirk [134] developed an artificial neural network using elastography

measurements to segment the boundaries of a stiffer inclusion embedded in a phantom system. Moreover, there is no evidence of the accuracy of the diagnostic framework for the nodule heterogeneity as its depth.

The ANN techniques strongly depend on the precision of the training data-set. otherwise a poor prediction or an overfitting in the solution could be reached. Therefore, this is a clear limiting factor when dealing with patient data.

In conclusion, the identification and characterization of cancer in soft tissue can be obtained performing mechanical palpation and analysing the force feedback response. However, the heterogeneity of the normal and cancer tissues leads to a significant variability in the mechanical response. Therefore, the development of a predicted model, for overcoming the limitations of the diagnostic frameworks mentioned in the literature, will be suggested.

2.7 Bridging the gaps

The objectives and literature review conducted so far recommend a number of challenges, which will be further investigated in the following chapters

- The mechanical palpation devices showed promising potential for early cancer detection as they are non or less invasive, inexpensive and provide quantitative outcome. However, the mechanical measurement can be heavily influenced by the presence/absence of the tumor nodule(s) and the anatomical variation of the patients as the organs which surrounding the prostate, its position, size, geometry and stiffness. Therefore, it is necessary to develop a numerical framework, based on instrumented palpation, for detecting the presence/absence of the tumor nodule with the least amount of anatomical knowledge of the patient, as it may not be readily available at the point of measurement.

- The detection of the presence/absence of the tumor nodule using force feedback values is strongly influenced by the cancer heterogeneity. The nodule size, depth and stiffness could cause variations in predictions. Therefore, a sensitivity analysis of the computational diagnostic framework as a function of the nodule parameters is needed.
- The diagnosis in clinical practice for patients who suffer by cancer is sorted with the assessment of cancer stage and aggressiveness. Therefore, the prediction of the tumor nodule, size, depth, dispersion and mechanical properties are crucial for improving the prognosis of the patients. A predicted model able to identify the presence/absence of the tumor nodule(s) and provides as outcome the position, depth, suspicious area of the tumor(s) with a degree of confidence is essential and will be developed in this thesis.
- The mechanical characterization of biological tissue for diagnosis purpose using palpation devices is still challenging. The presence of benign conditions as inflammation and calcification can cause diverse force feedback values. Likewise, the presence of cancer could significantly increase the tissue elasticity and the variation may arise from more aggressiveness cancer types. Furthermore, the biological tissue shows a high variability between diverse patients. The mechanical response and the interaction between the samples and the probe, when a probing procedure is applied, lead to a whole new level of complexity. Therefore, there is a need of assessing the identification methods using experimental data with the aim of quantify the uncertainties, given rise by the complications mentioned earlier, in the diagnosis using palpation procedure.

In conclusion, there is a need of developing new complementary diagnostic tool with the aim of improving the early cancer detection and ultimately the prognosis for the patients who suffer by PCa. More importantly, a diagnostic method able to distinguish 'significant' and 'not significant' cancer, avoiding unnecessary biopsies and medical cost, would be useful. Therefore, it is crucial to develop novel mechanical palpation devices for cancer early detection [135], and more importantly, the data analysis tool associated with them.

The thesis will address the major challenges mentioned above and aims to attempt to equip the instrumented palpation devices and their mechanical measurements with novel numerical methods and nodule identification algorithms. Vitally, it aims to improve the sensitivity and specificity of the palpation diagnostic framework, quantifying its limitations and establishing prediction for the tumor nodules such as their size, position, depth, dispersion, which ultimately would lead to improved clinical assessment of the condition and aggressiveness of PCa.

Chapter 3

Identification of Tumor Nodules in Soft Tissue – An Inverse Finite-Element Framework based on mechanical Characterization

Contents

3.1 Summary

This chapter aims to establish an FE-based inverse method to characterize the size of a soft tissue sample and detect the presence of a cancerous nodule in it, without *a priori* knowledge of the nodule geometry and location. Prostate tissue is used, without loss of generality, as an exemplar system. The method is based on knowing the reaction forces obtained from mechanically probing a prostate sample and those derived from an

equivalent FE model, which is optimized iteratively towards the target solution by minimizing an error function between the two sets of reaction forces. By doing so, it is possible to estimate not only the volume of the prostate, but, more importantly, the embedded tumor nodule can also be identified from its influence on the stress field resulting from mechanical probing. The effectiveness of the proposed method is verified using a realistic prostate model reconstructed from a magnetic resonance (MR) image.

3.2 2D Computational model

The prostate is surrounded by a number of other structures *in-vivo*, including the bladder, and the rectum as well as being embedded in connective tissue, as illustrated by an MR image in Fig. 3-1(a). Digital Rectal Examination (DRE) involves accessing the palpable surface trans-rectally, which will deform these other structures to accommodate the probe before palpation commences.

Palacio-Torralba and co-workers [20] evaluated the influence of the anatomical details of the patients in the outcome of the probing procedure. The patient-specific models showed the presence of the rectum, prostate, bladder and pelvic bone. Interesting, those organs were embedded in a 'box' (homogenous soft material) chosen to be comparable to the size of patient's pelvic cavity. One of the conclusions of the work was that the pelvic bone and the relative position of the bladder and prostate affects the force feedback during probing procedure and consequently the sensitivity of the method.

However, a comprise between accuracy in the force feedback and the time consuming of the FE simulations needed to be found. Therefore, rigid boundary conditions were applied for simulating the constraints of the pelvic bone without including in the model the bladder and the 'box' for simulating the interaction between the prostate and the surrounding soft tissues (Fig. 3-1(b)). As a result, it would be possible performed a

sensitivity analysis, which will be discussed later, with the aim of proving the concept of numerical diagnostic framework. It should be noted that, the mechanical characterization and modelling of the fascia is not a trivial task as it might expect a homogenization technique for estimating its apparent stiffness.

The rectum wall is not considered in the model, as its effect has been proven to be negligible when high probing depths are used [114]. Instrumented palpation was modelled using a rigid 'probe', with prescribed displacement (d) along the anterior-posterior axis repeated at a number of points, (p) (Fig. 3-1(b)).

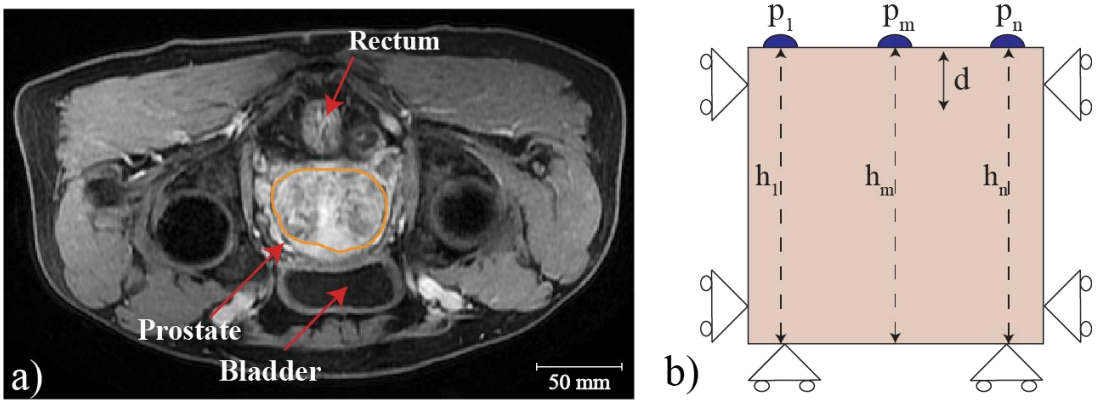

Fig. 3-1. The schematic of the simplified 'prostate' FE model. a) An MR image of the male pelvis, illustrating the anatomical features. The posterior surface can be probed through the rectum; b) The simplified FE model which represents the prostate tissue and its thickness values (h) at probing points. The constraints, which allow zero displacement conditions, were based on the anatomical features shown in a). At all probing points (p), a displacement of depth (d) was applied along the anterior-posterior axis and the reaction force calculated. Details of the thickness values and the width of the prostate model will be given later using appropriate examples.

The point-wise probing was considered to be quasi-static, using a strain rate lower than $0.01s^{-1}$, allowing the prostate tissue to be considered as a (hyper)-elastic material [62]. Subjected to such a quasi-static loading the observed stiffness is often referred to long-term modulus.

Moreover, in the literature, there is no clear evidence of which hyperelastic model could be exploited to characterize the mechanical behaviour of the prostate. In Chapter 2 section 2.3.2 has been reported that the biological tissues might show a non-linear behaviour under large deformation and hyperelastic models such as Mooney-Rivlin and Ogden might capture with higher accuracy the mechanical behaviour of the biological tissues compared to neo-Hookean. However, the deformation of the elements in FE simulations could be significant due to high strain values. In this case, the elements might become so distorted causing instability of the material (the Drucker stability condition is not met). As a result, convergence issues for the FE simulations may appear[6]. Therefore, the neo-Hookean model, which may lead to improve convergence if the material constants assume positive values, has been chosen to characterize the mechanical behaviour of the prostate undergoing probing procedure.

The neo-Hookean hyperelastic model was used for both cancerous and non-cancerous tissue, with strain energy function expressed as

$$U = C_1(\bar{I}_1 - 3) + \frac{1}{D_1}(J-1)^2 \tag{3-1}$$

$$D_1 = \frac{2}{K_0} = \frac{3(1-2\nu)}{\mu_0(1+\nu)} \qquad \text{and} \qquad \mu_0 = 2C_1 \tag{3-2}$$

where $\bar{I}_1$ is the first deviatoric strain invariants and J the total volume ratio (refer to Chapter 2 section 2.3.2). The remaining material parameters, C_1 D_1, are related to bulk modulus (K_0), initial shear modulus (μ_0) and Poisson's ratio (ν), as shown in Eq. (2). The prostate tissue was modeled as nearly incompressible material [136]. The elastic properties of prostate tissue were adopted from the work by Hoyt et al. [65], who measured the Young's moduli of the non-cancerous and cancerous tissues from *ex-vivo*

[6] http://dsk.ippt.pan.pl/docs/abaqus/v6.13/books/usb/default.htm?startat=pt05ch22s05abm07.html

radical prostatectomy samples as 17 kPa and 42.5 kPa, respectively. The Poisson's ratio of both tissue types is 0.49. As a result, after fitting the neo-Hookean model in Eq. (3-1) against the elastic properties mentioned above, the non-cancerous tissue had properties of C_1 (0.00285 [MPa]) and D_1 (7.067 [-]) and the cancerous tissue of C_1 (0.00712 [MPa]) and D_1 (2.827 [-]). The prostate was modeled as a homogenous material which might be justified by the experiments and statistical analysis performed by Krouskop et al. [64] where a non-significant variation of the Young's moduli between the anterior and posterior region of the prostate was identified. Moreover, the force values are influenced by the constitutive parameters, in our model C_1.and D_1. A variation of the 32% was identified in the force values once the parameters were multiplied by a factor of 2.5.

A justification for the choice of modelling the mechanical behaviour of the prostatic tissue using neo-Hookean was given previously. However, it could be important assessing the influence of diverse hyperelastic models in the force values. Liu et al. [119] provided a comparison between the error in fitting the experimental data obtained by compression of biological tissues (porcine kidney), using as hyperelastic models Arruda-Boyce, Ogden and neo-Hookean. A non-significant variation in the error values was identified between the three models for a displacement of 6mm.

The probe was modeled as a rigid material of diameter 10mm, and its contact with the prostate tissue was assumed to be frictionless [106]. A quasi-static displacement along the anterior-posterior axis was applied to the probe with depths ranging between 2 and 8mm. The location of the probing was at 5, 20 and 35mm considering as origin the edge of the prostate model. The FE model was meshed with 3-node linear triangular elements. The global size of the seed, which specifies the mesh density of the FE model, was 0.25. (mesh refinement was conducted to ensure cost-effective convergence of FE simulations)

and solved in ABAQUS (Dassault Systemes, Vlizy Villacoublay, France) using implicit quasi-static analysis.

3.3 Optimization algorithm

For the proposed inverse method, an FE model with 'initial guess' of the prostate 'thickness', h_i, was established, as illustrated above in Fig. 3-1(b), and an iterative process was executed to drive the initial guess to the target (i.e. the true solution), based on the difference between the reaction forces obtained from probing the prostate and the FE model being iteratively optimized.

To construct the optimization algorithm for estimating the prostate size, the Levenberg-Marquardt (LM) method was adopted [137]. It iteratively minimized an error function of reaction forces between the current FE model and the 'target' model:

$$\min \quad F = \sum_1^n \left(RF_{Target}^{(p_n)} - RF_{FE}^{(p_n)} \right)^2 \tag{3-3}$$

which denotes the difference between the sums of target reaction forces (of 'true' solution), $RF_{Target,}$ and those from the FE model being optimized, RF_{FE}, at all probing points (p_n). The parameters, i.e. the thicknesses (h), were those to be optimized against the first derivatives of the error functions. In the 2D formulation illustrated in Fig. 3-1(b), the Jacobian matrix (J) can be numerically calculated by perturbing each variable, h_n, individually:

$$J^{(i)} = \begin{bmatrix} \frac{F_1\left(h_1\right) - F_1\left(h_1 - \Delta h_1\right)}{\Delta h_1} & \cdots & \frac{F_1\left(h_n\right) - F_1\left(h_1 - \Delta h_n\right)}{\Delta h_n} \\ \vdots & \ddots & \vdots \\ \frac{F_n\left(h_1\right) - F_n\left(h_n - \Delta h_1\right)}{\Delta h_1} & \cdots & \frac{F_n\left(h_n\right) - F_n\left(h_n - \Delta h_n\right)}{\Delta h_n} \end{bmatrix} \tag{3-4}$$

where i represents the i_{th} iteration, and F_n, h_n and Δh_n denote the error function, the thickness variable and the perturbations in the thickness variable at n_{th} probing point, respectively. The maximum change of Δh was set to be 0.1 mm to ensure stability of the algorithm and accuracy of solving the first derivatives for the Jacobian matrix. The updated parameters, h_{i+1} used in the following iteration step (i+1) were obtained from:

$$H^{(i)} = J^{(i)^T} * J^{(i)}; \tag{3-5}$$

$$\delta^{(i+1)} = \left(H^{(i)} + \lambda^i * I\right)^{-1} * \left(J^{(i)^T} * F^{(i)}\right); \tag{3-6}$$

$$h^{(i+1)} = h^{(i)} - \delta^{(i+1)} \tag{3-7}$$

where H is the Hessian matrix (i.e. the square matrix of second-order partial derivatives), I the identity matrix, δ the increment of the variables h, and λ is the damping factor, which was used to ensure the robustness of the optimization algorithm. It is worth noting that the proposed optimization algorithm only estimates the size of the prostates at each probing point. As a result, the anterior surface of the prostate model is estimated with a cubic spline function using the thickness values, h_i.

The damping factor, λ, is the key parameter that controls the efficiency and accuracy of the convergence of the LM algorithm [138]. If the error function in Eq. (3) increases between two consecutive iterations, the updated parameter h_{i+1} will not be accepted. As a result, the damping factor will increase in order to drive the algorithm towards the direction of gradient descent, which may lead to slower but guaranteed convergence to mimima. Otherwise, the damping factor is reduced leading to faster convergence. Thus, the algorithm is capable of alternating between a slow descent and a fast convergence, depending on the evolution of the error function.

The initial value of the damping factor, λ, was defined as the maximum value among the diagonal elements in the initial Hessian matrix *H*, as it can be related to the eigenvalues [139]. The parameter that dictates if the damping factor is to be increased or reduced is the gain ratio, ρ, which is defined as the ratio between the actual reduction in the error and the predicted reduction in error, based on the chosen increment δ:

$$\rho^{(i+1)} = \frac{\left(\left\|F^{(i)}\right\|^2 - \left\|F^{(i+1)}\right\|^2\right)}{\left(\delta^{(i+1)^T} * \left(\left(\lambda^{(i)} * \delta^{(i+1)}\right) - \left(J^{(i)^T} * F^{(i)}\right)\right)\right)} \tag{3-8}$$

whose absolute value is between 0 and 1, although it can be either positive (indicating a need to decrease the damping factor) or negative (to increase the damping factor):

$$\lambda^{(i+1)} = \lambda^{(i)} * \max\left(\frac{1}{3}, \left(1 - \left(2 * \rho^{(i+1)} - 1\right)^3\right)\right),\ v^{(i+1)} = 2;\ if\ \rho^{(i+1)}\ is\ positive$$

$$\lambda^{(i+1)} = \lambda^{(i)} * v^{(i)},\ v^{(i+1)} = v^{(i)} * 2;\ if\ \rho^{(i+1)}\ is\ negative \tag{3-9}$$

where the variable v was used to increase the value of the damping factor, of a multiplier of 2, when the gain ratio was negative.

3.4 Solution of the inverse procedure

The proposed procedure of inverse analysis is illustrated in Fig. 3-2, aimed to minimize the difference between the target reaction forces (e.g. from an instrumented palpation measurement) and their counterparts from the FE model, based on quasi-static point-wise palpation over the posterior surface of the prostate through the rectum.

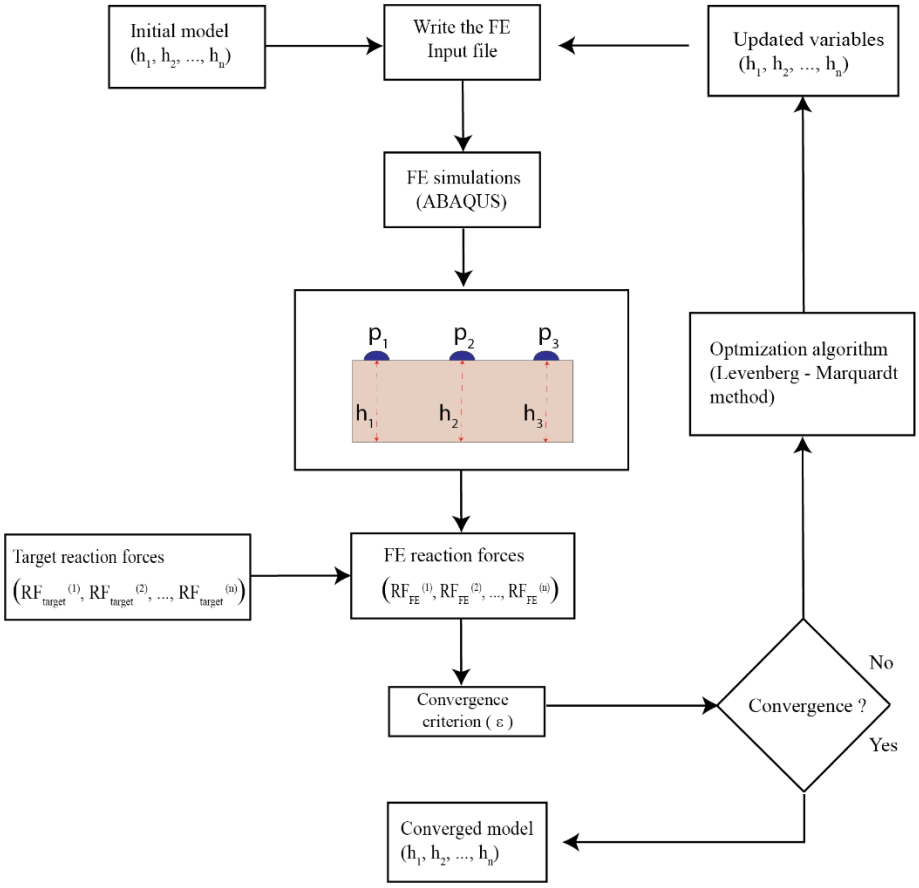

Fig. 3-2. Flowchart of the proposed inverse FE framework.

The iterative process is terminated when the convergence criterion is met, where the difference between two sets of reaction forces:

$$\varepsilon = \max\left(\frac{\left|RF_{target}^{(p_n)} - RF_{FE}^{(p_n)}\right|}{RF_{target}^{(p_n)}}\right), \quad n = 1, \dots, n \text{ (probing points)} \tag{3-10}$$

is smaller than the convergence threshold, 0.1% .

The essential premise of the technique is that the presence of tumor nodule will cause distortion of the stress field, hence different reaction forces at one or more probe points. Since the presence of a tumor nodule is not known at the time of probing, the prostate size estimated from the inverse analysis is either. **i)** the 'true' size, if there is no tumor

nodule present, or **ii)** a ‘distorted’ size, if a tumor nodule is present. Therefore, tumor nodule identification requires a robust method to distinguish between these two cases.

Here, it is hypothesized, and later validated, that it is possible to identify the presence of the tumor nodule by analyzing the reaction force data using multiple probing depths. This hypothesis is based on the likely interplay between the probing depth and the existence of a tumor nodule, whereby any stress distortion is likely to be ‘amplified’ by deeper probing. Therefore, by increasing the probing depth, one could examine the estimated area of the prostate with respect to increasing probing depth and conclude that, if the area estimation varies, a tumor nodule is present.

3.5 Sensitivity study on tumour-free model

In this section, a sensitivity study is carried out for prostate volume determination against a target of a tumour-free gland of idealised (rectangular) shape. Two dimensions of sensitivity were tested in the idealised tumour-free model shown in Figure 3-1(b); the effects of the initial guess of prostate size and number of probe points, and the effect of depth of probing.

As shown in Fig. 3-2, an initial guess in the size of the prostate $h_1 \ldots h_n$ is required to initiate the inverse algorithm, therefore the sensitivity of the algorithm to the initial guess needs to be explored. For simplicity, all target values of h are identical at 35mm (i.e. a rectangular target) and the size range of the initial guess was chosen to be between 10 and 60 mm, a little wider than that of adult prostate (20 to 50 mm). Probing to a 5 mm depth, at 3, 5 or 7 points (i.e. 15, 6, 4.3 mm horizontal spacing) was carried out on the rectal surface of the model.

Fig. 3-3(a) shows the relative errors in estimated areas of prostate using the proposed inverse FE method, as the initial guess is varied. Convergence is reached (with relative errors less than 0.1%) regardless of the initial guess chosen, although the rate of convergence is influenced by how far the initial guess is from the true solution, as might be expected.

Fig. 3-3(b) shows the effect of number of probing points, i.e. spatial 'resolution'. Here, convergence is achieved in all three cases, although it is worth noting that the size of the Jacobians in Eq. (4) increases with the power of the number of probe points with consequences for computational cost.

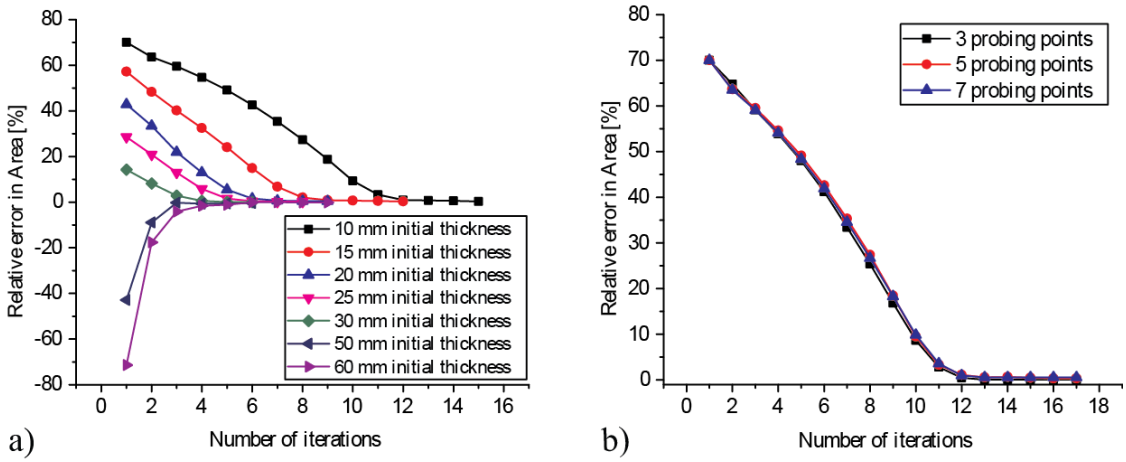

Fig. 3-3. Estimation errors in prostate size for a 35mm target, when the initial guess and the number of probing points is varied. The relative error in area is defined as the difference between the area of the equivalent prostate model and the target. The area of the equivalent prostate model is identified in the last iteration, when the inverse procedure reaches convergence (refer to equation 3-10).

Fig. 3-4 shows the effect of varying the 'target' thickness from 20 mm to 95 mm and the probing depth from 1 to 9 mm. Five probing points were used in all cases, with an initial thickness of 10 mm. All 56 cases are presented in Fig. 3-4(a), where the vertical bars

illustrate the relative error in estimated area of prostate. In general, the larger the 'target' prostate model is (Fig. 3-4(b)) or the greater the probing depth is (Fig. 3-4(c)), the higher the estimation error, although all cases reach convergence, most with under 1% error. Thus, the proposed method can estimate the total area of a tumour-free prostate, irrespective of the probing depth used.

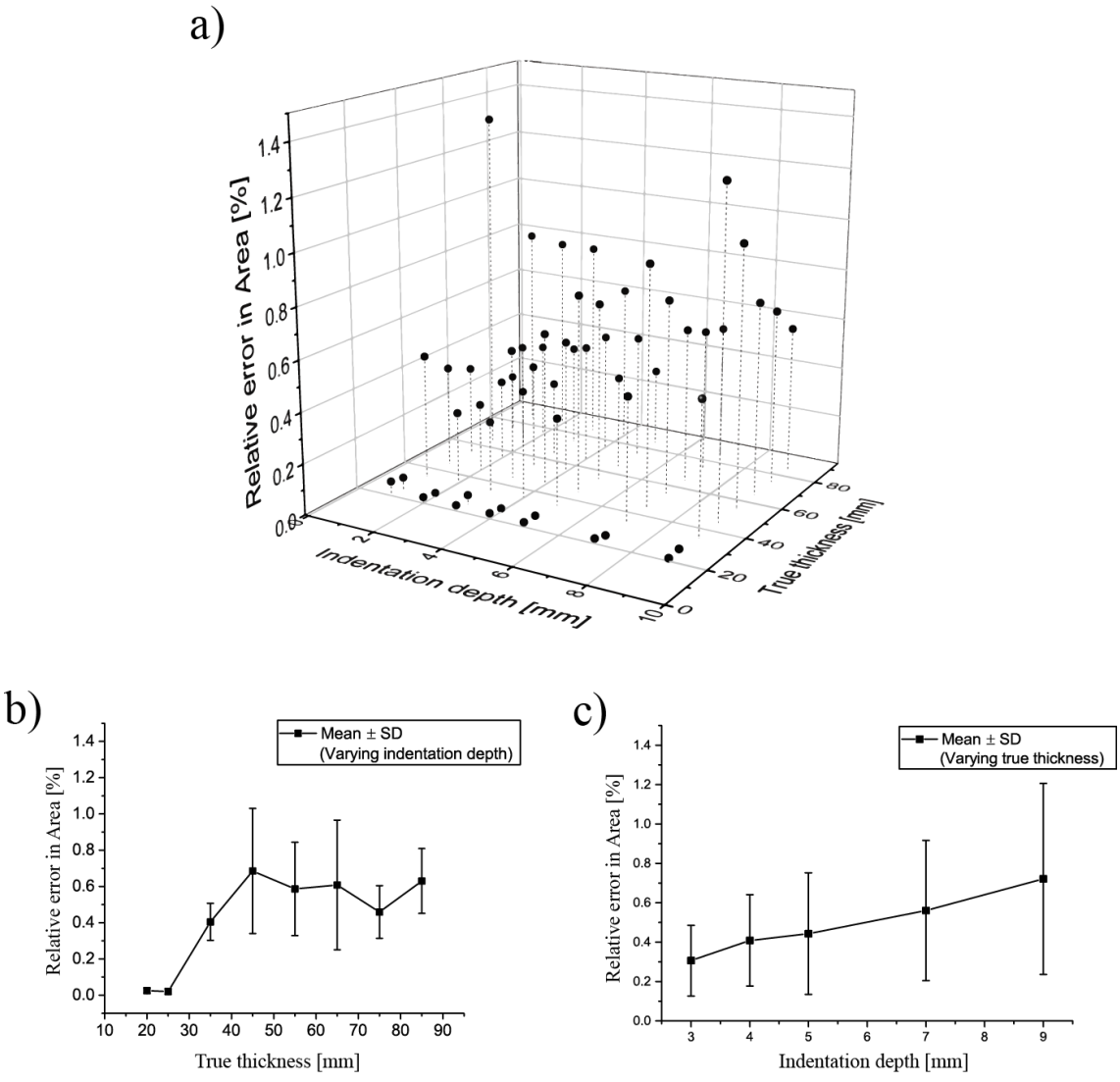

Fig. 3-4. Relative errors in area estimation when the target size and probing depth are varied.

3.6 Identification of tumor nodule

In this paragraph, the proposed methodology will be applied to cases where a tumor nodule is present in the model, in order to test the feasibility of nodule identification. Fig. 3-5(a) shows a schematic of the model, where a tumor nodule of diameter 15mm and with Young's modulus a factor of 2.5 higher than the 'matrix' [66] is placed at a depth of 10.65mm from the top (posterior) surface. This represents a readily palpable tumour [98] so is a reasonable test case for the ability to distinguish the effects of a local increase in stiffness from an increase in thickness in the idealized prostate shape.

Probing was carried out at three points (p_1, p_2 and p_3), using a probing depth of 8mm. It should be noted that, the results of the inverse procedure are not affected by the values chosen for the initial thickness even for a prostate model which show the presence of a cancerous nodule. Therefore, the initial thickness was 10mm for consistency with the analysis showed in the previous section. A comparison between the reaction force profiles of models with or without the tumor nodule, is shown in Fig. 3-5(b). The values of reaction forces are significantly higher when the stiff tumor nodule is present. This is also reflected in the stress distributions under probing at location p_2, Figs. 3-5(c) and (d). Furthermore, the reaction force values in the homogenous case are lower once the probing is performed close to the edges of the prostate model. The zero displacement conditions influence the reaction force values. For instance, once the probing is performed in p1, the effect of the constraint applied on the opposite side of the prostate model could decrease significantly. Once the probing is performed in p3, both constraints on the edges influence the displacement, therefore, the reaction force is higher in the middle of the force profile.

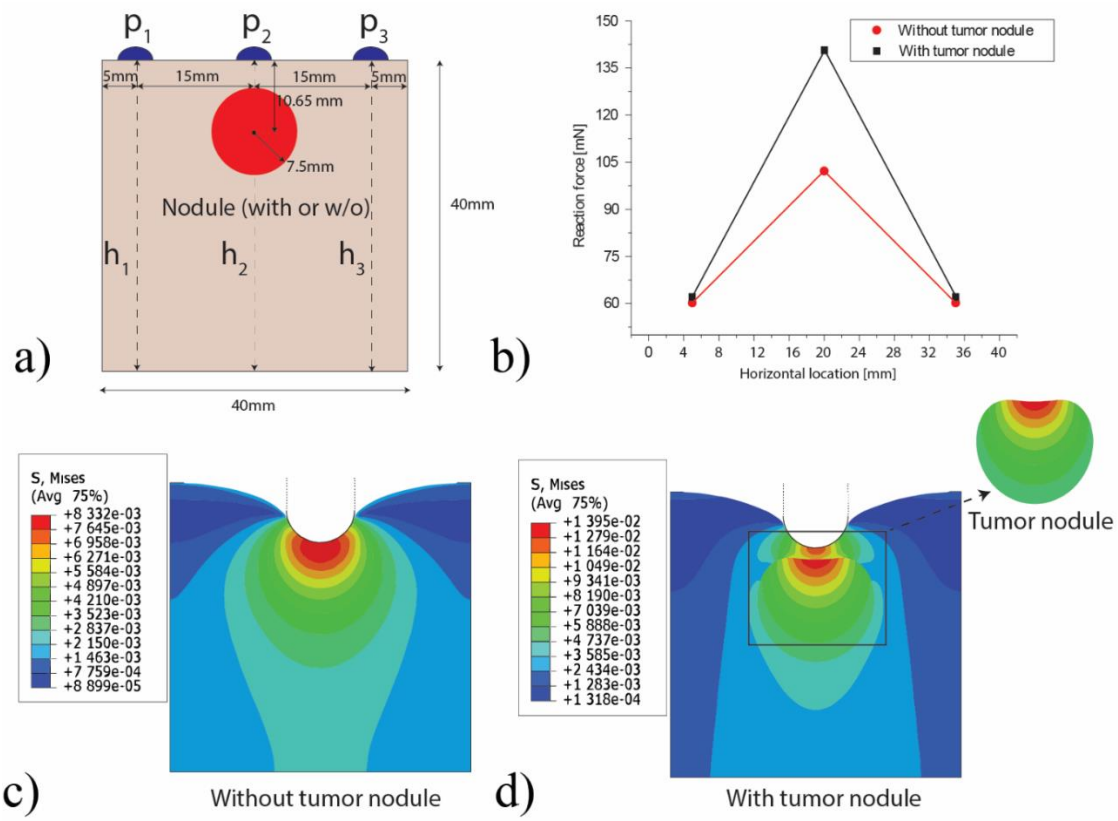

Fig. 3-5. The comparison between simplified prostate models with and without a tumor nodule. The size of 'prostate' model is 40mm × 40mm. a) Schematic of the model, with or without the Mechanical Imaging of Soft Tissues with a Highly Compliant Tactile Sensing tumor nodule; b) reaction force profiles; and (c-d) the stress distributions in two models. Colorbar unit: MPa.

Using the same models as Fig. 3-5(a) as the 'target', the method was applied with a second probing depth of 2mm. The results for the four cases, i.e. with and without nodule and 2mm and 8mm probing depths, are illustrated in Fig. 3-6. When no tumor nodule is present in the target, Fig. 3-6(a), the estimated prostate has a much flatter profile at the anterior surface than when a nodule is present, Fig. 3-6(b). As hypothesized, increasing the probing depth amplifies the effect of the tumor nodule on the stress field, leading to an even greater underestimation in prostate area. This is illustrated by the error in area estimation illustrated in Fig. 3-6(c). In tumour-free cases, when the probing depth changes from 2mm to 8mm, the estimated area of prostate does not change significantly (errors of

0.08 % and 0.06 %, respectively). However, when the tumor nodule is present, the error in estimated area of prostate increases drastically, and even more so when a deeper probing is used. This demonstrates the potential of using the proposed inverse method for tumor nodule identification by using a range of probing depths.

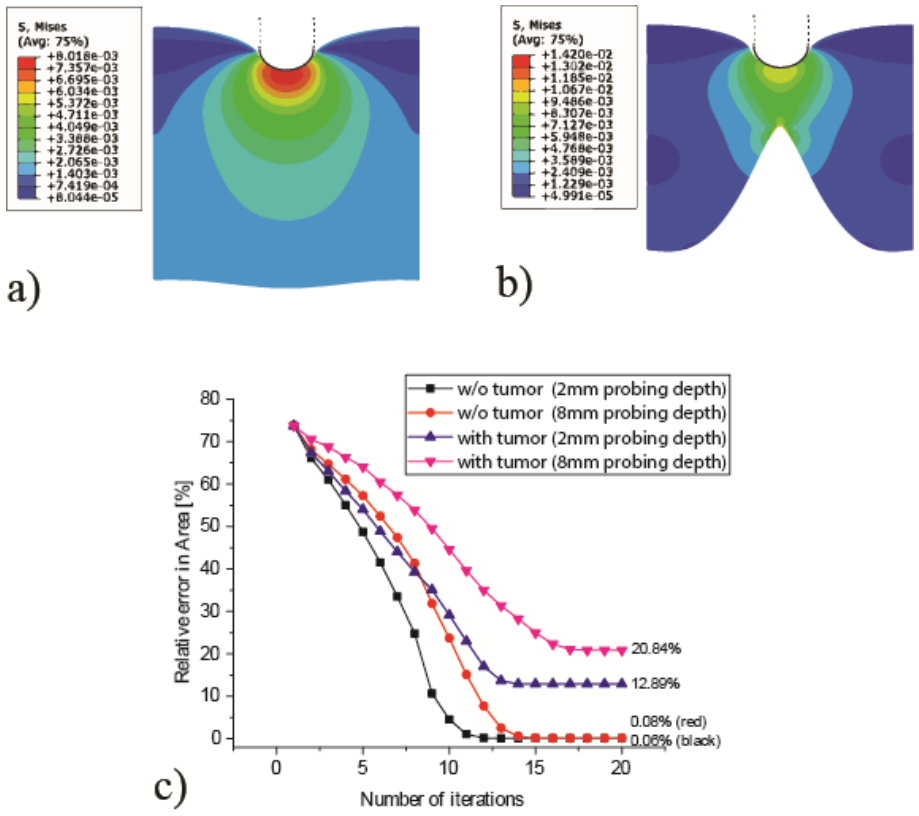

Fig. 3-6. Comparison of simplified models for probing depths of 8mm and 2mm. Distributions of von Mises stress in converged geometries under 8mm probing depth (a- tumor free ; b – with tumor nodule). c) Convergence and error for both probing depths with and without tumour nodule. Initial guess:10 mm. Colorbar unit: MPa.

3.7 Prostate characterization and tumor identification – a feasibility study

To demonstrate the feasibility of the proposed framework in a realistic situation, a prostate model was reconstructed (using Scan-IP, Simpleware, Mountain View, USA) from the MR image shown in Fig. 3-7(a) and the same palpable nodule as used in Section

3.5 superimposed onto the model, Fig. 3-7(b). The boundary conditions were applied as before, considering the anatomical features surrounding the prostate. Probing was performed vertically at three locations on the posterior surface, as indicated in Fig. 3-7(b), using probing depths ranging from 4 to 8mm with and without the palpable tumor. This arrangement is a reasonable facsimile of actual patients on whom instrumented palpation measurements and FE simulations have been made *in vivo* [20].

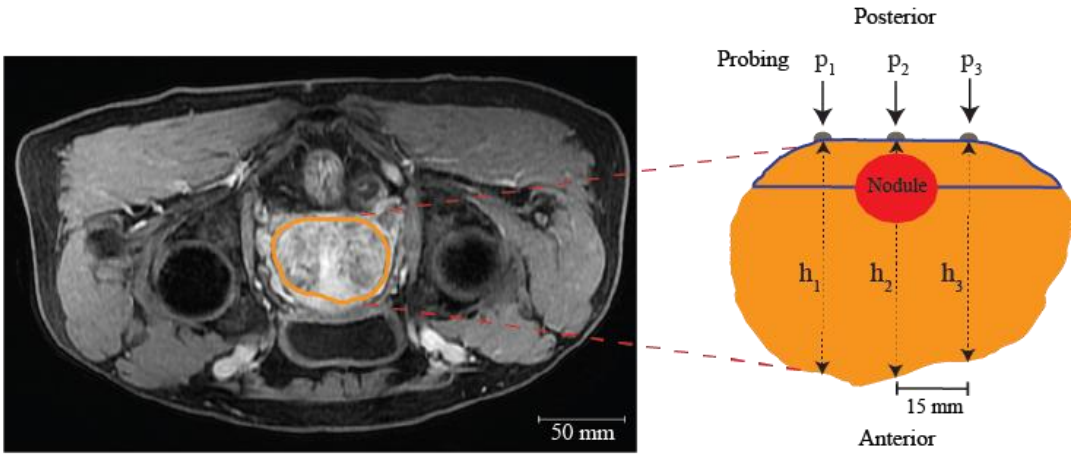

Fig. 3-7. Feasibility study model (a) Segmented MRI pelvic image (b) Model derived from image with 15 mm diameter nodule located 10.65 mm below posterior surface (surface to the nodule center). The three target values of prostate thicknesses are: h_1=51.31mm; h_2=52.69mm and h_3=48.40mm. The initial guess (blue boundary) has a depth of 10.07mm at p2, equivalent to a total area of 468.03 mm^2. The total prostate model has an area of 2812.21 mm^2.

Fig. 3-8 summarises the estimated areas of the MRI-based prostate model for the five probing depths, with and without the tumor nodule. In the tumor-free models (in black), the estimated areas of prostate are close to the target with little variation between probing depths. By contrast, even when the probing depth is low the presence of tumor nodule leads to underestimated prostate sizes, worsening as the probing depth increases. It is also interesting to note that most of the converged models (even those where a tumour is present) reflect the asymmetry of the target (h_1>h_3). Most importantly, Fig. 3-8 demonstrates that, when assessing the response of prostate tissue to probing from the

posterior side, one can vary the probing depth and use the obtained reaction forces to estimate the ‘apparent’ prostate size using the proposed method. If the estimated prostate size remains relatively constant with little variation when the probing depth is varied, the examined prostate sample can be regarded as homogeneous, meaning that there is no palpable lesion. Otherwise, the consistent variation in the estimation of prostate size, due to the disturbance in the stress field caused by the appearance of a stiff nodule, could serve as a primary indicator of a tumor.

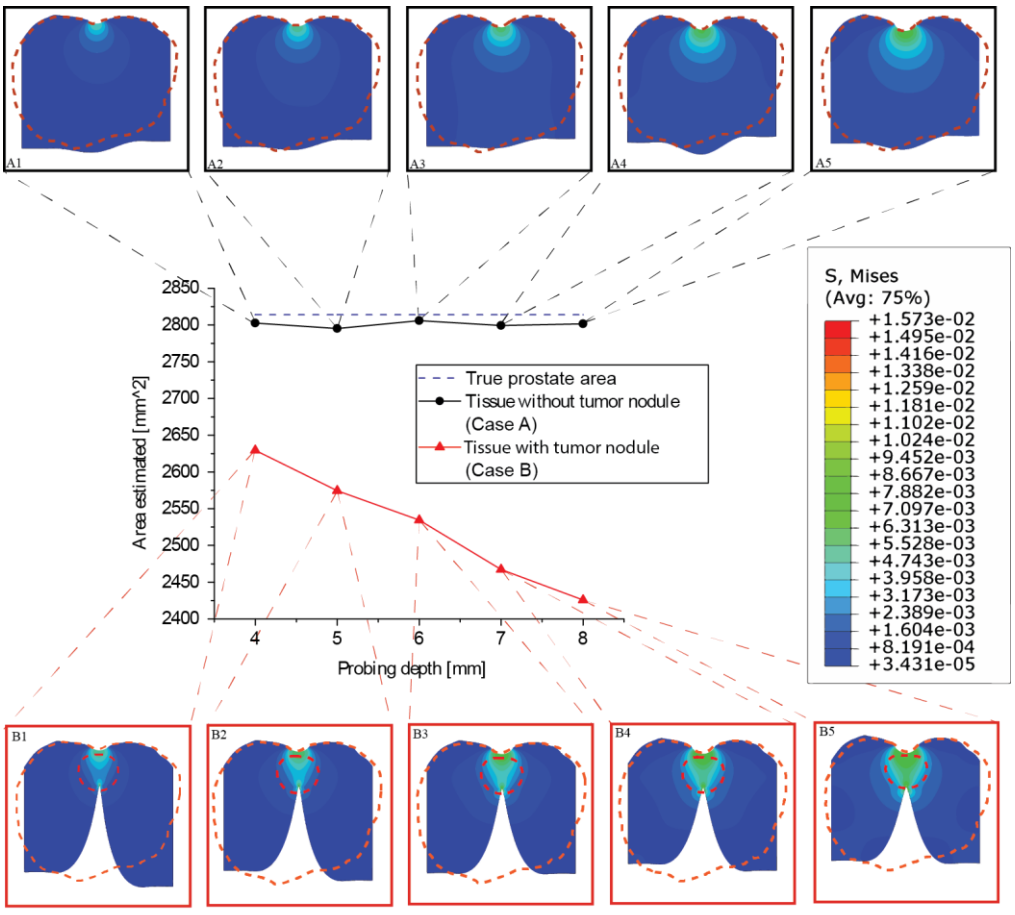

Probing depth	4 mm	5 mm	6 mm	7 mm	8 mm
Case A	2803 mm^2	2795 mm^2	2806 mm^2	2799 mm^2	2801 mm^2
Error	0.40%	0.67%	0.29%	0.52%	0.44%
Case B	2629 mm^2	2574 mm^2	2534 mm^2	2467 mm^2	2426 mm^2
Error	6.58%	8.51%	9.93%	12.33%	13.80%

Fig. 3-8. Results of the feasibility study model of prostate, with and without an idealized tumor nodule. The red dash lines indicate the boundaries of 'true' prostate or tumor nodule. Colorbar unit: MPa.

3.8 Concluding remarks

There is a need of robust and effective methods for the quantitative interpretation of data from mechanical probing in order to identify inhomogeneities in soft tissue. This work has focused on the identification of tumor nodules in the prostate by trans-rectal instrumented probing.

A finite-element based inverse method has been proposed to estimate the size of the prostate using reaction force data at a number of probe points on the posterior surface of the prostate. A sensitivity analysis showed that the initial guess of the shape and the interval between probing points have little influence on the estimated prostate size, showing the robustness of the proposed method.

Importantly, it was hypothesized, and later validated, that the presence of tumor nodule that is of higher modulus can be identified by conducting probing at various depths, without a *priori* anatomical knowledge of the prostate such as volume and geometry. This was possible because the estimate of prostate size changes significantly as the probing depth is varied if a tumour is present, but remains constant when no tumor nodule is present.

The accuracy of the results is not affected by the initial conditions which means that the inverse procedure can be applied irrespective of the size, geometry, and boundary conditions of the organ under investigation. Increasing the number of indentation points would improve the quality of the diagnosis, although it is necessary to explore the accuracy and sensitivity of the method to features of the cancer nodule, such as its diameter, depth, and mechanical properties

The computational framework has a limitation in the material properties which were assigned for characterizing the mechanical response of the soft tissue. The tissue has been

modeled as a homogeneous, isotropic and incompressible material, however, the material properties of the biological tissues may be more complex. For instance, the healthy matrix has an elastic modulus which can vary due to the presence of benign condition, calcification or inflammation of the tissue [64]. More importantly, the stiffness of the tumor nodule can evolve depending on their development stages [62]. Furthermore, the prostatic tissue often presents certain time-dependent behaviour, due to the presence of liquid in the tissue microstructure [39].

Another limitation is in the choice of the rigid boundary conditions applied to the prostatic model. The prostate is encapsulated among connective tissue, muscles and fat. Therefore, certain deformation of the prostate is allowed along both axes. During experimental measurements the probe might show a deformation and friction, once in contact with the indented surface of the prostate. Therefore, the sensitivity of the method may be affected by such effects.

The results shown in this chapter were obtained using a 2D model so that the inverse procedure needs to be further validated in a more realistic scenario of using 3D prostate models. Moreover, the inverse method was assessed using probing values which were obtained from FE simulation. The framework needs an experimental validation using in vivo or ex vivo. Some limitations mentioned above will be addressed in the following chapters. In the next chapter a sensitivity analysis for the tumor nodule detectability, using the proposed framework will be carried out using realistic prostate models reconstructed from MRI data.

Chapter 4

Sensitivity Analysis of Inverse FE Framework

Contents

4.1 Summary

In Chapter 3 a computational framework was developed to estimate the volume of the prostate and to detect the existence of the PCa nodule, based on force profile from instrumented probing, without *a priori* knowledge of the nodule geometry and location. The method could provide the area of the prostate if the sample is homogeneous (i.e. prostatic tissue without tumor nodule - healthy). Instead, a 'variance' in the areas estimated for multiple probing depths due to the heterogeneity of the sample (i.e. PCa nodule) will be shown, indicating the existence of PCa nodules in the prostate. Moreover,

the accuracy of the prediction can be heavily influenced by the nodule parameters such as lateral position, depth, size and stiffness ratio.

In this chapter, the values and combinations of the nodule size, depth and stiffness ratio within a clinical range are varied and their influence in the binary classification for the presence/absence of tumor nodule, using the measurements of the areas as outcome of the inverse FE procedure, is evaluated. Furthermore, the feasibility of the proposed method using prostate models reconstructed from MRI images, will be assessed.

4.2 Sensitivity analysis – random prostate models with values of the nodule parameters within a clinical range

The prostate model, in which a PCa nodule is present, is illustrated here in Fig. 4-1. The width and height of the sample were chosen to be 40 mm, representative of the physiological size of the prostate.

The influence of the stiffness ratio was assessed as first. A stiffness of 25.5, 34, 42.5, 51 and 59.5 kPa was assigned to the circular PCa nodule, and the stiffness of the healthy prostate tissue was kept as a constant of 17 kPa. As a result, the stiffness ratio was varied between 1.5, 2, 2.5, 3 and 3.5. Those values were decided based on the experimental evidence discussed in more details in Chapter 2 section 2.3.3, which suggested how the stiffness of the tumour nodules might increase due to later development stages of PCa. For all cases, the nodule size and depth were 10 and 1 mm, respectively. The PCa nodule and healthy matrix were modeled as described in Chapter 3 section 3.2. The reaction force values were recorded when the probe reached a displacement of 4, 6 and 8 mm from the posterior surface along the anterior-posterior axis. The probing procedure was simulated

using boundary conditions, probe size, contact properties and mesh quality as described in Chapter 3 Section 3.2.

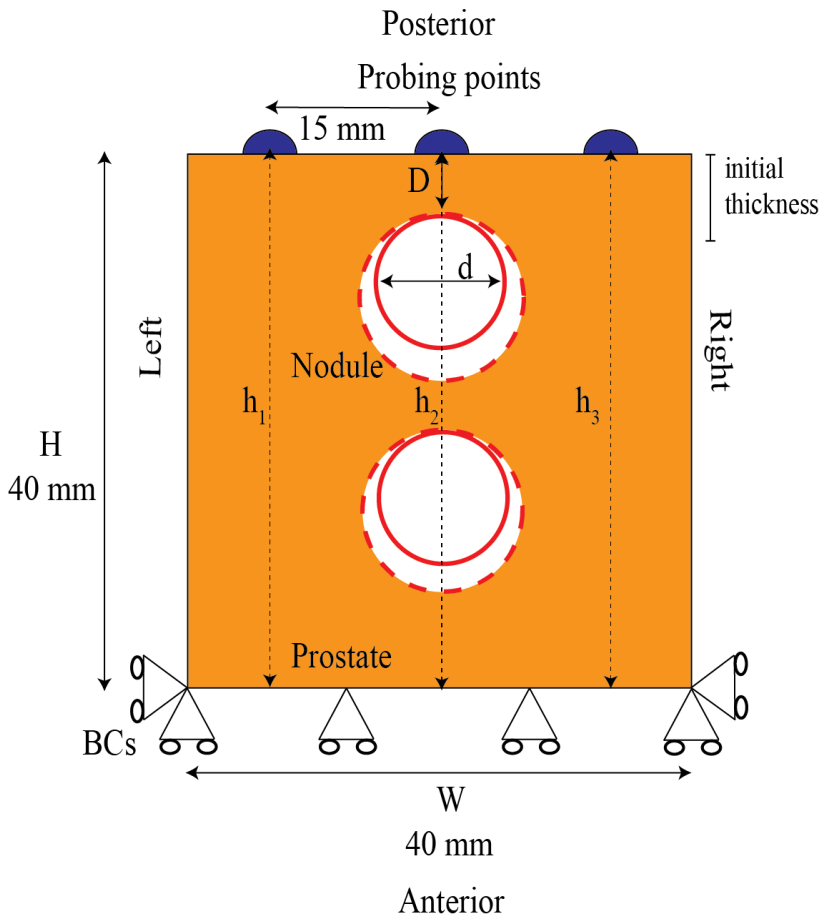

Fig. 4-1. Prostate sample characterized by the presence of stiff nodule (with depth D and diameter d) chosen for obtaining the force values which were in input to the inverse procedure. Therefore, the framework can estimate the thickness along the location of the probing points (h_1 , h_2 , h_3). It should be noted the initial thickness of 10 mm defined in the equivalent FE model for the first iteration.

The influence of the number of probing points and the initial conditions was evaluated in Chapter 3 section 3.5. The results showed that the accuracy of the areas estimated does not vary due to the initial conditions. Therefore, in this study, the areas estimated were obtained using an initial thickness for the equivalent FE model of 10 mm. Furthermore, the results showed that the inverse procedure can reach convergence with the same accuracy for a number of probing points which could be 3, 5 and 7. Moreover, the time-

consumption of the inverse procedure may increase significantly when a higher number of probing points was used. As a result, the number of probing points chosen for the following analysis in this chapter was 3 (h_1 , h_2 , h_3), representing a good compromise between the sensitivity of the probing procedure and computational cost for the framework.

The analysis was further assessed by varying the nodule depth and size of the idealised PCa nodules. The nodule depth was defined as the distance between the indented surface and the top edge of the nodule (D). The range assigned for the nodule depth was between 1 to 17.7 mm. It should be noted that, the tumour nodule might occur deeper in the prostatic tissue. However, the force profile would not be distorted by the presence of the stiff nodule. Therefore, the inverse procedure would provide as outcome a false negative. As a result, the area estimated would show similar value than the homogenous case as already discussed in the limitations of the diagnostic framework in Chapter 3. For each case of the nodule depth, the size of the nodule was varied too, with values of the nodule diameter (d) being 2, 5, 7, 10, 12 or 15 mm. Moreover, a stiffness ratio of 1.5, 2.5 and 3.5 was set up for each combination. In Chapter 3 section 3.6, the geometrical index such as the 'variation' of the areas estimated using multiple probing depths showed promise for predicting the presence of tumor nodule in the prostate sample. Therefore, the probing procedure was performed for the 144 cases using 6 diverse values of probing depths (2, 3, 4, 5, 6 and 8mm). As a result, a total of 864 cases was generated for carrying out the sensitivity analysis for the nodule parameters which can influence the capability of the diagnostic framework in classifying the presence/absence of tumor nodule using palpation procedure.

In addition, a feasibility study using a prostate model reconstructed from MRI images with and without the presence of a tumor nodule was carried out, as illustrated in Fig. 4-

2. The methods used for simulating the prostate model in FE were kept the same as the previously used in Chapter 3.

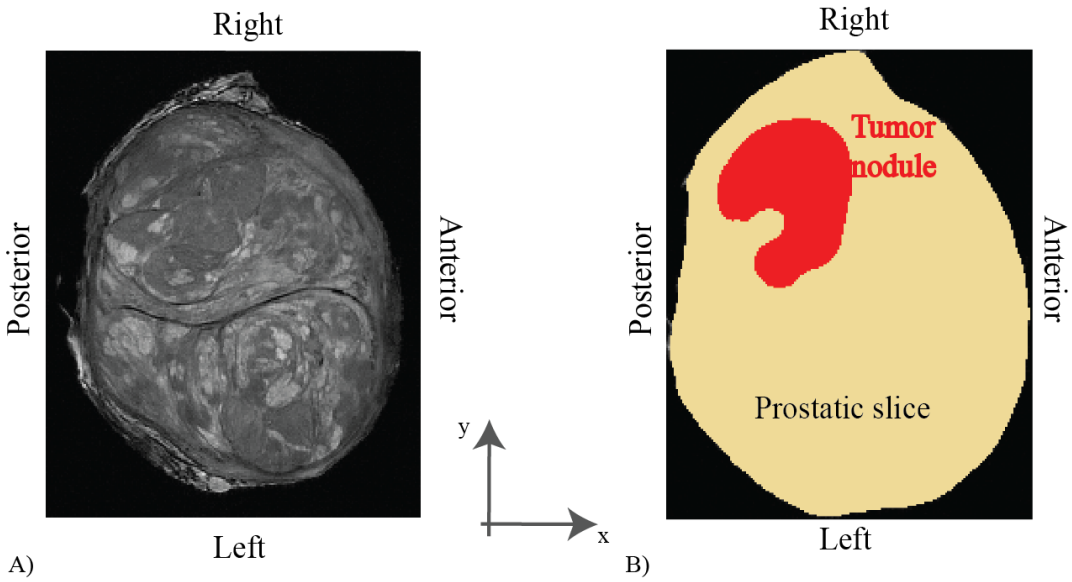

Fig. 4-2. MRI image of an *ex-vivo* prostate and the segmentation of the cancerous nodule and healthy matrix.

In summary, this chapter, in its first part, will further investigate the interplay between the size and depth of the PCa nodule and its stiffness ratio to the healthy tissue, particularly their influences on the identification outcome of the proposed methods. At the end of this chapter, a feasibility study using models reconstructed from the Magnetic Resonance images will be carried out to explore the role of such 'interplay' in a clinically-relevant scenario.

4.3 Inverse FE framework – Influence of stiffness ratio in the areas estimated

Fig. 4-3 shows the results of the inverse procedure for input in force obtained by probing a prostate sample with a nodule characterized by diverse values of stiffness (Fig. 4-3 (A)).

Fig. 4-3 shows how the relative error in predicted area increased when a higher stiffness ratio between PCa and healthy tissue was used. The reason can be reflected in the force profiles, which were used as inputs to the inverse procedure. The force values increase for a stiffer nodule (Fig. 4.3 (C)). As a result, the areas estimated for the equivalent FE model became smaller (Fig. 4-3 (B)), as already discussed in Chapter 3. Interestingly, when the stiffness ratio of 1 is used, i.e. there is no PCa nodule at present, the predicted prostate areas remained constant regardless of the indentation depth used. In conclusion, the stiffness ratio can greatly influence the capability of the proposed framework in classifying the PCa nodules. For a higher stiffness ratio, the error in area prediction increased, indicating that the capability of the framework in detecting PCa nodules may improve.

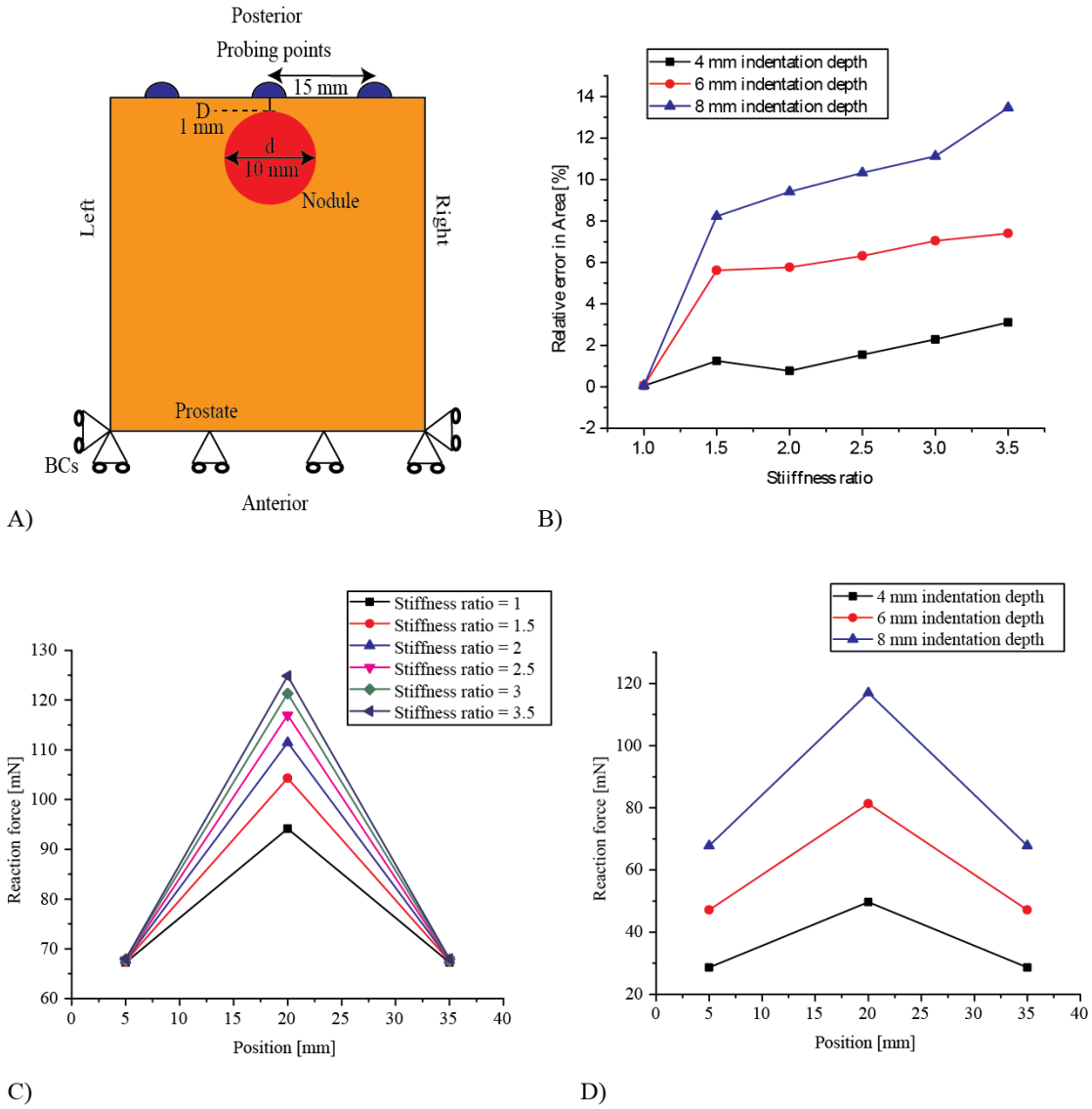

Fig. 4-3. A) Prostate sample which shows a stiff nodule with size of 10 mm and depth of 1 mm which underwent probing procedure. B) Results of the inverse procedure for the prostate sample characterized by a nodule with diverse stiffness values. C) Results of the probing procedure for five values of stiffness ratio and an indentation depth of 8mm. D) Results of the probing procedure for three values of probing depth (4, 6 and 8 mm) and a stiffness ratio of 2.5.

4.4 Inverse FE framework – Role of the interplay between the nodule depth and size

The previous results indicated a strong influence of the stiffness ratio in the estimated areas, however in only one prostate model whose PCa nodule has only one set of depth and size. Here, the roles of the depth and size of PCa nodules are further explored, as

shown in Fig. 4-4. where diverse combinations of PCa size and depth (6 values for the nodule size and 8 for the nodule depth) and a stiffness ratio of 2.5 were used.

The results showed that the error in estimated area increased for nodules with a larger size but the error decreased when the nodules located deeply into the prostate sample (Fig. 4-4 (B-C)).

Therefore, the proposed framework showed higher sensitivity in detecting tumor nodules which were closer to the indented surface and/or show a large size. For those cases, the error in area could reach as high as 20% (Fig. 4-4 (A)). In contrast, the nodules, with small size and/or located deeply into the prostate sample, were still challenging to detect as their influence in the force profile was neglectable. As a result, the outcome for those cases was similar to a homogeneous prostate (i.e. with no PCa nodule), so that the error in estimated area tends to zero. In conclusion, the interplay between the nodule size and depth can significantly influence, as one would expect, the outcome of the inverse analysis and the classification of PCa nodules.

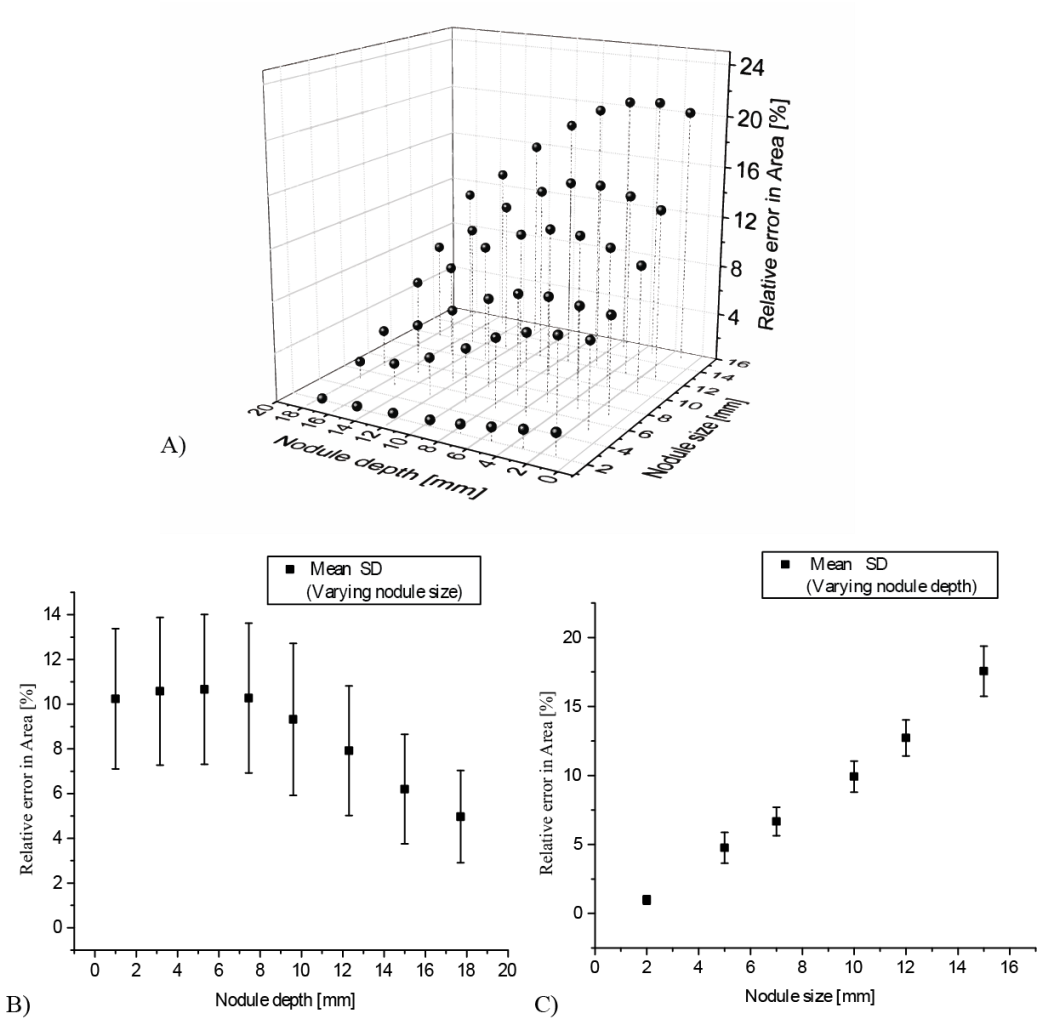

Fig. 4-4. Results of the inverse procedure for a prostate sample characterized by diverse combinations of nodule size and depth (48 combinations). The stiffness of the nodule was 42.5 kPa and the force values were obtained using a probing depth of 8 mm.

4.5 Quantification of the limits in detecting the tumor nodule by the inverse FE framework

Following the studies above, it would be of interest to find out the limits in the capability of the proposed methods in detecting the presence of a PCa nodule, in terms of its size, depth and the stiffness ratio. Here, a total number of 48 combinations of the nodule size and depth was used, along with 6 probing depths and 3 stiffness ratios, leading to a dataset of 864 cases being studied here.

Fig. 4-5 shows the results of all 864 cases, which were divided into 3 groups based on their stiffness ratio. It should be noted here that, in the 3D plots, one data point represented 6 cases with varying probing depth and the value of that data point was in fact the mean value among the 6 error values in area estimation. From the figure, the framework showed an increased capability in detecting nodules which were located closer to the indented surface and/or with a larger area. For those cases where the nodule was located deeply and/or with a small PCa nodule, the 'error' in area prediction becomes zero, meaning that the proposed methods believed the examined prostate model to be a homogeneous one without the presence of PCa nodules.

Fig. 4-5 (D-F) shows the same results discussed previously, albeit using a 2D fitted 'contour' representation, i.e. a top view of the figures to the left. Once again, the stiffness ratio between the PCa nodule and the healthy prostate tissue is proved to be critical – the higher the stiffness ratio, the better the detectability becomes (as illustrated by the increasing area in non-blue colours). What this means is that, when a PCa nodule has a higher stiffness, which may be correlated to later development stages of PCa, smaller and deeper PCa nodules may be detected, leading to an improved sensitivity of the proposed method. It should be noted that, the sensitivity in some cases decreases with the increase of the tumour size. The LM algorithm used to minimize the error function does not guarantee convergence to a global minimum (smallest value of the error function on its entire domain), instead, the method might find a local minimum [137]. This might justify the results in Fig. 4-5 wherein some cases the error in area decreases for larger nodule, which is in contrast with the conclusion achieved in the previous chapter.

In conclusion, the ’error’ in estimated area could be used as an index for classifying prostate models with PCa nodules. However, the accuracy in such classification may be influenced by the interplay between the nodule parameters such as size, depth and stiffness ratio. The analysis showed that those PCa nodules located deeply and/or with a small size are challenging to detect. Moreover, the classification showed good accuracy for nodules which are characterized with a diameter greater than 8 mm and a depth smaller than 12 mm, in a scenario where the stiffness ratio is equal to or greater than 2.5.

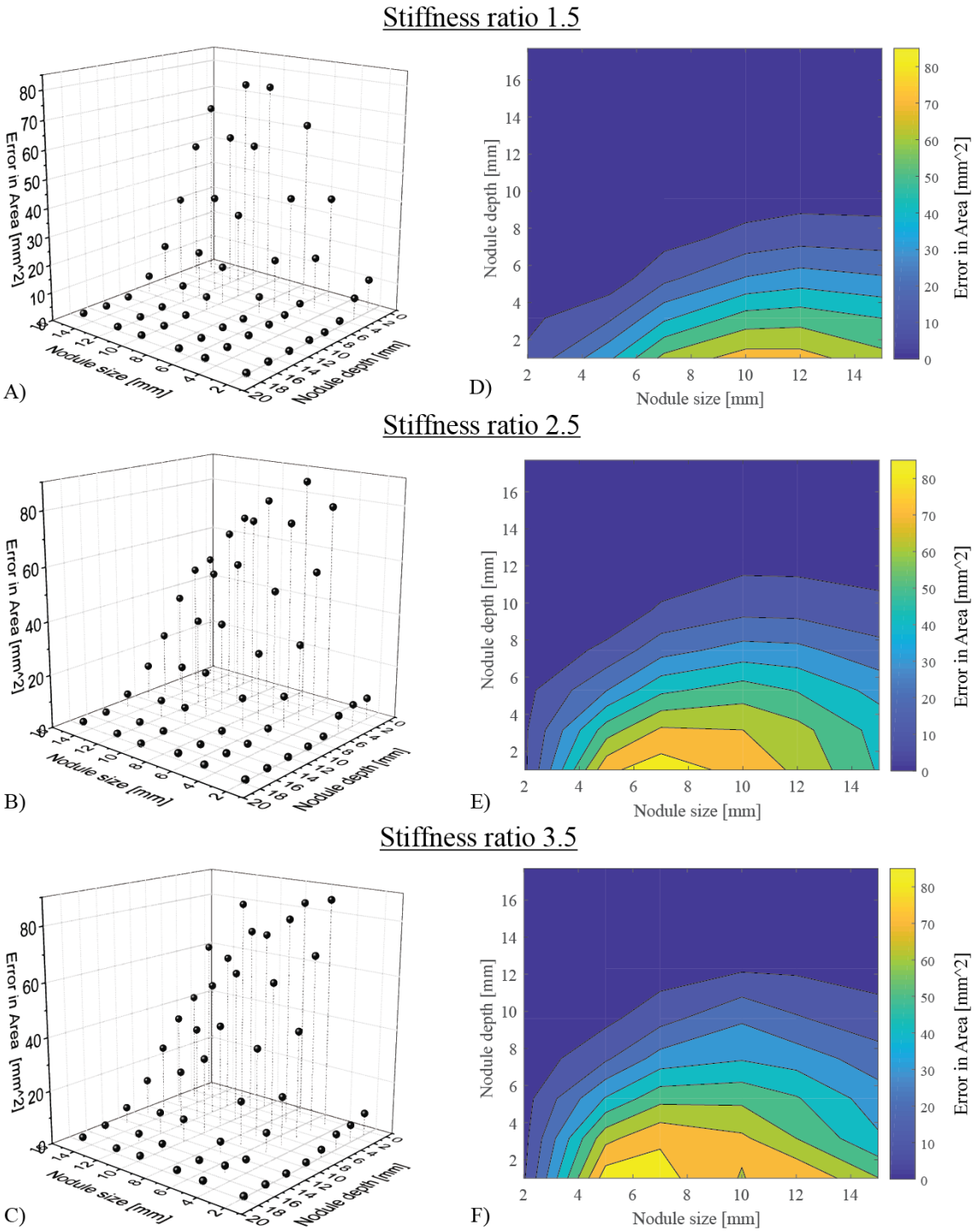

Fig. 4-5. Quantification for the limits of the diagnostic framework in detecting the presence of a tumor nodule in the prostate models. The 3D bar plots (on the left) show the results of the inverse procedure defined as the error in area for 48 combinations of the nodule depth and size with a stiffness ratio of 1.5 (A), 2.5 (B) and 3.5 (C). The 2D contour plots (on the right) show the 'top view' of the results which are illustrated on the left.

4.6 A feasibility study using MRI-reconstructed prostate model

Two FE models reconstructed from MR images were used here, namely Cases B and C, whilst Case A has already been used in Chapter 3. In both cases there was one PCa nodule at present (Fig. 4-6). Similar modelling strategies to those in Chapter 3 were used. Three probing points were used, 15 mm in between. The force values were recorded at probing depths of 4, 5, 6, 7 and 8 mm. The stiffness ratio chose for those examples was 3.5. The high stiffness ratio was chosen for increasing the distortion in the force feedback by the presence of the stiff nodule. As a result, it was possible assessing the sensitivity of the diagnostic framework for detecting a cancerous nodule which shows realistic geometry, depth and position in the prostatic tissue.

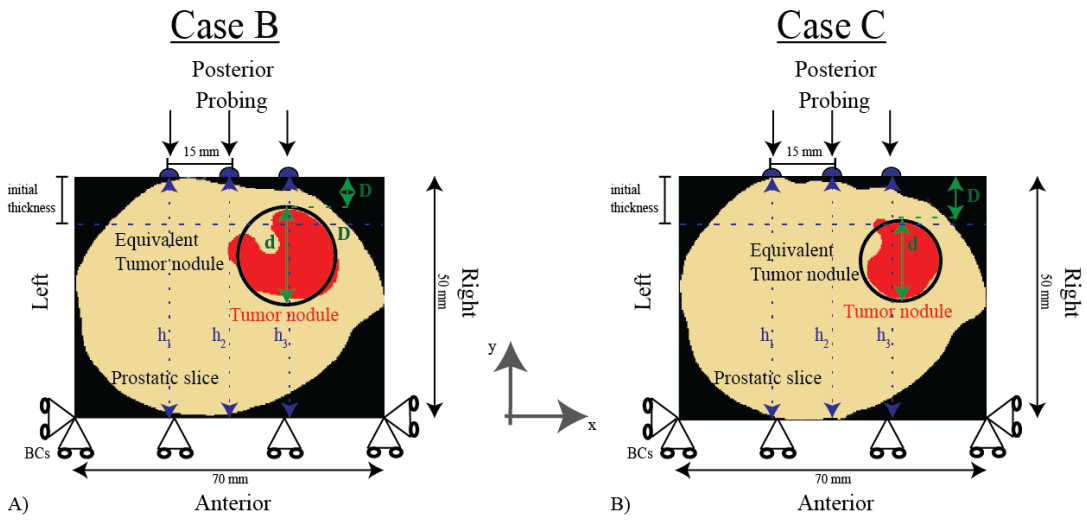

Fig 4-6. Prostate models reconstructed from MR images – Case B and C.

The images were characterized by the presence of a tumor nodule which was located in the posterior surface and right edge of the prostate. The size of the tumor nodule for case B was 368 mm^2 with an equivalent diameter of 10.8 mm and a depth of 4 mm. The location of the PCa nodule for the case C was similar, however, the nodule had a size of

237 mm^2 with an equivalent diameter of 8.7 mm and a depth of 7 mm. The size of the entire prostatic slice was 2455 mm^2, however, it was embedded in a 'box' for simulating the interaction between the prostate and tissues which surrounding it during an *in-vivo* DRE procedure [140]. The size of the 'box' was 3500 mm^2, therefore a tumor area fraction for the case B was 10.5% and 6.8% for the case C. In addition to these two models, a case studied in Chapter 3, i.e. case A, where the PCa nodule was absent in the prostate, was also used here as a comparative study.

Fig. 4-7 shows the results of the errors in estimated area for the 3 cases, plotted against the number of iterations during convergence of the inverse procedure. Once again, the error was significantly higher for the cases where the prostate model contains a PCa nodule (i.e. in case B and C), compared with the healthy case (i.e. in Case A), leading to an under-estimation in areas in cases B and C.

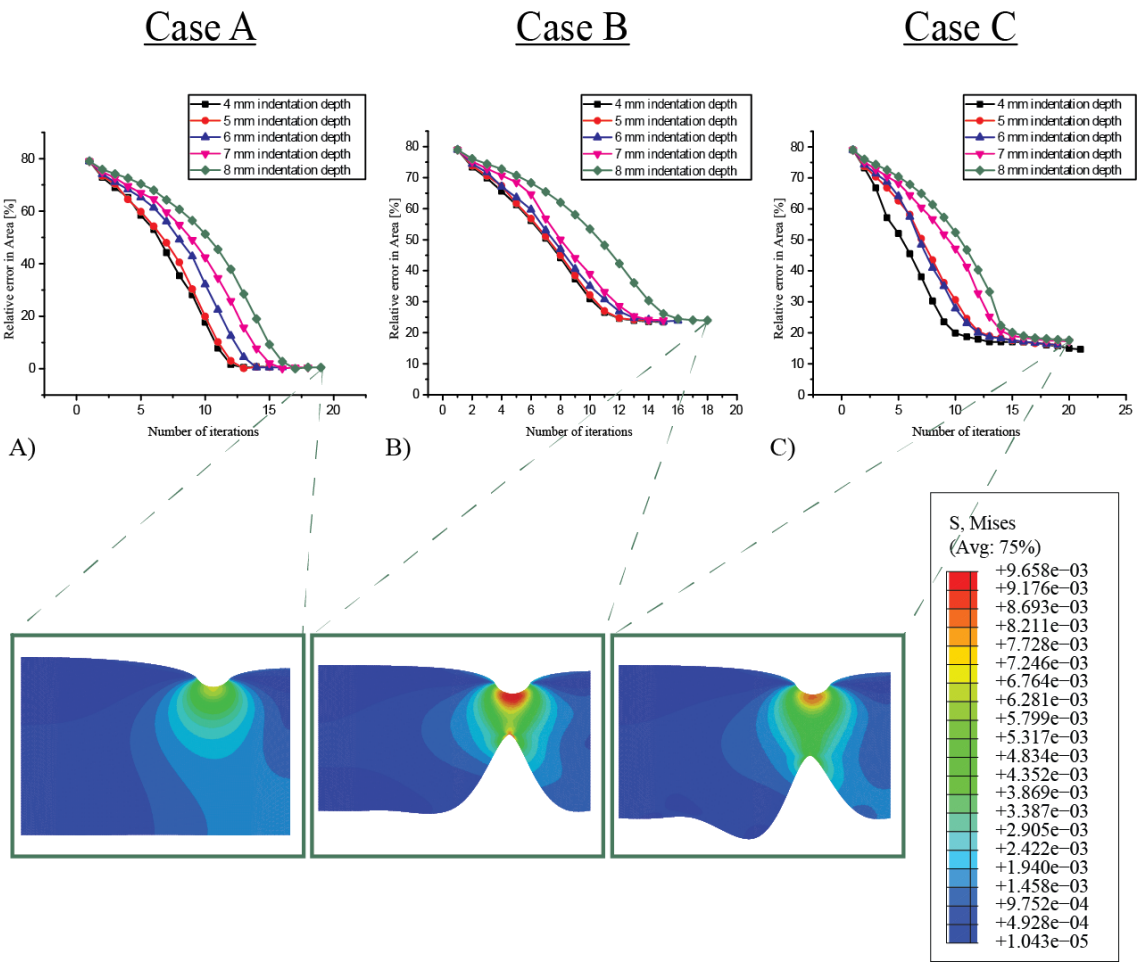

Fig 4-7. Results of the inverse analysis for the prostate models A-C. The values of the stress distribution are in MPa.

Fig. 4-8, similar to what has been presented in chapter 3, demonstrates the identification process of the PCa nodule. The area estimated for case A was similar, within a small margin of error (0.48%), to the true area of the prostate. More importantly, the values remained constant when the probing depth was increased, as already discussed in Chapter 3. However, the estimated areas of the cases B and C were significantly different compared to the 'true value' (24.1% for case B and 17.6% for case C) and the estimated areas also varied when the probing depth increased. However, such variation was as significant as what one would expect (in comparison to Fig. 3-8). This can be attributed to the fact that in Cases B/C the PCa nodule is located rather deeply, leading to a reduced

sensitivity of the predictive method, in comparison to the idealised PCa nodule which located much closer to the posterior surface in Fig. 3-8.

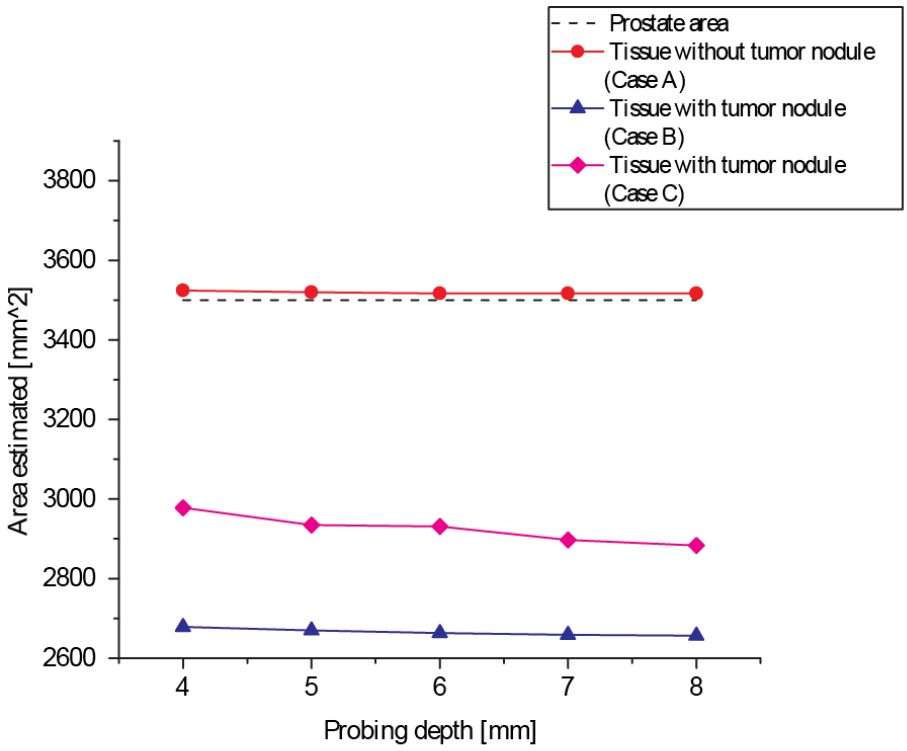

Probing depth	4 mm	5 mm	6 mm	7 mm	8 mm
Case A	3524 mm^2	3520 mm^2	3517 mm^2	3517 mm^2	3517 mm^2
Error	0.68%	0.57%	0.48%	0.48%	**0.48%**
Case B	2679 mm^2	2670 mm^2	2663 mm^2	2659 mm^2	2657 mm^2
Error	23.4%	23.7%	23.9%	24%	**24.1%**
Case C	2978 mm^2	2935 mm^2	2931 mm^2	2897 mm^2	2883 mm^2
Error	14.9%	16.1%	16.2%	17.2%	**17.6%**

Fig. 4-8. Results of the inverse procedure for all three prostate models.

4.7 Concluding remarks

In this chapter, a further sensitivity analysis of the proposed method to nodule parameters, such as size, depth and the stiffness ratio of the PCa nodule. was carried out. The results showed that PCa nodules which are located deeply into the prostate and/or with a small size are challenging to detect. Moreover, the analysis allowed the quantification of the limits in detectability of the proposed framework, dependent upon the interplay between the size and depth of the PCa nodule, and more importantly, to the stiffness ratio between the PCa and healthy tissue. At the end of this chapter, a feasibility study involving three FE models reconstructed from MR images proved the capability of the proposed framework in detecting PCa nodules in a more clinically-relevant scenario.

However, the current framework is only capable of making estimations on the basis of prostate model, not on individual PCa nodules. Therefore, it is not possible to estimate the parameters of individual PCa nodules such as their depth, size and 'dispersion', which are important clinical parameters for assessing the stage and aggressiveness of cancer. Therefore, in the next chapter, a predictive model based on a probabilistic approach will be proposed for characterising individual PCa nodules in the prostate based on point-wise instrumented probing procedure.

Chapter 5

Probability-based Predictive Methods for PCa Nodule Identification

Contents

5.1 Summary

In chapter 3 and 4, a methodology for binary classification of the prostatic tissues with and without the presence of tumor nodule has been presented. The method has the advantage of achieving a classification without a *priori* knowledge of the patients such as the anatomical details and the pathological condition. However, the method is not able to provide the estimation of the nodule parameters such as position, depth, size, essential for clinical diagnosis [141].

Therefore, in this chapter, a novel predictive model which aims to decrease the 'uncertainty' in the soft tissue classification and provide the estimation of the tumor nodule parameters has been developed. The method is based on a probabilistic approach with the aim of decoupling the effect of the nodule size and depth in the probing measurements. Notably, the prediction of the nodule parameters is not deterministic, and the outcome is described by the probability distributions for the size and depth values of the PCa nodule.

The method is hypothesized and later validated using simplified FE prostatic models. A sensitivity analysis is proposed to evaluate the capability of the predictive model using diverse combinations of nodule size and depth. Statistical analysis is carried out for assessing the capability of the proposed method in estimating the nodule position, depth and size. Finally, the complications such as consideration of nodule 'dispersion' are also discussed.

5.2 The simplified prostate model and FE modelling of instrumented probing

The human prostate is surrounded by bladder and rectum in the pelvic cavity, and its posterior surface can be probed through the rectum wall. In this study, prostate is modelled in a simplified way for methodology development. Fig. 5-1 illustrates the simplified prostate model which is represented by a 'square box' of 50 × 50mm. The upper side is the posterior surface, where the probing is carried out. The model is constrained on anterior surface, as shown, to reproduce the experimental conditions.

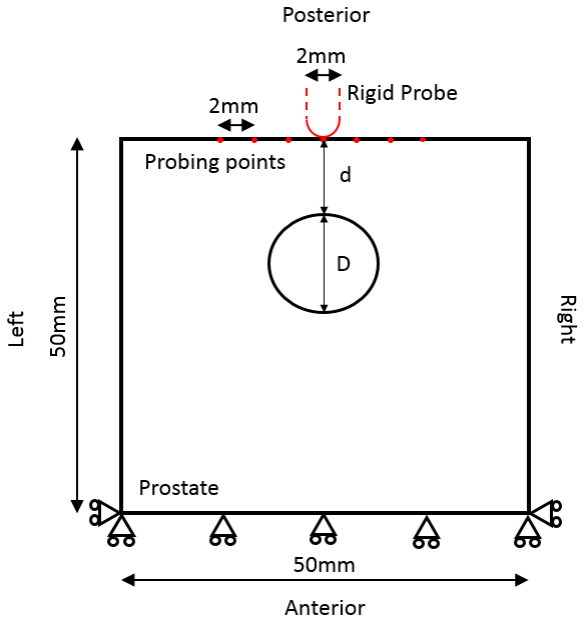

Fig. 5-1. Schematic of a simplified 2D prostate model with a single cancerous nodule embedded, later modelled with Finite Element.

For the sensitivity analysis using the simplified prostate model, the point-wise probing data will be simulated using the FE method. The instrumented probing from the posterior surface was carried out using a rigid semi-spherical probe, which has a diameter of 2mm. This size is chosen to ensure a sufficient spatial 'resolution' of probing along the posterior surface of the prostate. A probing depth of 8mm along the posterior-anterior axis was used at a number of probing points, 2mm apart. The contact with the soft tissue was assumed to be frictionless [106] and the point-wise probing was considered to be quasi-static, using a strain rate lower than $0.01s^{-1}$, allowing the soft tissue to be considered as a hyperelastic material without its viscous component [142]. To allow for the high local strain that may occur in FE simulations, a neo-Hookean hyperelastic model was used for both cancerous and non-cancerous tissue. The strain energy function of the model is expressed as

$$U = C_1(\bar{I}_1 - 3) + \frac{1}{D_1}(J-1)^2 \quad (5\text{-}1)$$

$$D_1 = \frac{2}{K_0} = \frac{3(1-2\nu)}{\mu_0(1+V)} \quad and \quad \mu_0 = 2C_1 \quad (5\text{-}2)$$

where $\bar{I}_1$ is the first deviatoric strain invariants and J the total volume ratio (refer to Chapter 2 section 2.3.2). The remaining material parameters, C_1 D_1, are related to bulk modulus (K_0), initial shear modulus (μ_0) and Poisson's ratio (ν), as shown in Eq. (5-2). The prostate tissue was modeled as aa nearly incompressible material [136]. The elastic properties of prostate tissue were adopted from the work by Hoyt et al. [65], who measured the Young's moduli of the non-cancerous and cancerous tissues from *ex vivo* radical prostatectomy samples as 17kPa and 42.5kPa, respectively. The Poisson's ratio of both tissue types is considered to be 0.49 [143]. As a result, after fitting the neo-Hookean model in Eq. (5-1) against the elastic properties mentioned above, the non-cancerous tissue had properties of C_1 (0.00285 [MPa]) and D_1 (7.067 [-]) and the cancerous tissue of C_1 (0.00712 [MPa]) and D_1 (2.827 [-]). The FE models (both simplified and those reconstructed from the histological sections) were meshed with four-node bilinear plane stress quadrilateral elements (mesh refinement was conducted to ensure cost-effective convergence of FE simulations) and solved in ABAQUS (Dassault Systemes, Vlizy Villacoublay, France). The reaction force exerted on the rigid probe by the examined prostate model at the given depth is then recorded at each probing point and its profile over all probing points is further investigated.

5.3 A probabilistic approach for identification of cancerous nodules

When the prostate is examined by point-wise probing as mentioned above, the reaction force is recorded at each point at a predefined indentation depth, forming a force profile along the posterior surface of the prostate. Such a force profile, as illustrated in Fig. 5-2,

has rather unique characteristics of local peaks, heavily influenced by the inhomogeneity in the prostate (i.e. the presence of a stiff cancerous nodule) [118]. Furthermore, a peak in the force profile is sensitive to the size and depth of the cancerous nodule and it becomes ‘sharper’, i.e. taller and narrower, when the nodule is located near the posterior surface and/or is larger. Therefore, the sharpness of the peak, represented by the ratio between its height and width, i.e. H/W, is a unique characteristic of the peak, related to the size and depth of the cancerous nodules, which give rise to inhomogeneity in the prostate and consequently a peak in the force profile. However, both size and depth of the cancerous nodule could influence the peak force in the measured profile in a similar way – a larger and deeper nodule may lead to a similar force profile to the one caused by a smaller but shallower nodule. Such non-uniqueness means it may not be possible to give a definitive prediction based on the force profile from quasi-static probing, and a probabilistic approach is needed to decouple the effects of the size and depth of the cancerous nodule from the peak.

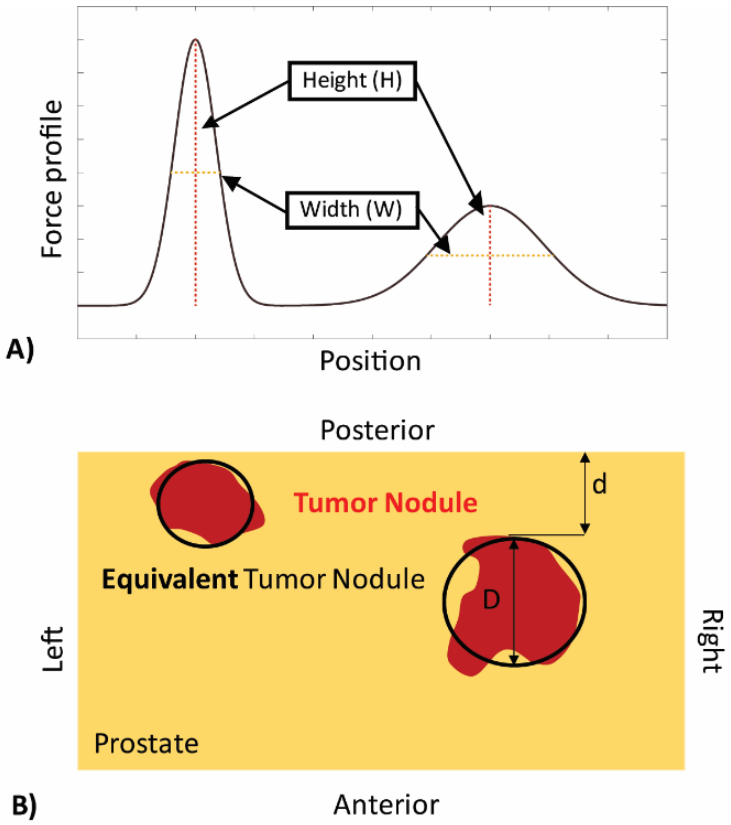

Fig. 5-2. An example of force profile. A) Two peaks can be identified, each having unique height and width characteristics; and B) the corresponding prostate model, in which the red areas denote the cancerous nodules and the black outlines indicate the predicted nodules.

As discussed above, an infinite number of combinations of nodule size and depth exist that may lead to the same force profile, due to the coupling effect between these two factors. The method proposed here, therefore, aims to estimate the possible ranges of the size and depth of the tumor nodule, due to the stochastic nature, rather than making a definitive prediction. To achieve this, a probabilistic approach is adopted, where the peak profile is 'searched' among a pool of a large number of random models, in which the size (between 2mm and 24mm in diameter) and depth (between 2mm and 30mm) of single cancerous nodules are randomly chosen. Such ranges are chosen in accordance to the common characteristics of cancerous nodules in prostate. As a result, a total number of 2500 of random models are generated, each having a unique tumor nodule and a peak in

the force profile, which is then characterised by its height, H, and width, W. The stiffness ratio in the random models was 2.5. However, the analysis in Chapter 4 showed that the stiffness ratio influences the peak in the reaction force profile and consequently the ratio H/W. Nevertheless, the identification of patterns for the system prostate-nodule using the combinations of the 3 parameters would be challenge and time-consuming.

The random models were generated using the following steps: firstly, random values, within the prostate domain, were assigned as coordinates of the nodule centre. Secondly, a random value, within the range of the nodule size values, was assigned as the diameter of the cancerous nodule. However, the choice of the centre might restrict the range of the values for the nodule diameter as its boundaries were constrained of being within the prostate domain. The MATLAB function *rand*[7] was used to choose the random values for the coordinates of the nodule centre and the nodule diameter.

Fig. 5-4 shows a clear trend of positive correlation between the 'sharpness' of the peak, i.e. H/W, and the 'degree of influence' in the peak profile caused by the cancerous nodule, i.e. d/D. A positive correlation between the two sets of parameters can be observed, meaning that the larger and shallower the nodule is, the sharper the peak becomes. More interestingly, the span of the random models in the plot, which is a measure of the 'uncertainty' in the correlation between these two sets of parameters, increases significantly when the peak in the force profile become 'sharper'. For flatter peaks, i.e. data points with smaller H/W values along the x-axis, almost all cancerous nodules are located deeply in the prostate (i.e. greater value of D), regardless of their sizes. Therefore, all data points for flat peaks are distributed very closely with little dispersion in the plot. However, when the peak becomes more predominant, i.e. an increasing H/W value, either

[7] https://uk.mathworks.com/help/matlab/ref/rand.html

small nodules with a very shallow depth, or larger nodules with a small depth could lead to sharp peaks, leading to higher dispersion of the data points along the y axis.

Nevertheless, the trend in Fig. 5-4 illustrates that the sharpness of the peak in force profile can be correlated to the size-to-depth ratio of the tumor nodule, albeit having a certain degree of 'uncertainty'. Therefore, it is hypothesized here that, for a peak with a given sharpness value (on the x-axis in Fig. 5-4), the size-to-depth ratio of its tumor nodule would fall into the range (along the y-axis) depicted by the random models. To implement this, one needs to divide the dataset of the random models in Fig. 5-4 into sub-groups according to the 'sharpness' of the peak, as shown by the vertical dashed lines. A total number of 2500 of random models (hereafter referred to as 'the training dataset'), are divided into 6 groups according to the 'sharpness' value (i.e. H/W) of their peaks, namely, 5-10 (465 cases), 10-20 (325cases), 20-30 (177 cases), 30-40 (128 cases), 40-50 (126 cases), higher than 50 (104 cases).

Importantly, Fig. 5-4 did not include 1175 cases where the H/W is less than 5. We proposed this value as a 'threshold' for the nodule identification process, below which the peak is believed to be unidentifiable. This is illustrated in Fig. 5-3 where the reaction force profile is obtained by probing a soft tissue model without a tumor nodule. The homogeneity of the soft tissue caused a rather flat force profile with a H/W as low as 3. Considering the experimental measurements could be affected by certain degrees of noise, the threshold was set to be 5.

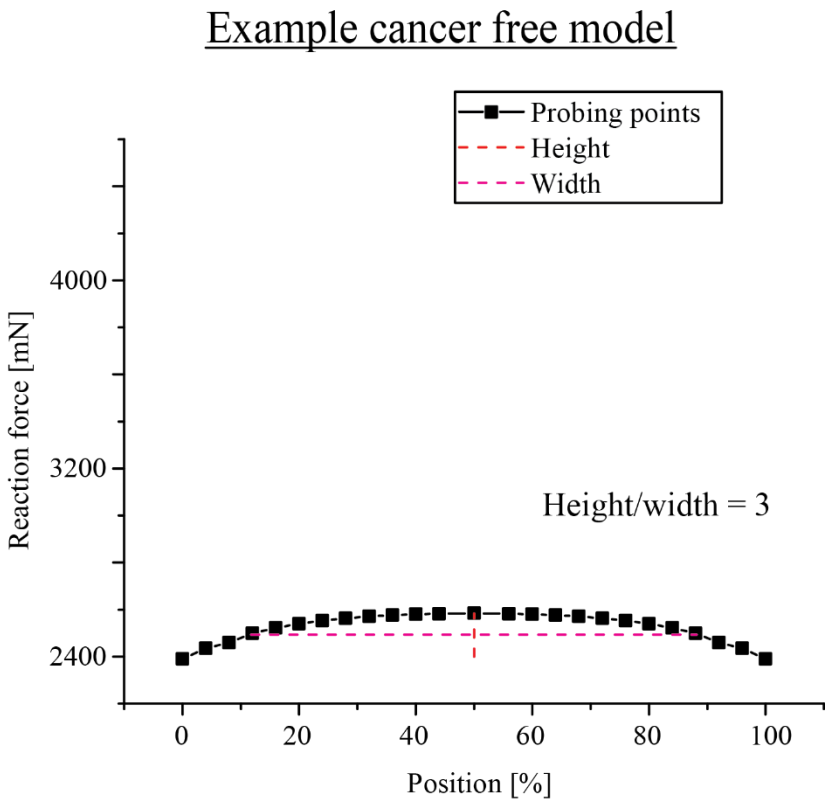

Fig. 5-3. Example of reaction force profile obtained by probing the soft tissue model which does not show the presence of a stiff nodule. The flat profile is characterized by a small height and large width.

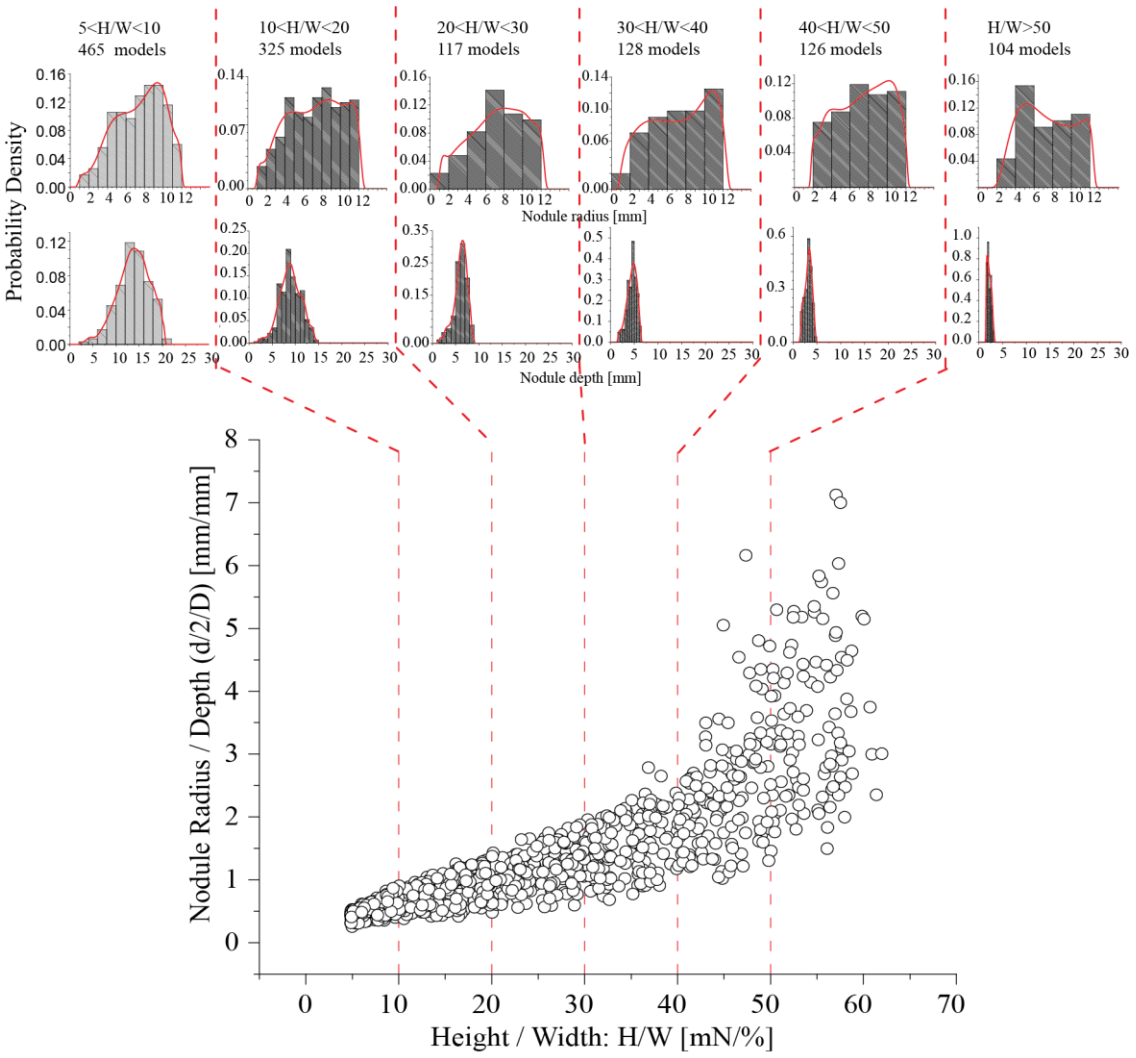

Fig. 5-4. Correlation between the peak sharpness (H/W) and the nodule radius/depth (d/D), of all random models (excluding those with unidentifiable peaks with H/W<5). Using the peak sharpness, H/W, the entire dataset is divided into 6 groups, each having characteristic probability distribution of their nodule size and depth. All these characteristic probability distributions will be employed to predict the tumor nodule existence, using the methodology included in the appendix A.

As shown, each data group contains enough numbers of representative random models, from which the probability-based prediction can be made. Each group, divided by different degrees of sharpness in their peak profile, also has characteristic distributions in the size and the depth of their tumor nodule, as illustrated by the histograms in Fig. 5-4. Certain variations of the probability distributions in both the size and depth of the cancerous nodule with respect to the increasing peak sharpness (H/W) can be observed.

Most importantly, the nodule depth is found to be significantly influenced by the peak sharpness. When the peak sharpness becomes greater, the probability distribution of the nodule depth becomes more concentrated towards smaller values, i.e. shallower nodules. This shows the peak identified in the force profile is highly sensitive to the nodule depth, but much less so to the nodule size. This can also be observed in Fig. 5-5, where nodules of all 2500 cases that have been generated by the random algorithm are plotted with their depth (d) against size (D). All cases are stratified according to their 'zones' of peak sharpness, and the greater the sharpness, the less 'uncertainty' their depth distributions present.

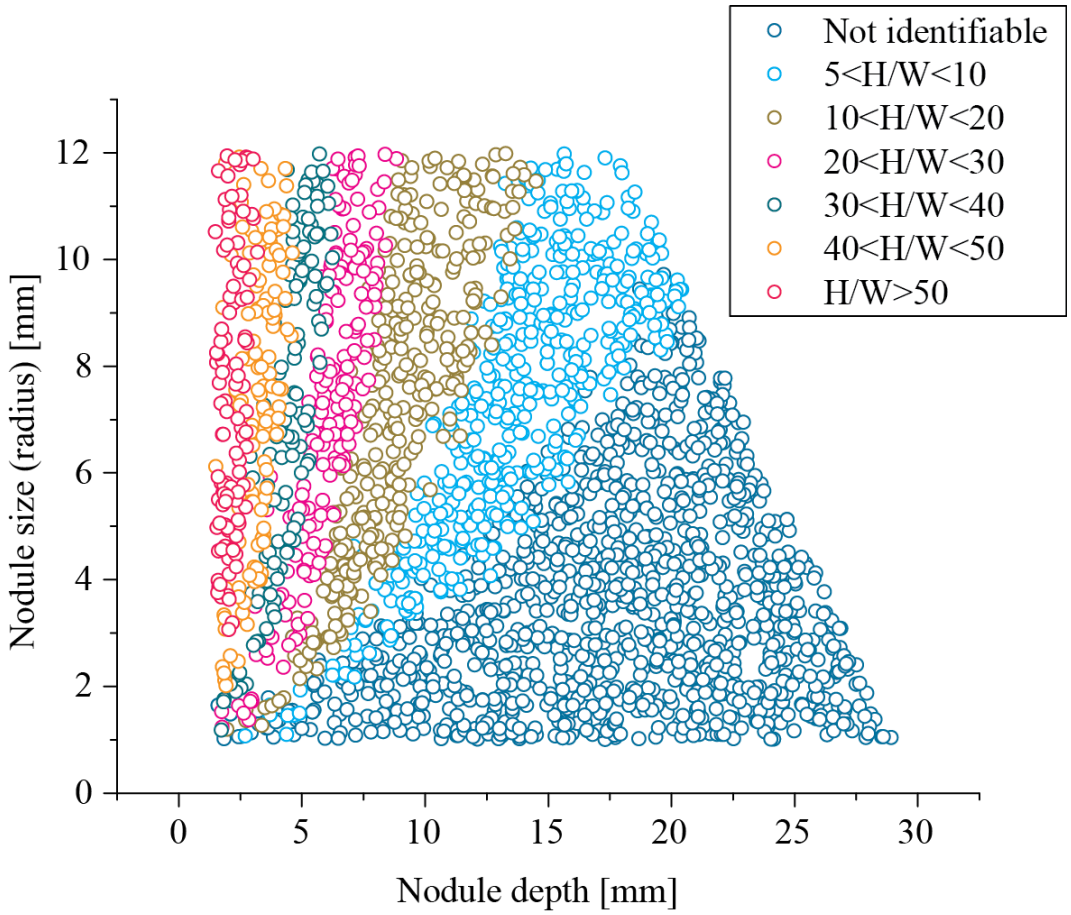

Fig. 5-5. The relationship between the nodule depth and size, where the sharpness of force peak in each division is plotted with different colours.

Due to the characteristic probability distributions of the nodule size and depth with respect to their peak sharpness, it is proposed here that, based on the sharpness of an identified peak in the force profile, one can make prediction of the presence of the cancerous nodule in the prostate 'domain' on a probability basis, and the methods will be detailed in Appendix A.

5.4 Probabilistic Approach - Sensitivity analysis with simplified prostate models

To demonstrate the probabilistic approach in tumor nodule identification, simplified prostate models, as illustrated in Fig. 5-1, are used here first. All the force profiles of instrumented probing are derived from the simplified prostate models using FE approach, as detailed in the methodology. Here, two representative cases are presented, both having nodules of similar diameter (D1=22.8mm; D2=20.6mm) but with different depths (d1=1.5mm; d2=13mm). In both cases, the peak in the force profile is identified and characterized by its height and width, as shown in Figs. 5-6 (A) and (D). The ratio between its height, H, and width, W, i.e. the sharpness of the peak, is used to predict the probability distribution of the nodule existence using the proposed methods, where the nodule is represented by the solid red circle and the predicted probability is illustrated along both axes. It should be noted that, the probability distributions are not the PDFs showed in Fig. 5-3, however, the results of the prediction described in Appendix A. Each value of the probability indicates the likelihood of that point being cancerous. It can be seen that, since the nodule is located more deeply in the second case, its peak value is much lower and force profile is less sharp (H/W=12, in comparison with the H/W=56.2 in the first case). This has also led to two distinct predicted probability for two cases, as shown in Figs. 5-6 (C-F). Interestingly, for a shallow nodule in case 1, the predicted probability map has a large area that has probability close to '1' near the centre of the

nodule. Although the prediction also correctly captured the nodule location for case 2, it has a much smaller area with probability close to ‘1’, indicating a lower degree of certainty in such prediction. This, again, reflects on the effects of the nodule depth on the ‘uncertainty’ as aforementioned in Fig. 5-4.

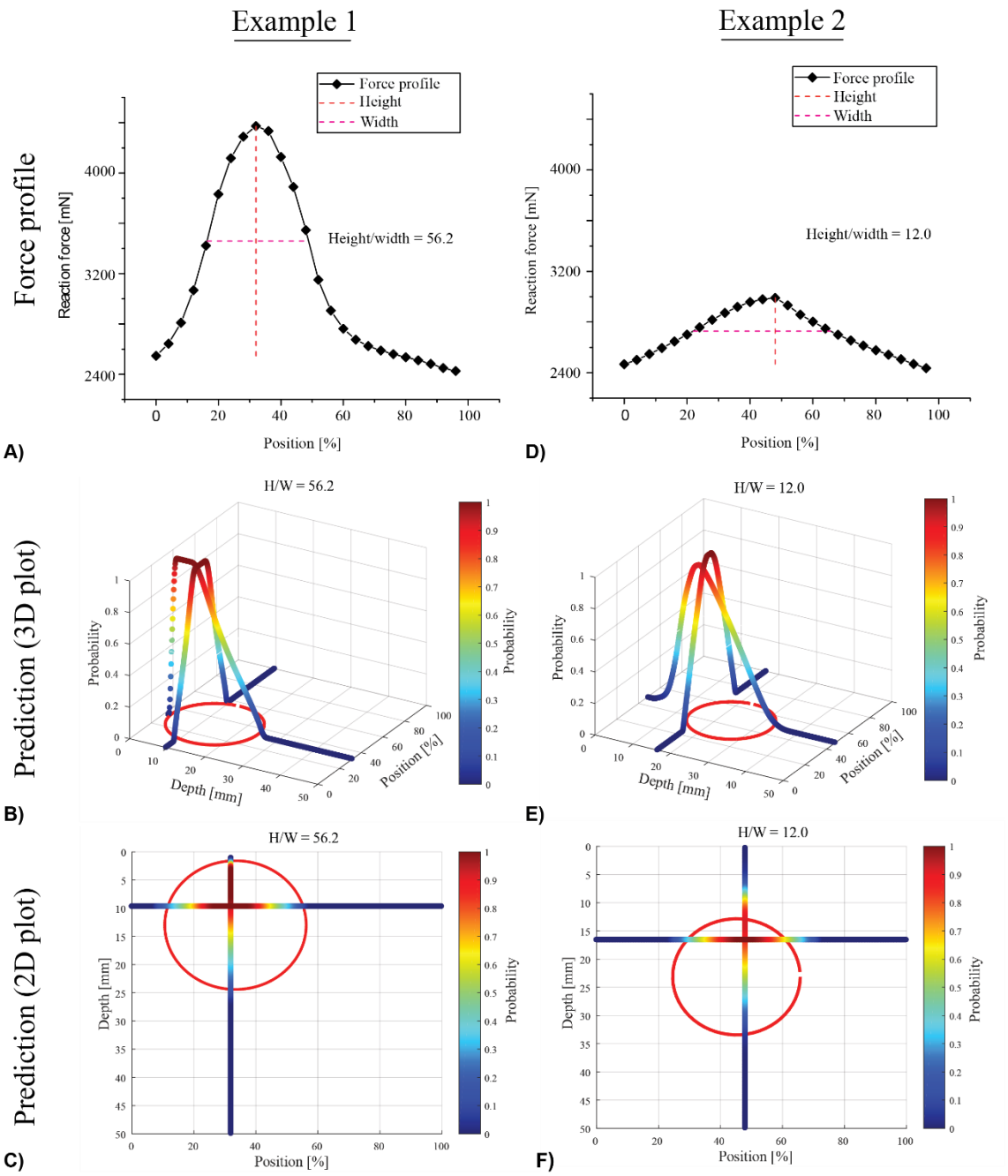

Fig. 5-6. Two examples of simplified prostate models, including the force profile and the predictions in 3D and 2D with illustrated probabilities (which are not the PDFs showed in Fig. 5-3). A-D) Force profile and peak identification for a prostate model which shows a cancerous nodule near the indented surface (A) and deeper in the prostate domain (D). B-E) Probabilities of the nodule existence along the posterior-anterior and left-right axes of the prostate model. C-F) 2D prediction of the nodule identified on the plan depth and position of the prostate model.

Although the results presented above demonstrated that the proposed method is capable of predicting the probability of nodule existence along two main axes of the prostate, it would be useful to have a 'binary' prediction of the nodule region, for which a threshold in the probability needs to be chosen. Such a threshold can be interpreted in Figs. 5-6 (B-E) as a 'horizontal plane' cutting through the 'bell-shaped' probability plot, and the area with probability greater (i.e. higher) than the plane would be the predicted nodule region. The effect of the chosen probability threshold on the predicted tumor area is demonstrated in Fig. 5-7, where the same examples as in Fig. 5-6 are used. In both examples, the probability threshold is found to be critical to the predicted tumor area in a binary fashion, and a greater threshold would lead to a smaller nodule predicted. Choosing the optimal value for the probability threshold is not a trivial task – choosing a smaller value would lead to a larger nodule predicted, more likely to cover the 'true' tumor nodule, however, this could also lead to over-prediction; in contrary, choosing a greater value would have an opposite effect.

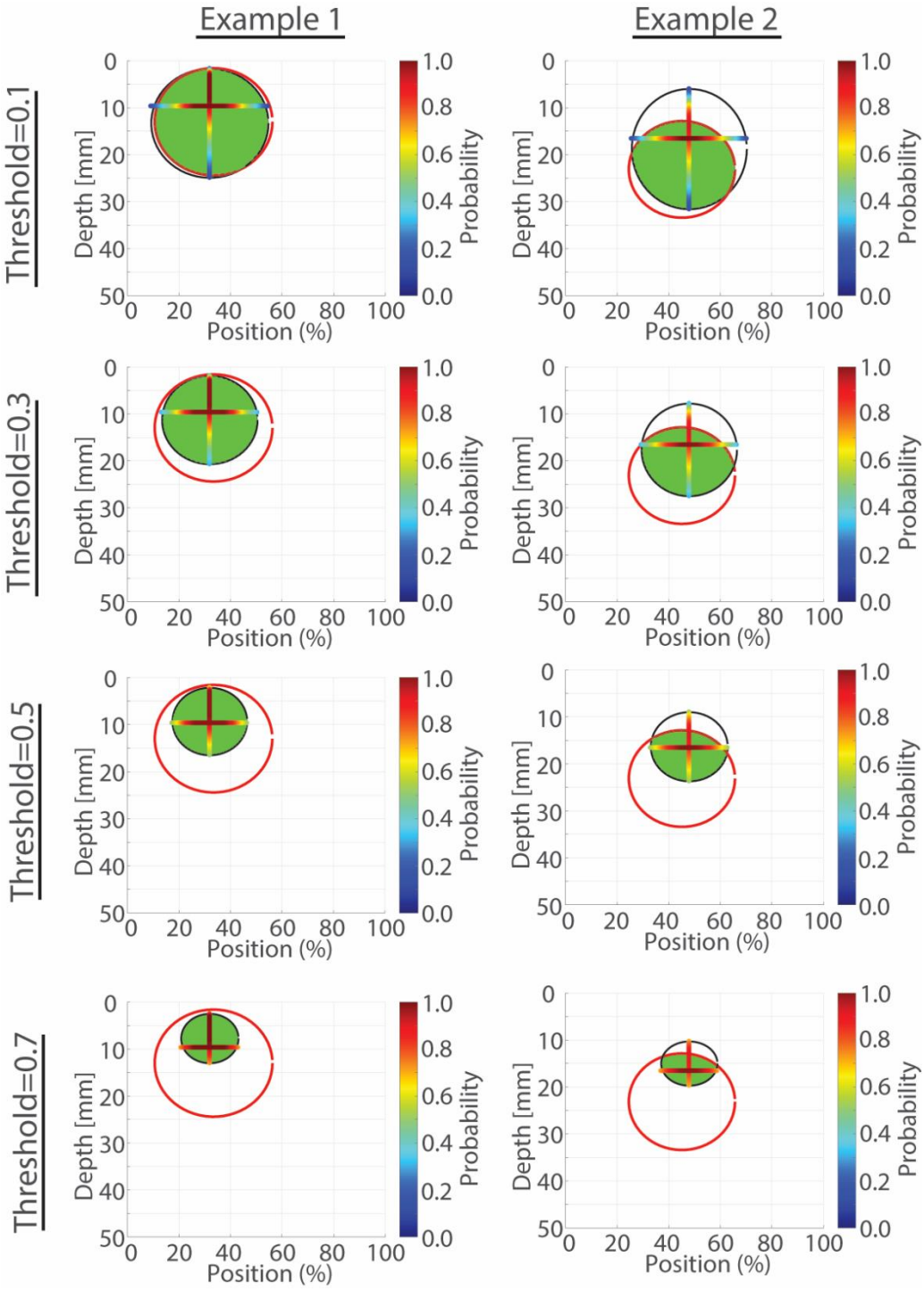

Fig. 5-7. The 'binary' tumor areas predicted from choosing a threshold in the probability of tumor existence. The same two examples as in Fig. 5-6 are used here again, with four different probability thresholds applied. The black and red outlines represent the predicted and the PCa nodule, respectively.

5.5 Probabilistic Approach - Statistical analysis of prediction

To examine the performance of the proposed method, sub-groups consisting of 400 models were randomly chosen (using the MATLAB function *rand*), for 4 times, from the original 2500 random prostate models. All randomly chosen models then went through the proposed method and the predicted tumor nodules were checked with the 'true' nodules in those prostate models. Results (which will be discussed in Section 5.6) showed that 4 randomly chosen sub-groups have consistent behaviour, in line with the entire dataset as illustrated in Fig. 5-4. Furthermore, to assess the effectiveness of the proposed method, three indices are used here, as

$$\text{Index}_1 = E_d\left(C_{p,}\, C_{TN}\right) / (D/2) \tag{5-3}$$

$$\text{Index}_2 = A_{Tp} / TN_{Area} \tag{5-4}$$

$$\text{Index}_3 = \frac{PN_{Area} - A_{Tp}}{PN_{Area}} \tag{5-5}$$

where E_d is the distance between $C_{p,}$, the centre of the predicted nodule, and C_{TN}, the centre of the PCa nodule. D denotes the diameter of the PCa nodule. A_{Tp} denotes the overlap area between PN_{Area}, the area of predicted nodule, and TN_{Area}, the area of PCa nodule. As a result, Index_1 represents the accuracy of the predicted centre of the tumor nodule. The lower the Index_1 is, the more accurate the predicted location is. Index_2, on the other hand, represents the 'true positive', i.e. the correctly identified nodule area, in relation to the total nodule area, whilst Index_3 represents the 'false positive', i.e. the incorrectly identified healthy area, in relation to the total predicted area. Index_1 is independent of the chosen probability threshold, since the centre of the predicted nodule is not affected by it. However, both Index_2 and Index_3 could be affected by the probability threshold therefore their sensitivity will be analysed here.

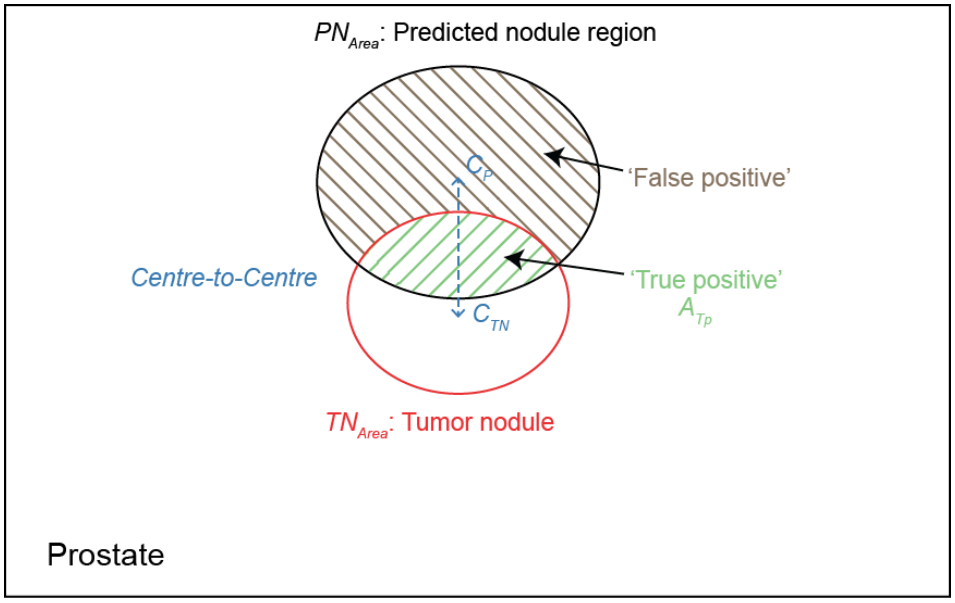

Fig. 5-8. Illustration of the predicted model performance in the tumor nodule parameters estimation such as position, depth and size.

Statistical analysis of results for one randomly chosen sub-group (400 models) is presented here in Fig. 5-9. Firstly, for the $Index_1$ (Fig. 5-9 (A)), the majority of predicted nodules has their centres within the true tumor nodule ($Index_1<1$). More interestingly, its accuracy depends highly on the size of the nodule. For almost all tumor nodules in a diameter greater than 10mm, the predicted centre is correctly located within the tumor nodule, whilst for smaller nodules the accuracy of the prediction centre is considerably worse. It is also worth noting that there are a few outliers with $Index_1$ greater than 4, due to the small nodules (<5mm in diameter) present in those cases. Secondly, for the $Index_2$ (Fig. 5-9 (B)), the probability threshold is shown to have significant impact, since a greater threshold would result in a smaller predicted tumor area, leading to worsened 'true positive'. Finally, similar behaviour can be seen for the $Index_3$ (Fig. 5-9 (C)), however leading to an improved 'false positive'. Therefore, one needs to choose the probability threshold carefully in order to balance between the 'true positive' and 'false positive'. For all the following results, a probability threshold of 0.5 will be adopted.

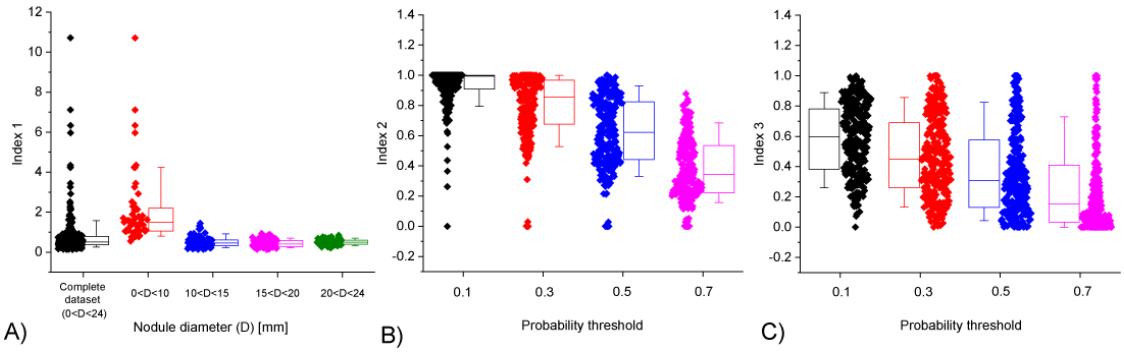

Fig. 5-9. Statistical analysis of one randomly chosen sub-group (400 models) using three different indices. Box indicates 25/75 percentiles and whiskers 10/90 percentiles.

5.6 Probabilistic Approach - Complications and Detectability limits

There are several complications that need to be discussed here. Firstly, the force profile may contain more than one peak along the left-right axis, indicating the existence of more than one detectable cancerous nodule in prostate. Two representative examples are shown in Figs. 5-10 (B-D), one where the force profile contains two identifiable peaks given rise by two separate nodules (Fig. 5-10 (C)), and the other one where the force profile only contains one single peak but given rise by two adjacent nodules (Fig. 5-10 (A)). It is evident that when two nodules are located far away from each other along the left-right axis, two separate nodules can be predicted given rise by two distinct peaks. However, when two nodules are too close to each other, only one peak can be identified in the force profile, leading to prediction of a single tumor nodule. Secondly, cancerous nodules may also have spatial dispersion along the anterior-posterior axis (i.e. along the vertical direction in Fig. 5-1), hence the influence of nodules located deeply in the force profile may be 'shielded' by those shallow ones. Such effect is illustrated in Figs. 5-10 (E-F), where one smaller nodule is located on top of the other larger one. In this case, although the horizontal location is correctly predicted because of a single peak, the prediction is in fact affected by both nodules and the shallower nodule could somewhat shield the deeper

one, resulting in under-prediction over the deeper nodule. Nevertheless, the proposed method is still capable of predicting the nodules in all three examples, with a good level of accuracy as indicated by the probability map.

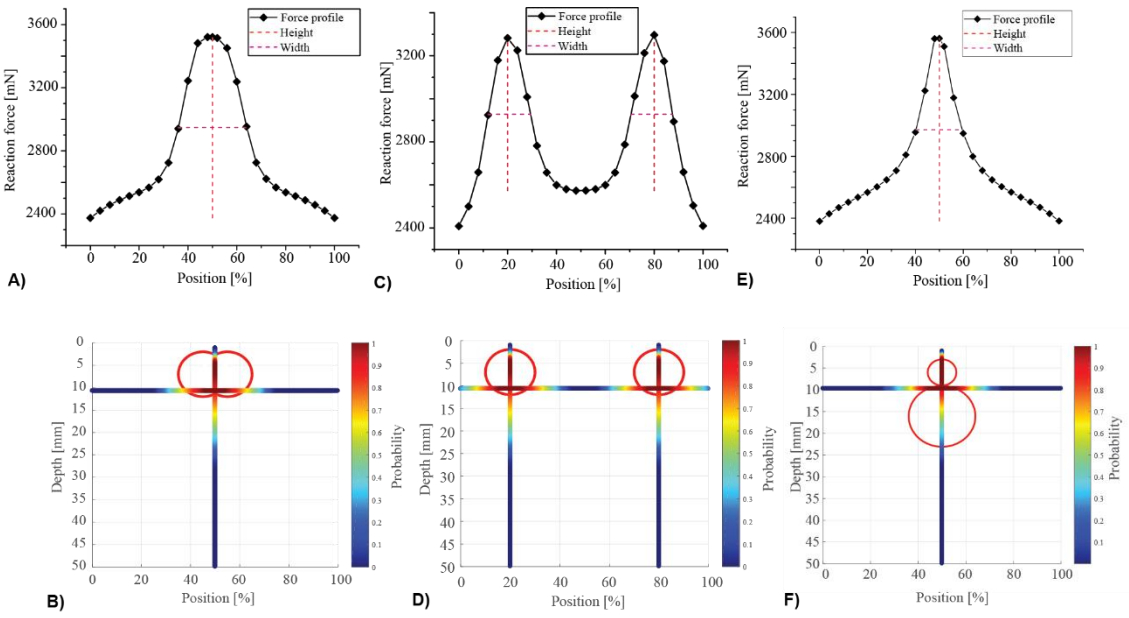

Fig. 5-10. Three representative examples, demonstrating the effects of the nodule dispersion along the left-right and anterior-posterior axes on the predicted results, respectively. The top of the figure shows the force profiles and peak(s) identification for a case of two adjacent cancerous nodules (A), a second case where the nodules are located far away from each other along the left-right axis (C) and a case where one smaller nodule is located on top of the other larger one (E). The bottom of the figure shows the prediction of the nodule(s) existence into the prostate domain for the three cases.

Among all 2500 cases studied here, some cancerous nodules were not detected using the proposed methods, due to the force profile with a sharpness less than 5 not accepted as a peak. Due to the 'coupling effects' between the size and depth of a cancerous nodule on the force peak that it may cause, the detected and non-detected cases, for 4 subgroups, are plotted in Fig. 5-11 against these two nodule parameters. Interestingly, while both parameters show certain influences on the detectability of the cancerous nodule, there is

clear distinction between detected and non-detected cases. The nodules which show a radius higher than 8mm are detectable. However, if the nodules are located near the surface, there are highly chances of detection even for small nodules. More importantly, it is evident that all nodules located more deeply than 20mm from the probed posterior surface are not detectable regardless their sizes. The uncertainty in the classification increase in the zone where the nodules show radius less than 8 mm and depth between 7.5 and17.5mm. It is evident an overlapping for the detected not-detected cases which is caused by the interplay between the nodule size and depth in the reaction force values obtained by probing the soft tissue.

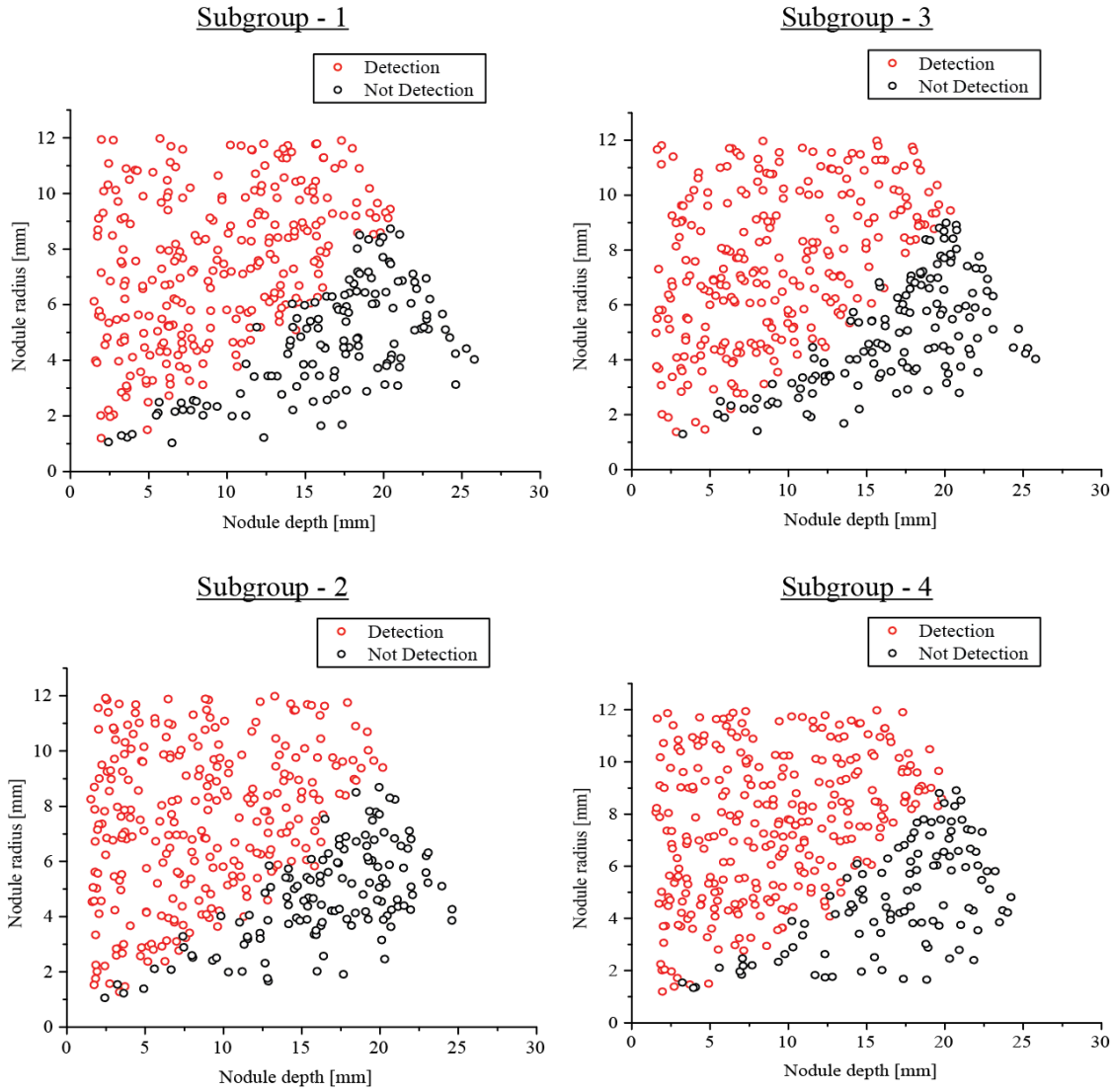

Fig. 5-11. Combinations of nodule size and depth (for 4 subgroups of the dataset) which cause a peak in the reaction force profile with ratio H/W less than 5 (not detection of the inclusion) and ratio higher than 5 which is the detection threshold for classifying prostatic tissue slices and then be able to apply the predictive model to characterize the PCa nodule parameters.

5.7 Concluding remarks

In this chapter, a novel predictive model based on a probabilistic approach was developed. The predictive model provides a classification between soft tissues with and without the inclusion of stiff nodules and the estimation of the nodule parameters such as their position, depth and size. The predictive model was first presented using simplified FE

prostate models. To demonstrate the capability of the method in nodule identification two examples were presented. A prostate model with a nodule near the posterior surface and another case where the nodule had a similar size but was located more deeply. Therefore, the peaks showed diverse characteristics and sharpness values. The results showed how the predictions correctly captured the nodule location for both cases. However, the depth of the PCa nodule clearly demonstrated an important role in influencing the predictions from the proposed methods.

A probability threshold was proposed for the binary identification of the cancerous regions in the prostate domain. The results for a threshold of 0.1 showed a good level of accuracy in the tumor area identification, however, the method may overestimate the nodule size. In contrast, for a threshold of 0.7, the accuracy in the tumor nodule identification decreases and the prediction of non-cancerous area improves. Therefore, the threshold can be seen to have a 'two-way effect', and it is possible to find a value for it in order to yield optimal clinical outcome.

The threshold might be optimized by exploiting the magnitude H. A higher magnitude is a sign of a cancerous nodule located in the posterior surface with a larger size. Therefore, further studies are needed to find out a robust correlation between the size of the cancerous nodules and the magnitude H. Ideally, for a higher H/W and H the threshold should decrease with the purpose of increasing the area of the predicted nodule.

The threshold could be chosen based on the prediction of the nodule depth. If the prediction suggested the presence of a cancerous nodule located within 12mm from the posterior surface, the probabilities of a nodule with a size lower than 5mm are low as shown in Fig. 5-11. Therefore, in this case, the threshold should be chosen towards smaller values to increase the area of the predicted nodule.

The optimal threshold might be determined by combining the results of the predictive model with medical imaging such as MRI and Ultrasound. For instance, a region of interest can be identified using the medical imaging and based on that identify the threshold of the prediction which minimizes the uncertainties in the cancerous nodule detection as a combination of the outcomes obtained by both diagnostic techniques [144].

In the final section, two cases of method complications were investigated, including one case where two PCs nodules area 'overlapping' along the left-right axis and another one where one nodule is 'on top of' the other one. Results demonstrated a certain level of errors in the predictions and this will be further investigated in the following chapter using realistic models reconstructed from histological images. Furthermore, the method showed a limitation in identifying tumor nodules which are located deeply into the prostate domain. The detectability is heavily influenced by the nodule depth, particularly for those with a small radius between 2 and 8 mm. Moreover, the results showed that a nodule with a depth higher than 20 mm from the posterior surface is undetectable.

In conclusion, the proposed predictive model showed promising potential in identifying the existence of tumor nodules in prostate, based on the instrumented probing data obtained from FE simulations using simplified prostate models, and more importantly, was capable of predicting, on a probability basis, the location, size and depth of PCa nodules. There are certain limitations, particularly for those PCa nodules that are small, located far from the posterior (probing) surface and have a high degree of dispersion. Therefore, in the next chapter, the predictive model will be assessed using a large dataset of models reconstructed from histological images for further study.

Chapter 6

Validation of Predictive Methods – Stage 1: Models Reconstructed from Histological Images and FE-Simulated Instrumented Probing

Contents

6.1 Summary

In chapter 5 the predictive model was developed and assessed using simplified prostate models and PCa nodules. To further assess the effectiveness of this model, in this chapter, a dataset of models reconstructed from the histological image will be used. The reaction

force profile will be obtained from simulating the palpation procedure using FE method. The capability of the proposed methodology will be assessed at the patient, tissue and nodule levels, respectively. Furthermore, the detectability limitation as a function of the nodule depth and size will be estimated. Finally, statistical analysis regarding the accuracy in predicting the PCa nodule position, depth and suspicious area will be presented.

6.2 The prostate models - histology and simplifications

Based on the histology images, FE models were reconstructed, based on the outlines of the prostate and tumor nodules. The mechanical probing was carried out on the upper side of the model, which is the posterior surface of the prostate (Fig. 6-1). For the boundary conditions, the work produced by Mousavi et al. [140] has been taken as reference. Mousavi et al. suggested a prostate model reconstructed using elastography images. The prostate model was surrounded by a homogenous soft tissue which was constrained due to the presence of the pubic bone. The thickness of the surrounding tissue was 1.5 times greater than the prostate so that the force values were not influenced by the rigid constraints as the stress decreases rapidly with the distance from the probing points. Therefore, the prostatic slices were embedded in a 'box' of fascia (Fig. 6-1). Moreover, the fascia tissue was extended of 15 mm in both directions of the model in order to mimic the mechanical 'interaction' with the tissues surrounding the prostate *in-vivo*. The model is constrained on the left and right edges and at the anterior surface, as illustrated in Fig. 6-1. The constraints allow zero displacement conditions.

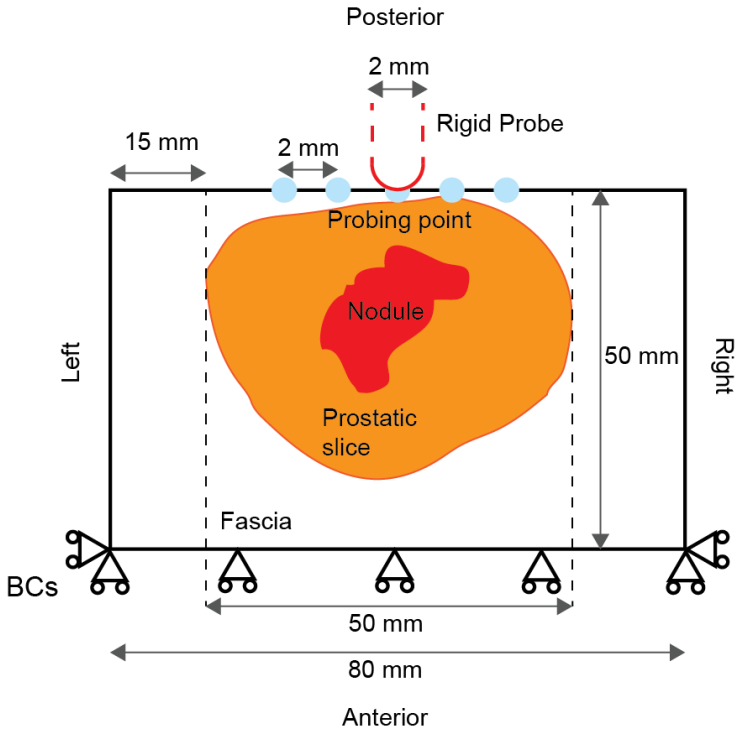

Fig. 6-1. Schematic of the histology-based model.

The instrumented probing was performed using FE method at 25 points on the posterior surface and the reaction force was recorded at the indentation depth of 9mm. The distance of 2mm between the probing points allows generating a reaction force profile. The material properties for the cancerous nodule and healthy matrix and the quality of the mesh were the same to those described in Chapter 5 section 5.2 so that the reproducibility of the analysis was guaranteed. The Fascia was modeled as a hyperelastic, homogeneous and nearly incompressible material. The Young's modulus was assumed of being 15 kPa and the neo-Hookean model was used for fitting against the elastic properties of the material [20].

6.3 Predictive model – peak characterization in the histology

The histological dataset investigated here includes 106 images which were obtained from 30 patients. For each prostate, three or four prostatic slices were cut along the anterior-

posterior plane and sent for histological examination. Some slices were classified as healthy ones, i.e. without the presence of PCa nodules. For the PCa area fraction among all histological slices, its interquartile range is among 8% and 28%, with a mean value of 15% (Fig. 6-2(A)). Most of the PCa nodules are located around the posterior surface of the prostate. The 75% of the nodules are located within 15 mm from the indented surface (Fig. 6-2(B)).

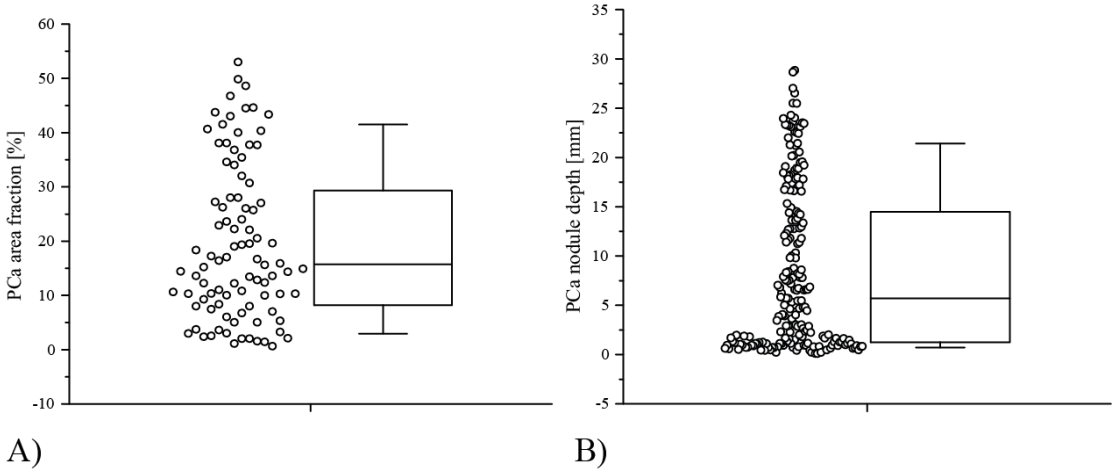

Fig. 6-2. Data of PCa area fraction and distance of the PCa nodule from the posterior surface. A) Box plot for the PCa area fraction which shows an interquartile range among 8 and 28%, a median of 15% and the upper and lower whiskers of 3 and 42%. B) Box plot for the PCa nodule depth which shows an interquartile range among 3 and 15 mm, a median of 6 mm and the upper and lower whiskers of 22 and 2mm.

Using the same predictive methods as presented in the previous chapter, the identification of a PCa nodule started when a peak was identified in the reaction force profile with a sharpness ratio, H/W, greater than 5. Fig 6-3 shows 'Example 1', where a PCa nodule is identified from the histology. As a result, the sharpness value, H/W, was higher than the detection threshold (5) and the predictive model correctly classified it as condition positive (i.e. presence of PCa nodule). On the other hand, 'Example 2' shows another prostatic slice which is healthy (i.e. with no tumor nodule). As a result, the sharpness

value of the peak was lower than the detection threshold, leading to a correct prediction of healthy prostatic slice.

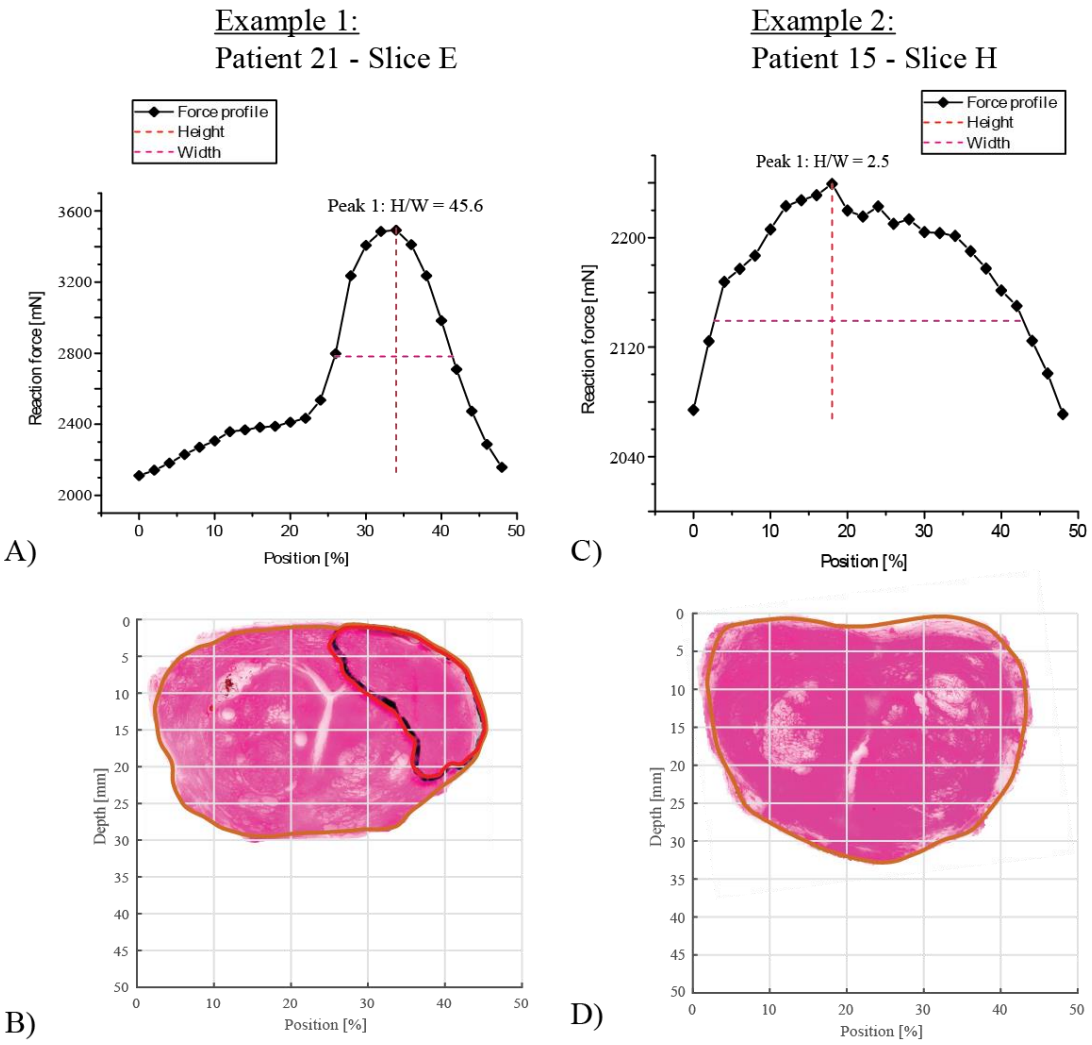

Fig. 6-3. Results of the probing procedure performed in two histology-based models. The Height (H) and Width (W) of the peak were estimated using the MATLAB function *peak*[8].

[8] https://uk.mathworks.com/help/signal/ref/findpeaks.html

6.4 Prostatic tissue classification – sensitivity and specificity

Following the strategy described in the previous section, the complete data-set of the histological images was evaluated with the purpose of quantifying the capability of the predictive model in identifying the presence/absence of cancerous nodule in the prostatic slices and estimating the sensitivity and specificity of the method. Tab. 6-1 shows the results of the predictive model for binary classification, at two different levels, namely histology slices and PCa nodules. The histological examination suggested that 86 prostatic slices showed PCa nodules (i.e. condition positive) and 20 slices were classified as healthy, with no tumor (i.e. condition positive). The proposed methods yielded a sensitivity of 91% and specificity of 100%, although only a low number (n=20) of condition negative samples were considered in this study. However, the predictive model was incapable of detecting the presence of PCa nodules in 8 slices. Therefore, those slices were classified as false negative. It should be noted that all slices with negative condition (healthy) were correctly classified. For all these cases, the force profiles were rather flat and their sharpness was less than the threshold (5) as described in Fig. 6-3 Example 2. On the other hand, 45% of the PCa nodules (95 out of 213) were correctly identified. Among 55% of PCa nodules that are not identified, in a majority of those cases (80%) the PCa nodules appeared in the same slice where at least one other peak in the reaction force profile was identified. In other words, although these nodules were missed from the identification process, the slices they are in were still correctly identified.

Table 6-1. Statistical analysis of the histology-based prediction, on two classification levels, i.e. histology slices and PCa nodules.

Total histology slices: 106			
Condition Positive – PCa in histology: 86 (81%)		Condition Negative – no PCa in histology: 20 (19%)	
True Positive	False Negative	False Positive	True Negative
78	8	0	20
Sensitivity 91%		Specificity 100%	

Total PCa nodules: 213		
Condition Positive – PCa: 213		
True Positive	False Negative	
95 (45%)	118 (55%)	
/	At least one other PCa nodule detected in same slice	No other PCa nodules detected in same slice
	94 (80%)	24 (20%)

6.5 Size and depth of tumor nodule – limitations in PCa detection

The results of the predictive model discussed in the previous section and showed in Tab 6-1 were strongly influenced by the parameters of PCa nodules such as depth, size and geometry.

Fig. 6-4 shows the detectability limits of the PCa nodule with respect to its size and depth (i.e. distance from the posterior surface). It should be noted that the sensitivity increased significantly in detecting nodules with an area larger than 100 mm^2 and a depth smaller than 9 mm (Figs. 6-4(A-B) first column). However, decoupling the effect of the nodule size and depth is still challenging. For the group characterized by the not-detected PCa nodules, the statistical analysis showed that the nodules with size within 10 and 80 mm^2

and distance from the posterior surface with an interquartile range of 10 and 22 mm were classified as false negative (Figs. 6-4(A-B) second column). The third column of the figure shows the statistic of the group characterized by the detected PCa nodules. In this case, the PCa nodules which show an area within 30 and 200 mm^2 and a depth between 0.98 and 9 mm were correctly identified.

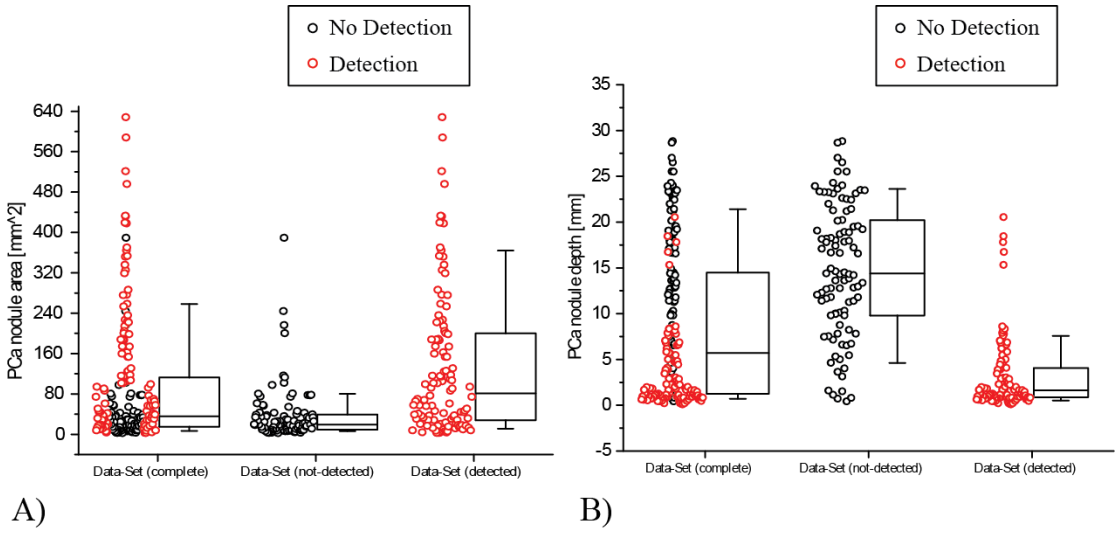

Fig. 6-4. A statistical analysis which shows the results of the predictive model in identifying the presence of PCa nodules and the ranges of the nodule size (A) and depth (B) which define the sensitivity of the method. A) Box plot for the PCa nodule area which shows for the Data-set of the not-detected nodules an interquartile range among 12 and 40 mm^2, a median of 20 mm^2 and the upper and lower whiskers of 70 and 10 mm^2. For the Data-set of the detected nodules an interquartile range among 30 and 180 mm^2, a median of 70 mm^2 and the upper and lower whiskers of 350 and 12 mm^2. For the complete Data-set an interquartile range among 25 and 110 mm^2, a median of 40 mm^2 and the upper and lower whiskers of 230 and 20 mm^2. B) Box plot for the PCa nodule depth which shows for the Data-set of not-detected nodules an interquartile range among 9 and 21 mm, a median of 14 mm and the upper and lower whiskers of 24 and 4 mm. For the Data-of the detected nodules an interquartile range among 1.5 and 3 mm, a median of 2 mm and the upper and lower whiskers of 9 and 2 mm. For the complete Data-set an interquartile range among 3 and 15 mm, a median of 6 mm and the upper and lower whiskers of 22 and 2 mm.

In addition to the statistical analysis presented above, Fig. 6-5 demonstrates the limits for the PCa nodule identification as a ‘function’ of the nodule depth and size. The majority of PCa nodules with area higher than 125 mm^2 were detected. However, the nodules that are located near the indented surface were detected even for cases with a small area. Moreover, the PCa nodules with a depth higher than 9 mm were not-detectable. It is worth noting that, the interplay between nodule depth and size and the ‘uncertainty’ introduced by the tumor nodule geometry may cause an overlap between the data of the detected and non-detected PCa nodules.

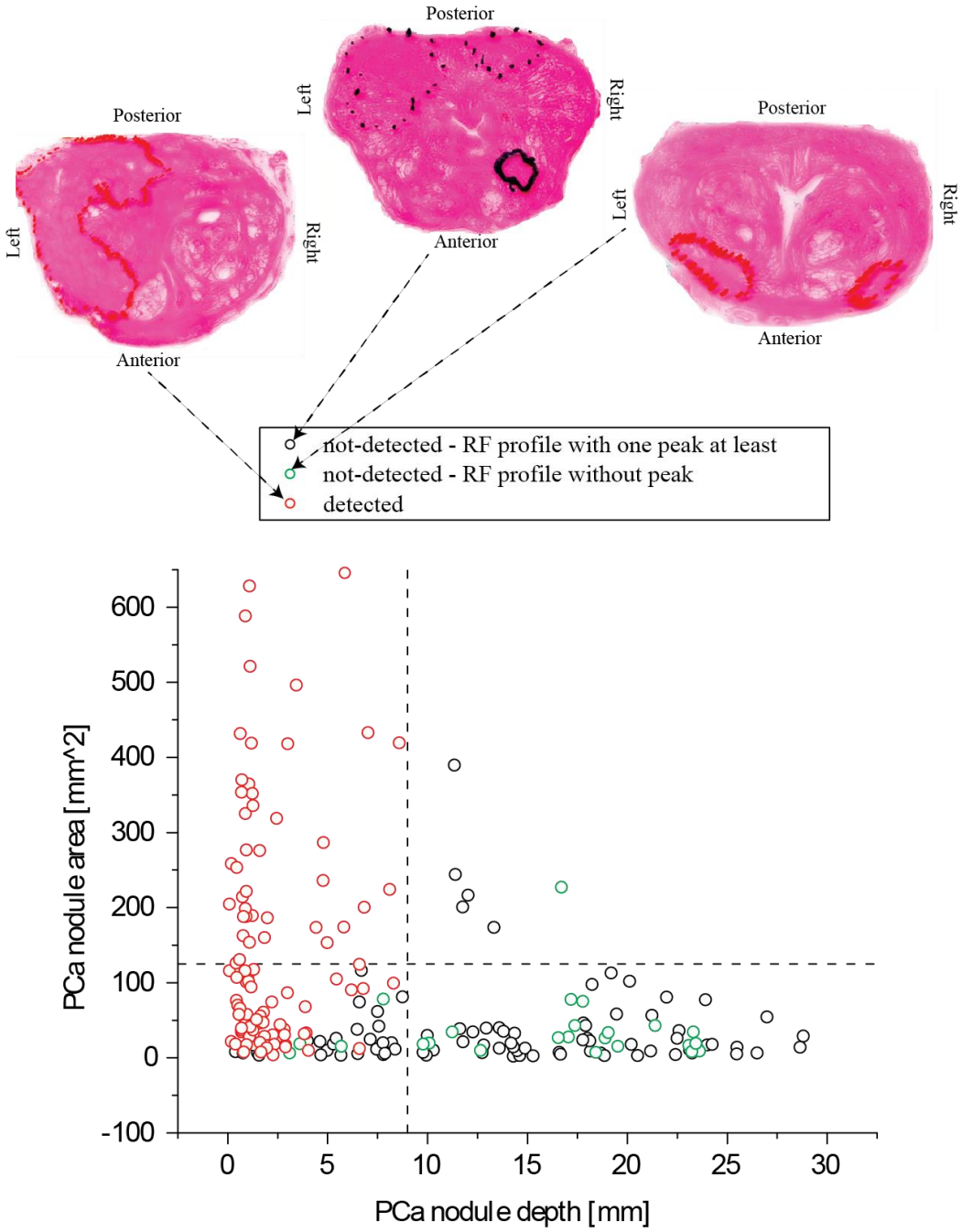

Fig. 6-5. Results of the predictive model in identifying the presence/absence of tumor nodules as a function of the nodule depth and size.

6.6 Summary of results for patients

Table 6-2 summarises the results of the prediction according to patient number. There is a total number of 19 patients who were included in the following analysis, excluding the 'other patients' in the last row where the histological slices cannot be identified to match the patient number. In total, 72 histological slices were examined. As mentioned above, the patients were already diagnosed with PCa and the histological examinations identified the outlines of the prostate and PCa nodules, making it possible to reconstruct FE models as shown in Fig. 6-1. The number and geometry of PCa nodules in those slices could vary significantly -There were slices which showed only one single PCa nodule with a large area and others where the 'degree of dispersion' of the PCa nodules was higher.

Nevertheless, the results showed a good level of accuracy in predicting the PCa nodules. The predictive model was capable of identifying 80% of tumor nodules which were located near the posterior surface of the prostates. However, the nodules located near the anterior surface were undetectable. As a result, the numbers of slices classified as 'true positive', 'true negative' and 'false negative' were 48, 20 and 4, respectively. It should be noted that no false positive, i.e. prediction of tumor nodule when the slice is in fact healthy, exists in the predicted results. In the analysis, the patients were classified as 'positive' if at least one PCa nodule was detected from one of the slices. As a result, only one patient (P11) was classified as false negative and all 3 PCa nodules were located near the anterior surface, undetected.

Table 6-2. Results of the prediction which classify patients with and without the presence of cancer.

	Number of prostatic slices	Tumor nodule in the posterior surface	Tumor nodule in the anterior surface
Patient 4	3 (TP=1, TN=2)	1 (detected)	0
Patient 5	4 (TN=4)	4 (detected)	1 (not detected)
Patient 6	5 (TN=5)	14 (6 detected, 8 not detected)	20 (not detected)
Patient 7	4 (TP=3, TN=1)	3 (detected)	6 (not detected)
Patient 11	3 (FN=3)	0	3 (not detected)
Patient 13	4 (TP=3, TN=1)	4 (detected)	0
Patient 14	5 (TP=5)	5 (detected)	2 (not detected)
Patient 15	3 (TP=1, TN=2)	1 (detected)	1 (not detected)
Patient 16	4 (TP=4)	9 (6 detected, 3 not detected)	7 (not detected)
Patient 17	3 (TP=3)	5 (3 detected, 2 not detected)	2 (not detected)
Patient 18	5 (TP=4, TN=1)	10 (9 detected, 1 not detected)	2 (not detected)
Patient 19	4 (TP=2, TN=2)	2 (detected)	0
Patient 20	4 (TP=2, TN=2)	3 (detected)	0
Patient 21	4 (TP=4)	8 (6 detected, 2 not detected)	1 (not detected)
Patient 22	4 (TP=4)	6 (5 detected, 1 not detected)	1 (not detected)
Patient 23	4 (TP=3, FN=1)	4 (3 detected, 1 not detected)	1 (not detected)
Patient 24	5 (TP=5)	5 (detected)	3 (not detected)
Patient 25	4 (TP=4)	6 (5 detected, 1 not detected)	1 (not detected)
Other Patients	34 (TP=30, FN=4)	42 (24 detected, 18 not detected	30 (not detected)

In summary, the predictive model is capable of classifying prostates based on FE-simulated results using models reconstructed from histological slices. Once again, PCa nodules located near the anterior part of the prostate were challenging to detect using the proposed method. The method can identify the majority of PCa nodules located near the posterior surface and/or with a large volume.

6.7 Prediction of PCa nodule parameters

Fig. 6-6 shows the results of the prediction for two exemplar models. The reaction force profile shows a total number of three peaks as a direct consequence of the presence of the PCa nodules. Since all three peaks have sharpness values, H/W, greater than 5, they are identified as PCa nodules. The probability distribution functions were chosen, accordingly to their H/W value, following the method described in Chapter 5 section 5.3. Using the probability-based method as presented in Appendix A, the probability distribution of the PCa nodule is projected onto the domain of prostate models, where the nodule is represented by the solid red circle as classified by the pathologist and the predicted probability is illustrated using the colorbar along left-right and anterior-posterior axes. Each value of the probability at a given point indicates the likelihood of that point being cancerous.

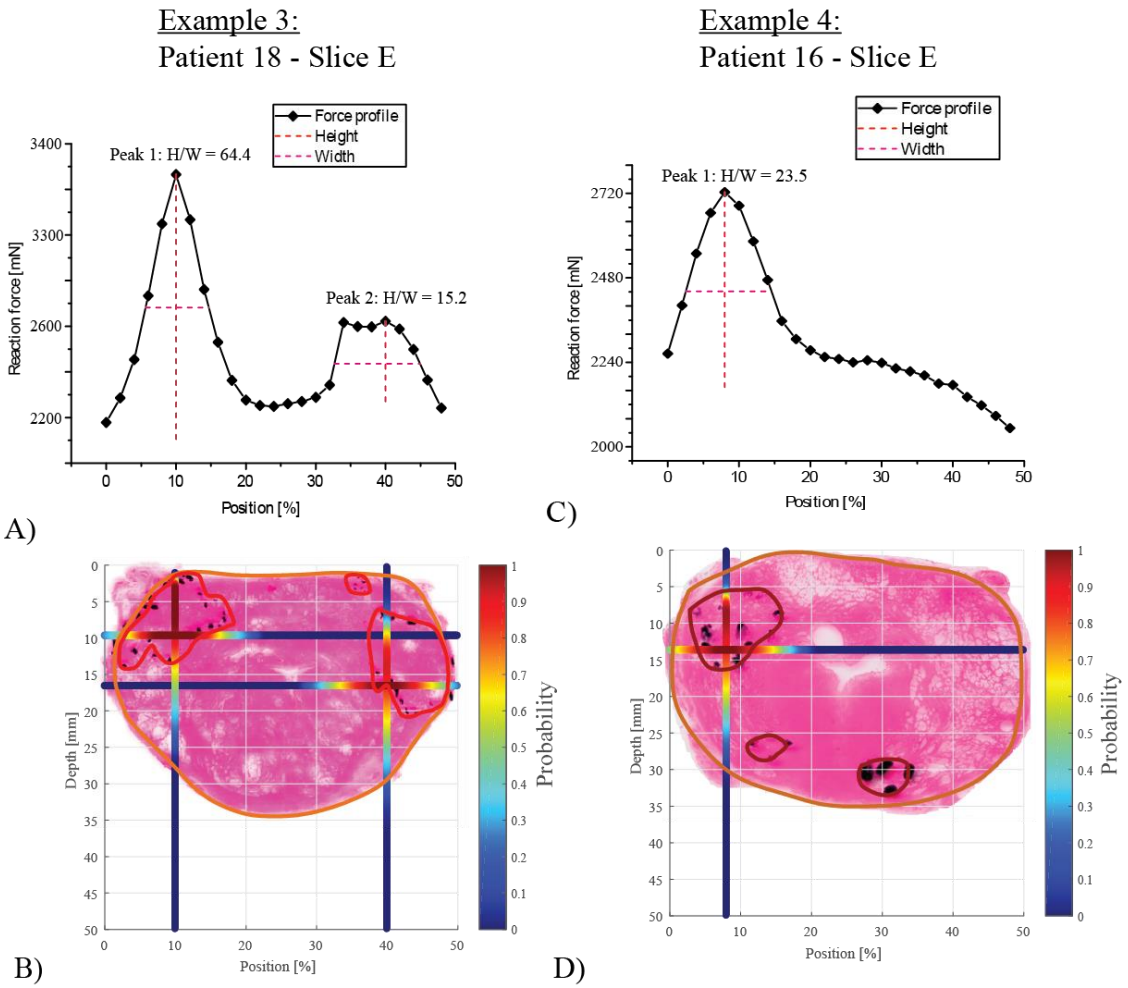

Fig. 6-6. Two examples of histology-based models, including the force profile and the predictions in 2D with illustrated probabilities. A) Force profile and peaks identification for a histology-based model which shows a cancerous nodule near the indented surface (on the left of the prostate model) and a second cancerous nodule located deeper (on the right of the prostate model). C) Force profile and peak identification for a histology-based model which shows a cancerous nodule near the indented surface (on the left of the prostate model) and two cancerous nodules with a smaller size located in the anterior part of the prostate model. B-D) 2D prediction of the nodule(s) identified on the plan depth and position of the histological slices.

Example 3, in Fig. 6-6 (A-B), shows PCa nodules located on the left and right edges of the prostatic slice. The nodules have similar sizes (115 and 124 mm^2), however, the distance between the posterior surface and the edge of the PCa nodule located on the left is 0.1 mm, compared to 7 mm for the large nodule on the right. As mentioned previously, the depth of the PCa nodule could greatly influence the peak sharpness. As a result, the ratio H/W was found to be significantly greater for the case where the PCa nodule is

located closer to the posterior surface. However, the predictive model estimated the nodule position, depth and suspicious area with a good level of accuracy for both cases. The sharpness ratio caused by the nodule (left hand side) in example 3 is 64, leading to a predicted probability map with a large area that has a probability close to '1'. Instead, the peak on the right-hand side in example 3 is less prominent (H/W=15.2) and peak force is also lower. Therefore, the probability map has a much smaller area that has a probability close to '1', indicating that the nodule has a smaller influence in the force peak with less certainty in the prediction.

On the other hand, example 4 in Fig. 6-6 has a PCa nodule with a depth of 5.4 mm and an area of 105 mm^2. The difference between the example 3 and 4 is the presence of two PCa nodules located near the anterior surface of the prostatic tissue in example 4 (depths of 28.8 and 25.5 mm and areas of 28.7 and 13.7 mm^2, respectively). As a result, the method was incapable of detecting the presence of the two small nodules, and this again echoed the findings of limitations in detection capability as presented in Chapter 5 Section 5.6.

6.8 Accuracy of predictions

Fig. 6-7 shows the statistical analysis for the prediction accuracy of all histology-based models considered. To assess the accuracy, two indicators, namely $Index_1$ and $Index_2$, which were defined in Chapter 5 section 5.5, were evaluated. $Index_1$ is defined as the centre-to-centre distance and $Index_2$ represents the 'true positive', i.e. the correctly identified nodule area, in relation to the total nodule area (refer to Figure 5-8). For $Index_1$, the centre of the PCa nodule is calculated using the centre of mass, due to its irregular shape. It can be seen that a high level of accuracy was achieved, where the majority of predictions has a centre-to-centre distance less than 8mm (Fig. 6-7 (A)). For $Index_2$, its

interquartile range is among 0.4 and 0.7, with a mean value of 0.5 (Fig. 6-7 (B)). It should be noted that the probability threshold here was chosen to be 0.5, following the analysis performed in Chapter 5 section 5.3.

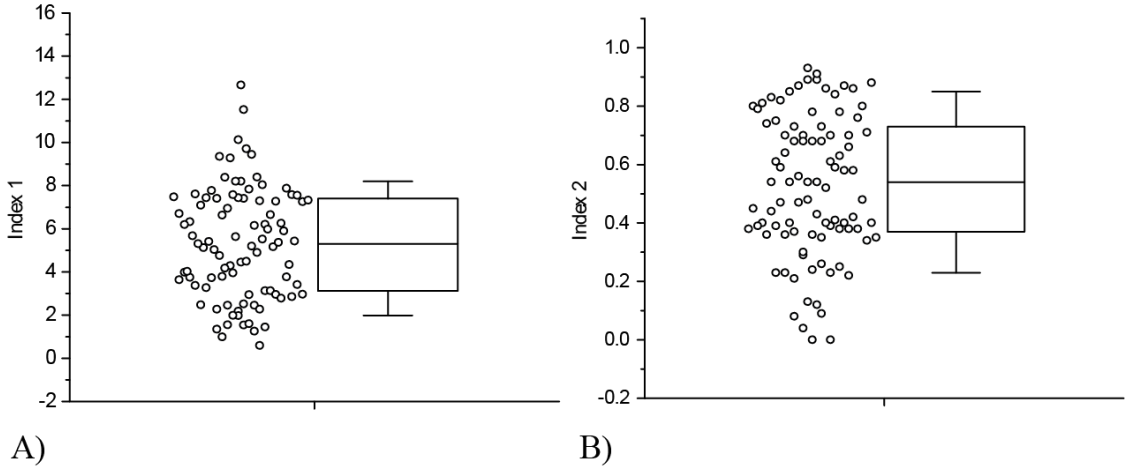

Fig. 6-7. Statistical analysis of the accuracy in predicting the position, depth and suspicious area of the cancerous nodules using two different indices. A) Box plot for the $Index_1$ which shows an interquartile range among 3.5 and 6.5 mm, a median of 5 mm and the upper and lower whiskers of 2 and 8 mm. Box plot for the $Index_2$ which shows an interquartile range among 0.3 and 0.7%, a median of 0.5% and the upper and lower whiskers of 0.2 and 0.8%.

6.9 Complications

Fig. 6-8 shows three examples of histological images where the choice of the models aimed to describe the limitations of the prediction. Example 5 shows a nodule which is small in area (size of 28.4 mm^2 and depth of 1.8 mm) and other two which are adjacent along the left-right axis (size of 22.3 and 16.72 mm^2, depth of 4 and 2.9 mm). As mentioned in Chapter 5 section 5.6, the predictive model may have a poor accuracy in identifying tumor nodule with these features. Therefore, the accuracy in predicting the PCa nodule position, depth and suspicious area was significantly lower as shown in Fig. 6-8(B).

Fig. 6-8(C) shows a PCa nodule located near the posterior surface but with a widespread along the left-right axis of the prostate (size of 214.1 mm^2 and depth of 0.75 mm). Therefore, the reaction force profile does not show a very 'sharp' peak (H/W=19.9), leading to a nodule located deeply in the prostate. The geometry justified the losing in predicting accurately the tumor nodule features as visible in Fig, 6-8(D).

Fig. 6-8(E) shows a PCa nodule with an extremely large volume (size of 351.6 mm^2 and depth of 0.7 mm). As seen in Fig. 6-8(F) the prediction of the cancerous area e was significantly underestimated.

Interesting, the variation of the magnitude H in three cases. Patient 21 shows for the peak1 a magnitude H of 2770 mN which is caused by the cancerous nodule with size 28.4 mm^2. However, Patient 17 and Patient 14 shows a higher magnitude H (3300 and 3800 mN, respectively) which is caused by a cancerous nodule with size of 214.1 mm^2 and 351.6 mm^2, respectively. It should be noted that the cancerous nodules in the three cases are located near the indented surface. Therefore, it might be possible to find a correlation between the size of the cancerous nodule and the magnitude H, which might improve the accuracy of the predictive model in distinguishing nodules with diverse sizes.

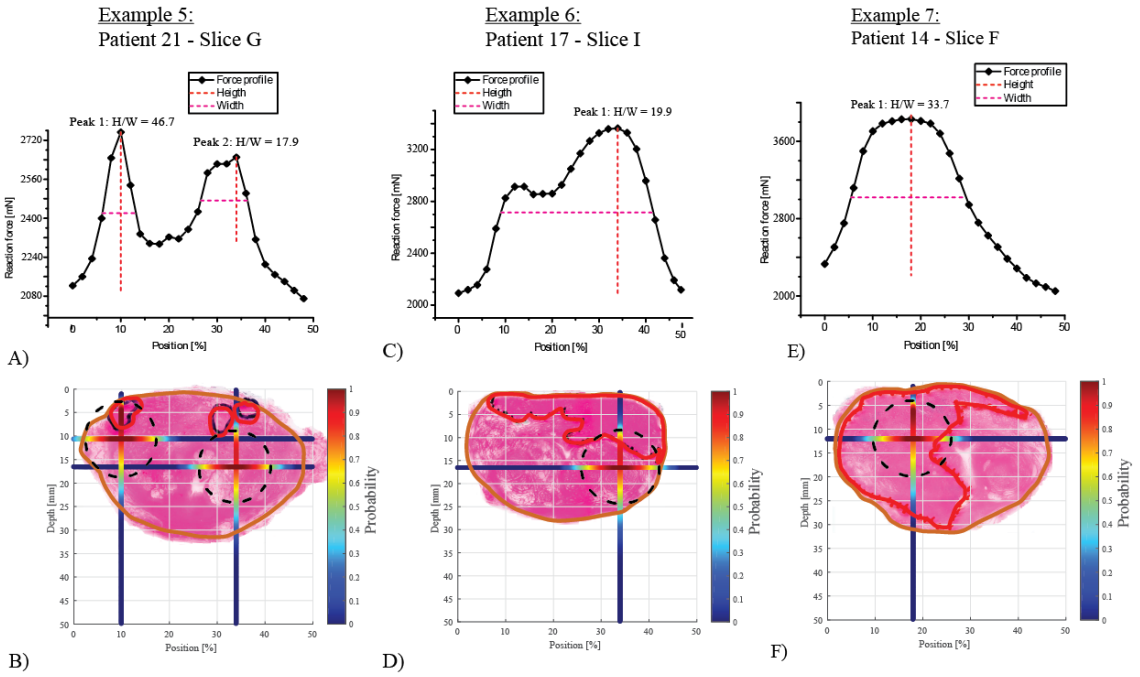

Fig. 6-8. Three representative examples, demonstrating the limitation of the predictive model in estimating the cancerous nodule features such as position, depth, and size. The top of the figure shows the force profiles and peak(s) identification for a histological-based model with a small cancerous nodule (on the left of the slice) and other two which are adjacent along the left-right axis (A), a second model where the cancerous nodule widespread along the left-right axis (C) and a model where the cancerous nodule shows an extremely large volume compared with the other two cases (E). The bottom of the figure shows the prediction of the nodule(s) existence into the histological slice domain for the three cases.

6.10 Concluding remarks

The chapter further examined the capability of the predictive model in identifying and quantifying PCa nodules based on simulated palpation force profile. A total of 106 histological slices were used to reconstruct prostate models and the proposed probability-based predictive methods were applied to estimate the probability distributions of the existence of PCa nodules. The results showed a good level of sensitivity (91%) and a high level of specificity (100%, potentially due to the nature of the dataset). It has been shown that, once again, despite of a high proportion of correct predictions among all PCa nodules, the majority of undetected nodules were those located far away from the posterior surface. Moreover, the statistical analysis showed the ‘certainty’ in nodule

identification could increase significantly when the tumor nodules have a size over 125 mm^2 and located within a depth of 9 mm from the posterior surface.

In conclusion, the predictive model showed promising sensitivity and specificity as well as the accuracy in prediction in terms of the size and depth of PCa nodules. All the probing force profiles used in this chapter, as aforementioned, were from FE simulations. In the next chapter, as a final stage, the predictive model will be validated using instrumented probing data acquired from ex vivo experimental measurements.

Chapter 7

Validation of Predictive Methods – Stage 2: Measurements on Ex-vivo Prostate

Contents

7.1 Summary

In Chapters 5 and 6, the predictive method for detecting and characterizing PCa nodules has been presented. The method requires the reaction force profile from probing the prostate using instrumented palpation. Therefore, the predictive model can work with a deployable medical device [19], with the aim of providing quantitative and objective identification of PCa nodules. The method has been tested using simplified prostate models in Chapter 5 and histology-based models (with simulated FE results) in Chapter 6. The results for binary classification of PCa nodules, based on sensitivity and specificity

outcomes, were promising. Furthermore, the estimation of the PCa nodule parameters such as position, depth and size has also shown a high degree of accuracy.

In this chapter, the capability of the predictive model will be assessed, at a final stage, using the experimental measurements obtained by instrumented probing of *ex-vivo* prostates. Data analysis similar to what has been carried out in Chapters 5-6 will be repeated here.

7.2 Instrumented probing and histological study

The palpation device exploited for probing the ex vivo prostate, as shown in Fig. 7-1, was designed to work with a Force-Resistor Sensor (FSR) of 10mm in diameter [19]. The device was placed onto a loading stage with three-dimensional motion control. The data from the sensor were acquired using a data-acquisition (DAC) hardware system and process digitally exploiting a LabVIEW interface. When a contact between the posterior surface of the prostate and the probe was identified, a vertical displacement of 8mm was applied along the Z-direction and the force feedback data was acquired at that depth.

The *ex-vivo* probing procedure was performed along the posterior surface of the prostate, shortly after radical prostatectomy using laparoscopy surgery, at an array of probing points, as illustrated in Figs. 7-1 (C-D). A minimum of 6mm distance was left between two probing points to avoid overlapping between two consecutive measurements. After the measurement, surgical clips were used in each row for permitting the histological examinations of the columns where the mechanical measurements were performed. A planar section of the prostatic tissue marked with the surgical clips was collected and sent for the histological examinations. The prostatic slices were stained using standard H&E technique, followed by patho-histological study, where the outlines of the cancerous tissues were determined by a consultant pathologist. As a result, a total number of 9

prostates were included in this study, each having 36-42 number of probing points with the histological examination.

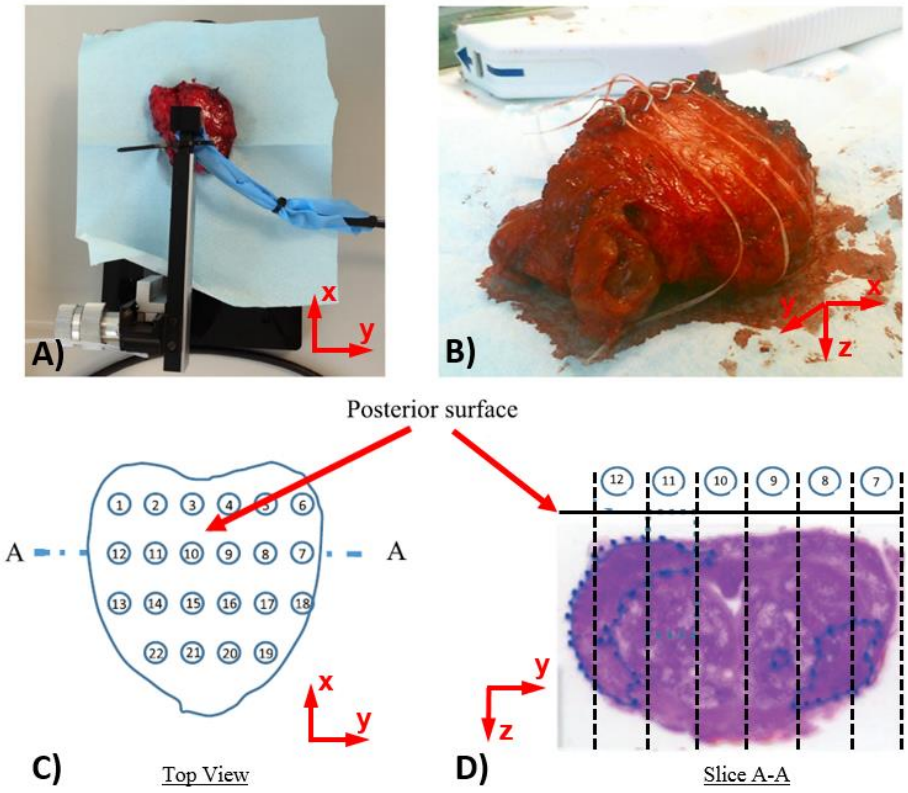

Fig. 7-1. The experimental and sectioning methods. A) The instrumented probing stage, allowing the movement of the probe and performing the probing at a certain depth of the whole prostate, which is located on a rigid testing platform with its posterior surface facing upwards; B) The prostate marked with the threads and clips, permitting the histological exams of the columns where the probing was performed; C) the probing sites and the numbering matrix used to divide the posterior surface in columns; and D) the histological slice 'under' a series of probing points along the left-right axis

7.3 Experimental Validation – a clinical feasibility study

All probing data from experimental measurements on 9 patients were collected, as illustrated in Fig. 7-2 (A). All probing forces at the depth of 8mm ranged between 0 to 3.2N. For the tissue columns directly underneath each probing point obtained from the

histology images, their pathological conditions are also shown in Fig. 7-2 (B). It should be noted here that the tissue column is believed to be 'cancerous' if PCa is identified in it from histology, regardless of the tumor's size and depth. As data suggests, using the values of probing forces themselves, we are unable to effectively distinguish the cancerous 'columns' from the non-cancerous ones. This, once again, highlights the complexity of nodule identification and the necessity of employing methods other than relying on the probing force at a single point.

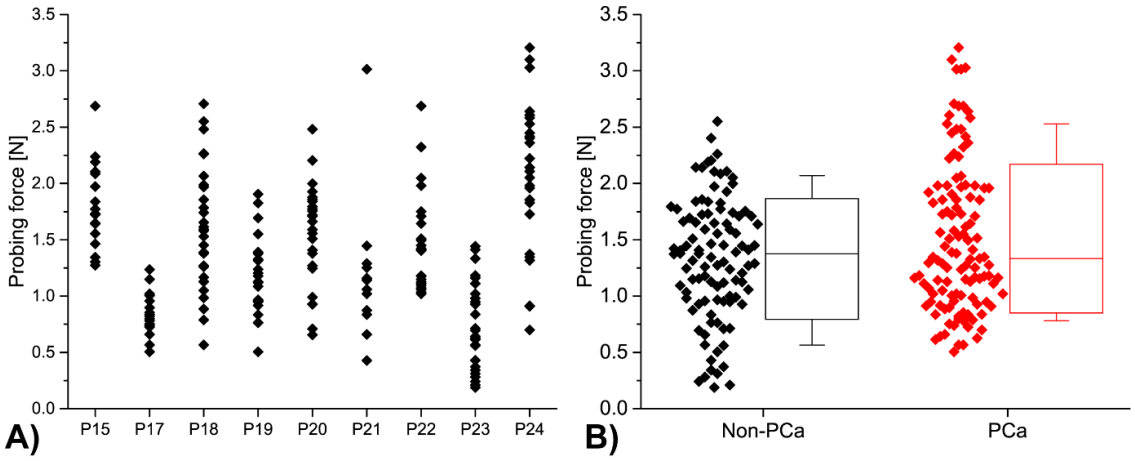

Fig. 7-2. Experimental data of probing forces classified by their (A) patient number and (B) the pathological conditions of the 'tissue column' directly underneath the probing points (B).

All point-wise probing data were then reformatted, for each patient, into force profiles along the left-right axis, following the procedures previously described in Fig. 7-1. The cubic spline method was used for fitting the probing data along the left-right axis. As a result, a total number of 33 force profiles with their corresponding histological slices underneath the probing points from 9 patients was analysed using the proposed methods to predict the probability distributions of tumor nodules along both axes in the prostate, and two representative examples are illustrated below. The H&E stained histology slice

E of Patient 24 showed two PCa nodules, outlined in red. Both were identified by the proposed methods based on the experimental force profile in Fig. 7-3 (A), and the predicted distributions of the 'PCa existence' were also plotted along both anterior-posterior and left-right axes. Interestingly, although two peaks identified from the force profile have rather different peak values, they have similar peak sharpness (peak 1 has a peak sharpness of 17.70 and peak 2 11.97) that falls into the same division ($10<D/W<20$, as illustrated in Fig. 7-3 (B)), leading to the same probability prediction. For the slice C of Patient 21, the histology indicated two PCa nodules, very close to each other. The probing force profile, in contrast, showed two identified peaks (sharpness of peak 1 is 96.78 and peak 2 11.01). The extremely sharp peak 1 resulted in a predicted nodule very close to the posterior surface and may be caused by both nodules. Peak 2, however, resulted in a predicted nodule that was not recognised as PCa by histology, making such prediction a 'false positive'.

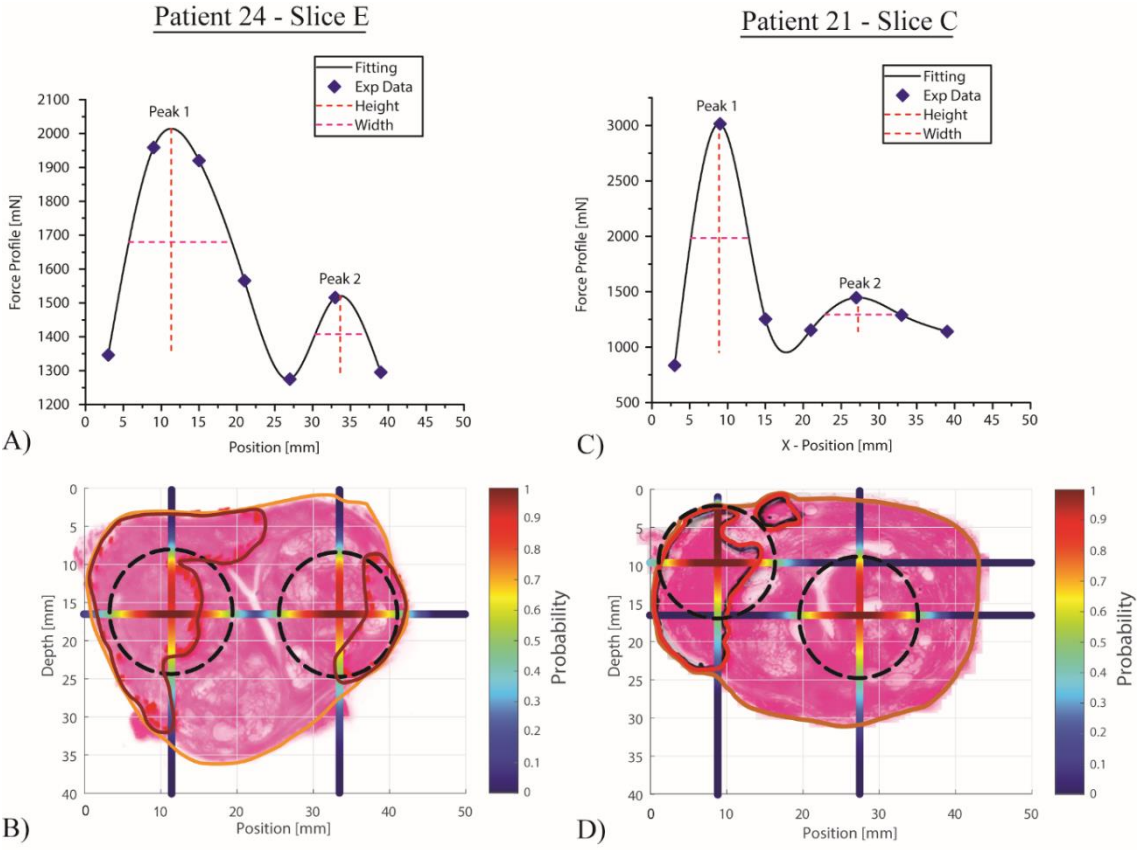

Fig. 7-3. Slice E of Patient 24 and slice C of Patient 21 are illustrated here, as two examples of PCa nodule identification. Histology slices, reconstructed outlines of prostate and PCa nodules and the predictions were stacked for visualization purpose. A probability threshold of 0.5 was used to obtain the predicted PCa nodules (in black).

Fig. 7-4 shows the results of the prediction for the 33 force profiles from the 9 patients. As discussed, the prediction was based on the peak characterization. The prediction threshold allowed the binary classification of the prostatic slices. More importantly, the values of the ratio H/W showed a significant 'dispersion'. Therefore, the predictive model was capable of classifying between PCa nodules which showed diverse important clinical parameters such as position, depth and size. As a result, the ratio H/W values fell into a diverse division and the probability distribution of the 'PCa existence' was obtained (Appendix C). It should be noted the improvement in the diagnosis using the predictive model against the approach of evaluating the single force values (Fig. 7-2). The results of

the reaction force values showed statistical distribution which does not guarantee a reliable identification and characterization of PCa as well as the novel methodology.

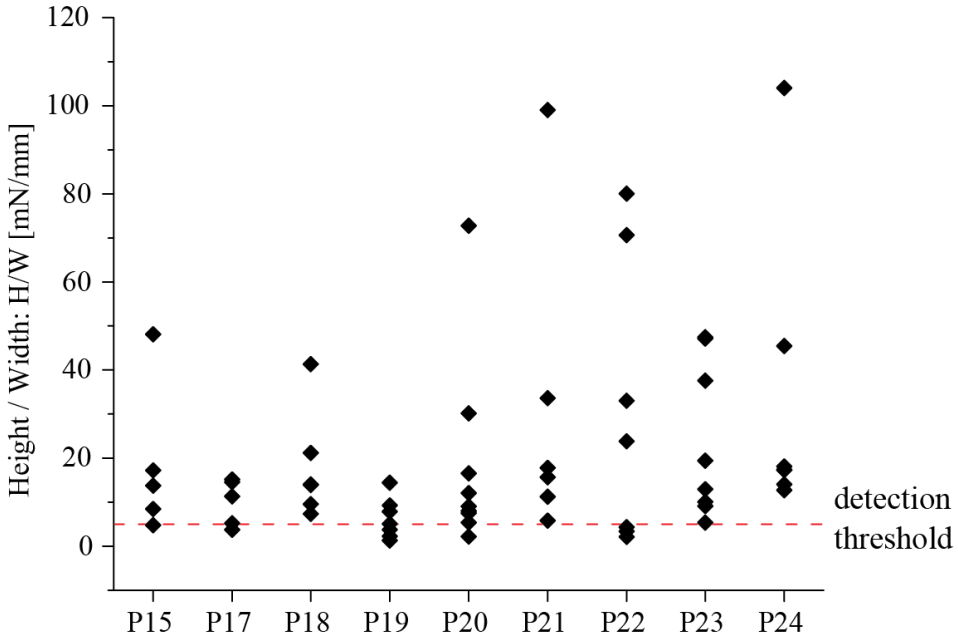

Fig. 7-4. Results of the prediction based on the peak characterization which were obtained by probing the posterior surface of the *ex-vivo* prostates.

7.4 Experimental data – Prediction

Here we further assess the effectiveness of the proposed methods in identifying the tumor nodules, at three different levels, namely histology slices, PCa nodules and patient level for binary classification tests. Firstly, the classification test for the histological slices (n=33), as shown in Table 7-1, demonstrated the capability of the proposed methods, yielding a sensitivity of 96% and specificity of 67%, although a low number (n=6) of condition negative sample should be noted. On the other hand, for classification at the level of PCa nodules (n=53), 57% PCa nodules were correctly identified, and among

those which were not identified, the majority of nodules were classified through the identification of at least one other PCa nodules in the same slice.

Table 7-1. Statistical analysis of the prediction, on two classification levels, i.e. histology slices and PCa nodules.

Total histology slices: 33			
Condition Positive – PCa in histology: 27 (82%)		Condition Negative – no PCa in histology: 6 (18%)	
True Positive	False Negative	False Positive	True Negative
26	1	2	4
Sensitivity 96%		Specificity 67%	

Total PCa nodules: 53		
Condition Positive – PCa: 53		
True Positive	False Negative	
30 (57%)	23 (43%)	
/	At least one other PCa nodule detected in same slice	No other PCa nodules detected in same slice
	21 (91%)	2 (9%)

In addition to the statistical analysis presented above, the classification outcome was also found to be affected by the depth and size of the PCa nodules. Most of the PCa nodules located within 10mm (i.e. the depth of d as illustrated in Fig. 5-2 of the Chapter 5 section 5.3) were correctly identified, as shown in Fig. 7-4 (A) and, in contrast, almost all non-detected PCs nodules are smaller than 125mm^2, i.e. equivalent to a diameter of 12.5mm. This result is consistent to the findings illustrated in Figs. 6-4 and 6-5 in the previous chapter. When the area and depth of all nodules are plotted against each other, in Fig. 7-

4 (C), the limitations in detecting PCa nodules can be observed clearly. PCa nodules which show an area higher than 125mm^2 are detectable. However, PCa nodules which are located deeply into the prostatic tissue, with a depth higher than 9mm, are non-detected. Moreover, the figure shows a region of overlap between the detected and not-detected PCa nodules due to the interplay between the nodule size and depth which influence the reaction force measurements. These detection limits are, once again, in line with the findings illustrated in Fig. 6-5 in the previous chapter.

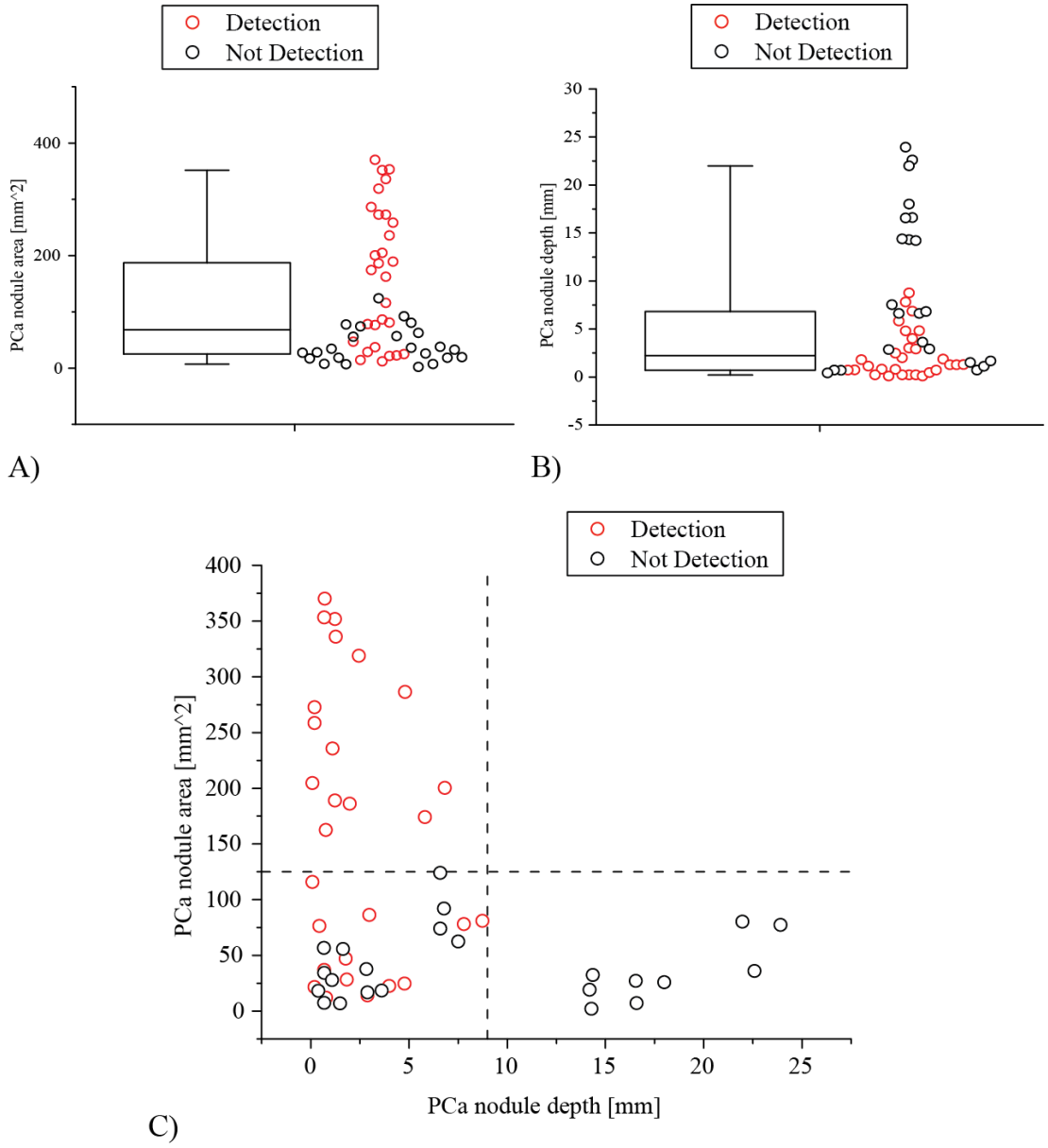

Fig. 7-5. Statistical distribution of the tumors volume fraction identified in the histological slices and their distance from the posterior surface.

Table 7-2 shows the results of the prediction at the patient level. The patients were classified as Condition Positive (presence of cancer) if the predictive model identified the presence of a peak with ratio H/W higher than 5. It should be noted that the study did not include patients without PCa. As mentioned, the method was incapable of detecting PCa

nodules which appeared in the anterior surface of the prostate. The outcome was confirmed by the data which are illustrated in the last column of the table.

Table 7-2. Results of the prediction in classifying presence of PCa at the patient level.

	Number of prostatic slices	Tumor nodule in the posterior surface	Tumor nodule in the anterior surface
Patient 15	3 (TP=1, FP=1, TN=1)	1 (detected)	1 (not detected)
Patient 17	3 (TP=3)	5 (3 detected, 2 not detected)	1 (not detected)
Patient 18	4 (TP=4)	10 (3 detected, 7 not detected)	2 (not detected)
Patient 19	4 (TP=2, TN=2)	2 (detected)	0
Patient 20	4 (TP=2, TN=1, FP=1)	3 (2 detected, 1 not detected)	0
Patient 21	2 (TP=2)	5 (3 detected, 2 not detected)	0
Patient 22	4 (TP=3, FN=1)	7 (6 detected, 1 not detected)	0
Patient 23	4 (TP =4)	4 (detected)	4 (not detected)
Patient 24	5 (TP=5)	7 (6 detected, 1 not detected)	1 (not detected)

7.5 Concluding remarks

In this chapter, the proposed predictive model was further assessed for the identification and characterization of PCa nodules based on mechanical palpation performed on ex vivo prostates. The measurements were obtained by probing a whole *ex-vivo* prostate along the posterior surface using a certain point pattern. The number of patients involved in the clinical study was 9, who were diagnosed with PCa and underwent total prostatectomy. The device recorded the reaction force from the probe at the certain probing depth and the histology slices directly under the probing points were also analyzed by a pathological consultant. The experimental measurements showed statistical distributions between the group of healthy and cancer 'columns' with respect to their measured for0ces, and this showed that using the force alone cannot guarantee a reliable classification for the presence of PCa nodules in the prostate.

Following the proposed predictive methods in Chapter 6, the capability of the method was assessed in predicting the PCa nodules at three levels, namely, histology slices, PCa nodules and the patient level. Interesting, the experimental force profiles show values and peak shapes which are in agreement with the force feedback obtained by simulating the probing procedure. Therefore, the assumption of the stiffness ratio of 2.5 (and 2D FE prostate model) might not affect significantly the sensitivity of the predictive model. The method showed a correct prediction even for nodules which are small in size, with an equivalent radius of 6mm. However, the detection of PCa nodules located in the anterior surface of the prostate proved to be challenging. The method was shown to be incapable of detecting PCa nodules located deeper than 10mm. It should be noted that the results of the prediction are in agreement with the conclusions using the histology-base models, for nodules larger than 125mm^2 and with a depth of less than 10mm. The false positive may be caused by the not optimal contact between the sensor and the indented surface. The

problem is more evident when the measurements are performed on the edge of the prostatic tissues. However, the detection threshold is set for avoiding this type of 'noise' in the experimental measurements as mentioned in chapter 5 Section 5.3. The number of detected PCa nodules was approximately 60%. For each of them, the predictive model provided the probability of the nodule 'existence' which allowed the estimation of the nodule position, depth and size, which are important clinical parameters for PCa diagnosis.

To summarize, the method provides a quantitative and objective classification of the PCa nodules, however, there are a number of limitations. One limitation of the study is in the number of patients, which could be improved into the range of sub-hundreds for improving the effectiveness of the assessment. In addition, all patients chosen for this study were already diagnosed with PCa. A further analysis is needed to include more patients, and more importantly, a patient group that is more representative of the total population, i.e. the inclusion of patients without PCa. Therefore, it would be possible estimating the maximum H/W value for a healthy sample instead of assuming an empirical value for the detection threshold of the predictive model.

The mechanical palpation in the clinical study was performed *ex-vivo* which means that the prostate was placed on top of a flat and rigid surface. As a result, the probing depth can be chosen and well-controlled. However, during the *in-vivo* procedure the probing depth could be extremely difficult to control and verify, often relying on the experience and interpretation of the practitioners. Furthermore, the anatomy of the patients can further complicate the *in-vivo* measurements, and the number of available probing points could be limited and the probing depth could vary significantly between patients. Furthermore, the reliability in the contact between the sensor and the prostatic tissue can vary, which may subsequently influence the performance of the predictive model. Finally,

the accuracy of the predictive method can also be affected by artefacts in the force measurements which could be caused by the blood perfusion, muscles tension and pulsation, all of which were not considered in the current framework. Nevertheless, the results showed a sensitivity of 96% and a specificity of 67%, promising as a starting point for future in vivo study

The current screening protocol often uses a combination of DRE and PSA outcomes. The clinicians are guided by those outcomes for identifying cancerous nodules in the prostate and deciding if the patient needs further examinations such as biopsy. In some cases, the clinician can decide if an MRI scan is necessary prior to biopsy, and the use of MRI is currently getting more common in most clinical practices. In this context, the results shown by the predictive model coupled with the palpation data presented a certain degree of improvement for PCa identification. From previous clinical studies, the DRE and MRI showed a sensitivity of 38% and 33.3% and a specificity of 66% and 82%, respectively [98]. Therefore, the clinical studies suggested the need for developing a diagnostic method which is able of detecting small and/or deeply PCa nodules with the aim of improving the diagnosis of PCa, at an earliest possible stage. The proposed method has shown a sensitivity and a specificity of 96% and 67% and could be useful to complement the existing DRE and MRI procedures. However, the detection of small nodules is still challenging, as shown in the results above, since the force profile has a low sensitivity to the nodules with small diameter (<5mm). Furthermore, the prediction is negatively affected by the 'false positive' which may be caused by the presence of benign condition (e.g. BPH) in the prostatic tissue, which is not considered in the current predictive framework.

In conclusion, the results of the novel diagnostic method overcome the accuracy for PCa detection in comparison with DRE and MRI techniques even maintaining the same

specificity. However, the method is based on instrumented palpation which implies a not invasive, safe and inexpensive procedure. As a further novelty, the predictive model provides an important clinical parameter for staging cancer and improve the prognosis of the patient. Therefore, the method does not replace the TRUS biopsy, however, it might be included in the screening protocol in conjunction with the PSA test for helping the clinicians in detecting and characterizing PCa and classify patients who need a biopsy.

Chapter 8

Looking back and working forward

Contents

8.1 Looking back

The multidisciplinary efforts involving engineering, biological and medical sciences allowed the development of novel methodologies and technologies for the ultimate goal of improving the effectiveness of current clinical diagnosis of prostate cancer. More specifically, in this thesis, the goal was to make sense of the tissue characterisation data (e.g. in the format of point probing) and make use of such data for tumor nodule characterisation and identification. Currently there are few methods available for such a challenging task, due to the complexity and a high number of unknowns in many aspects of the problem. This thesis attempted to achieve such a research objective, by employing mathematical and numerical concepts, involving such methods like soft tissue modelling, inverse optimisation methods and finite element analysis. A number of methods, verified in either practical or clinical contexts, were proposed for different purposes, all contributing to the grand picture of 'prostate cancer diagnosis based on instrumented palpation'.

The contribution, concluding remarks and potential impact of the thesis are summarized as follows:

Chapter 3: Identification of Tumor Nodules in Soft Tissue – An Inverse Finite-Element Framework based on Mechanical Characterization

- ✓ A computational framework for identifying the presence/absence of tumor nodule based on mechanical palpation without a priori knowledge of the patient anatomical details, the position or size of the tumor nodule.

The advantage of this diagnostic framework is the capability of identifying the presence of tumor nodule based on measurements of the reaction force values obtained from tissue probing using only a small number of probing points. Therefore, it is possible for the practitioners to obtain key information such as the presence of a stiff nodule using a less-invasive and inexpensive approach such as instrumented palpation. The framework, as it currently stands, does not require, but can be complementary to, medical imaging techniques. Therefore, the impact of such a framework could be a potential assisted computational tool for early screening of prostate cancer and patient stratification.

Chapter 4: Sensitivity Analysis of Inverse FE Framework

- ✓ A benchmark for cancer nodule detection using mechanical probing as a function of the tumor nodule size, depth and stiffness

The diagnostic framework, proposed in Chapter 3, showed significant influences of the features of tumor nodules such as their size and depth and results showed limitation in detecting nodules either located deeply in the prostate (from the posterior surface) or of a small size. Therefore, the sensitivity of the proposed methods to those variables needs to be investigated. The outcomes allowed defining a benchmark for classifying the presence/absence of the tumor nodule as a function of its parameters such as the size and

depth. Therefore, the parametric study presented in this chapter was able to quantify the 'uncertainties' in the nodule identification process. The study presented in this chapter could serve the purpose of understanding systematically the capability of the proposed nodule identification methods and their limitations with the aim of developing new strategies for improving the sensitivity of the tissue probing procedure.

Chapter 5: Probability-based Predictive Methods for PCa Nodule Identification

- ✓ A computational framework for identifying and estimating the position, depth and suspicious area of tumor nodule(s) in prostate based on a probability method.

The proposed framework was capable of providing a probability-based prediction for, as well as a binary outcome of, the existence of tumor area in prostate, based on the characterisation of the peak in the force profile obtained from point-by-point probing. Since a deterministic solution cannot be guaranteed due to the nature of the inverse problem, a probability-based method was proposed based on randomly-generated models, representative of the prostate-tumor system. The proposed method was tested using a subset of the random models in order to understand its sensitivity to a range of parameters that are related to the model and the tumor nodules. Illustrative results indicated that the method was capable of predicting not only the existence but more importantly the size and depth of the tumor nodules, with a good level of accuracy.

Chapter 6: Validation of Predictive Methods – Stage 1: Models Reconstructed from Histological Images and FE-Simulated Instrumented Probing

- ✓ A further study based on the methods proposed in Chapter 5, by using a large dataset of in silico measurements based on models reconstructed from patient histological data.

Further from the results presented in Chapter 5, an in-silico dataset of probing measurements based on prostate models reconstructed from patient histological images was obtained using Finite Element. The analysis has been performed for evaluating the capability of the predictive model in classifying healthy/cancer at three scales: the tumor nodules, the prostatic slices and the patients. Furthermore, the accuracy in predicting the location and suspicious area of the tumor nodules was evaluated. This study suggested the potential of the proposed methods for applying to make sense of the patient probing data, which will be examined in the next chapter.

Chapter 7: Validation of Predictive Methods – Stage 2: Measurements on Ex-vivo Prostate

- ✓ A further study based on the methods proposed in Chapter 5, by using a large dataset of experimental measurements on ex vivo prostates and their corresponding histological studies.

The proposed predictive method was further validated using experimental data obtained by performing mechanical probing in ex-vivo prostates. The characterization of the peaks identified in the reaction force profiles could lead to classification of the presence/absence of the tumor nodules and quantifications of their position, depth and suspicious area in the prostate. The validation was performed based on a comparison between the predictive model outcomes and the corresponding histological images of the prostatic tissues directly under the probing points. The results have shown that the predictive framework is able to identify and characterize the tumor nodule(s) in prostate with a level of good confidence, however the prediction can be influenced by the following sources of uncertainties:

- Cancer heterogeneity – tumor nodule(s) position, depth, size, material and 'dispersion'
- Inter-patient variations – size and geometry and of the prostatic tissues
- Intrinsic 'noise' in the experimental mechanical measurements

The advantages of the deployable palpation device coupled with the predictive model are that the method is not invasive, inexpensive, safe and easy to perform. Therefore, the method may be a complementary diagnostic tool for PCa. However, the aggressiveness of the cancer is still a challenging task. As future work, it will be interested to develop a multiscale model with the aim of couple the Gleason Score with the stiffness values which can be estimated by the probing procedure and inverse analysis.

In conclusion, the predictive model may increase the quality of the PCa identification and it can be translated into clinical practice for improving the early cancer detection. Furthermore, the clinicians may have a complementary tool for distinguishing in patients who need a biopsy and heavy treatments without a *priori* knowledge of the patient. Therefore, the method can decrease the cost for the healthcare.

As a whole, this thesis presented a number of computational frameworks with predictive capabilities that could lead to improved effectiveness of early screening for prostate cancer. The proposed methods are complementary to the instrumented palpation strategy that is currently being developed by a number of medical centres and research groups around the world and are certainly compatible to other recent developments in early diagnosis of PCa using methods such as advanced medical imaging [145].

8.2 Working forward

The methodologies, results and conclusions presented in the thesis, as they currently stand, have certain limitations, which need further investigations for accelerating its translation into clinical practice.

Heterogeneity in cancer and healthy tissue

The assumption of homogeneity of the material properties for healthy and cancerous tissues adopted in Chapter 3, 4, 5 and 6 presents one of the crucial limitations which might cause a source of error in the results. The material properties can vary between regions of the same prostate (intra-patient) and between patients (inter-patient). More importantly, the stiffness ratio between the healthy tissue and cancer can vary based on the aggressiveness grade of cancer. However, in the literature there is a lack of mechanical characterization of the prostatic tissues. Therefore, a future investigation on this topic will be crucial. For instance, a new protocol should be developed for recording the force vs. displacement curves during the probing procedure performed in the posterior surface of the *ex-vivo* prostates. Ideally, the data should be recorded in each probing point until reaching the maximum displacement with the aim to evaluate the prostate mechanically.

The diagnostic frameworks developed in chapter 3 and 5 have as a final goal of being a complementary tool for decreasing the number of unnecessary biopsies. Despite this, the task is still challenging. Therefore, the outcomes obtained with the computational frameworks can be 'merged' with outcomes of other methodologies, proposed for diagnosis purpose. There are experimental evidences which show how the perfusion, diffusivity and vascularization of the soft tissue vary due to the presence of cancer [146]–[148]. Therefore, the analysis of the variation of these parameters for healthy and cancerous tissues can improve the diagnosis. The analysis can be performed using

multiscale modelling and histological images. However, for a higher scale analysis, MRI and CT images need to be exploited.

The developing of multiscale modelling for studying parameters as diffusivity at diverse scales can be used for treatment purpose. For instance, A model for drug delivery can be developed. Likewise, an optimization method for a patient specific treatment for cancer in soft tissue can be suggested for avoiding damage in the healthy tissues, which surround the cancer, and an optimal dose of the drug for decreasing the pain and weakness of the patients [149].

Material modelling of prostatic tissue

Most biological tissues, including prostate, are time-dependent material. The viscoelastic parameters change in presence of pathological conditions [39], [64] and they can in fact also be used as an index for distinguish between presence/absence of cancer. Therefore, it is worthwhile to investigate the role of the time-dependent properties of prostate tissue on the nodule identification outcome, although the probing measurement in this thesis was quasi-static, which to some extent could mitigate this issue.

Deformation of the probe and its scaling

The assumptions suggested in Chapter 3, 4, 5 and 6 for modelling the material properties and the contact between the probe and the biological tissue surface can be one of the limitations of the diagnostic frameworks. In reality the probe may not be a rigid material. Furthermore, the contact between probe and tissue may not be completely frictionless. The sensitivity of the procedure depends also on the size of the indenter. As shown in Chapter 5 a small indenter can increase the horizontal ‘resolution’ of the identification process that may lead to improved diagnosis, however it is unclear how small the indenter needs to be for optimal outcome (bearing in mind that an indenter that is too small may

lead to noise issue in measured data). The role of probing direction is also an important factor. In this thesis, the probing direction always followed the anterior-posterior axis, however this may not be possible particularly when this method is deployed for in vivo measurements.

Validity and potential changing for the assumptions of the boundary conditions

In Chapter 6, the predictive model was assessed using the reaction force profile obtained by simulating the probing procedure using histological based-models. In those cases, the prostatic slices were embedded into a 'box' (homogenous soft material) for simulating the interactions between the prostate and surrounding tissues (fat, connective tissue and muscles). However, the force profiles and the peak shapes were consistent with the simulated force feedback, outcome of the random models using for generating the training data-set as described in Chapter 5. As a result, the accuracy of the prediction for the nodule(s) existence shown a not significant influence by the diverse boundary conditions applied in the histological based- and random models.

In Chapter 7, the predictive model was assessed using experimental force profiles. The range of the force values and the peak shapes agreed with the simulated force feedback. The sensitivity and specificity of the predictive model were comparable or even higher than the diagnostic techniques such as DRE and MRI. Therefore, the assumptions of the boundary conditions applied in the prostate models for generating the training data-set might influence the force profiles such as the error between the simulated and experimental force feedback is reduced.

However, modelling the interactions between the prostate and surrounding tissues during *in-vivo* probing procedure is not a trivial task. Nevertheless, a comprise between the accuracy of the force feedback and the time-consuming of the FE simulations need to be

found. Therefore, for improving the accuracy of the predictive model more complex boundary conditions could be considered. The rigid boundary conditions and the using of the 'box' could be overcome by 'elastic boundary conditions' which can be implemented using the Robin scheme. This method allows modelling the surrounding tissue to a sequence of elastic springs with a rigidity α representative of the Young's modulus of the tissue [150].

Patient data-set

Although the patient data presented in this thesis consisted of 9 patients, rare among biomechanical study of prostate tissue, a larger dataset involving more patients would be useful. In particular, because of the nature of the clinical study from which the experimental measurements were obtained, most patients have an advanced stage of PCa, meaning that the cancerous nodule may have a higher elastic modulus and the size of the tumor nodules is often quite large. For patients with PCa at earlier stages, the predictive outcome could become worse. However, the results presented in Chapter 7 are still encouraging, since the sensitivity and specificity of the proposed method are higher than the current DRE and MRI procedures in clinical examination.

Appendix A.1. Identification Steps of PCa Nodules in Prostate Model (Chapters 5-7)

This appendix is designed to demonstrate the process of identifying the PCa nodules in prostate models based on the force profile from point-wise probing, using a probability approach. The whole identification process includes a number of steps, which are demonstrated as follows:

Step 0: Identify the peak in the force profile – the sharpness value, H/W, needs to be greater than 5;

Step 1: Identify the location of the peak of force profile along the left-right axis – it is considered to be the location of the identified PCa nodule;

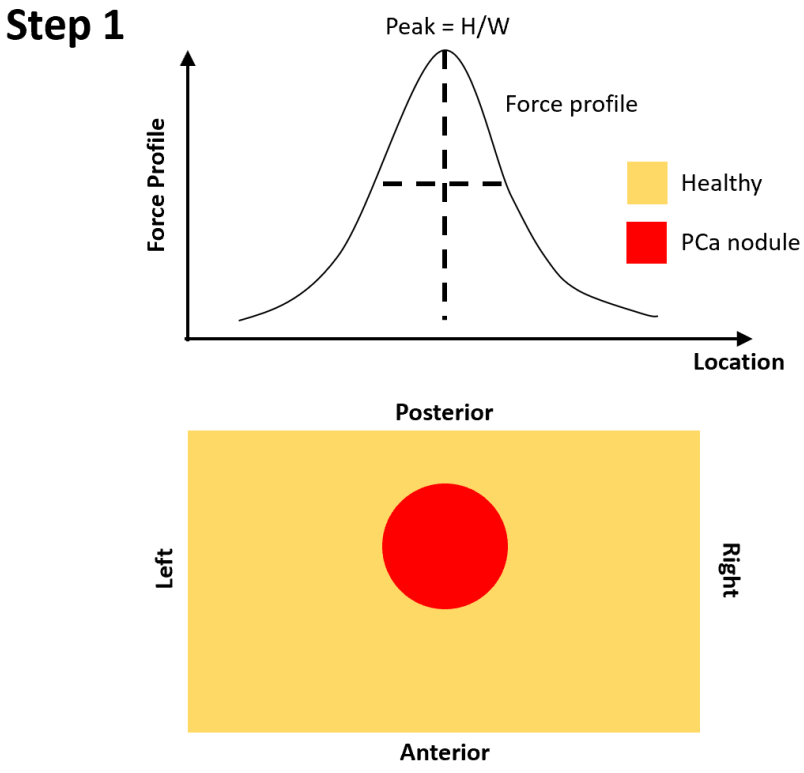

Fig. A.1-1. Step 1 – Identification of PCa nodule location along the left-right axis.

Step 2: Once the location of the PCa nodule is identified, the probability of the nodule existence is calculated, firstly, along the anterior-posterior axis, using the identified location at the posterior surface as the 'origin'. It should be noted that the probability along the anterior-posterior direction depends on both the PDFs of the nodule depth and size (see Appendix A.2.1).

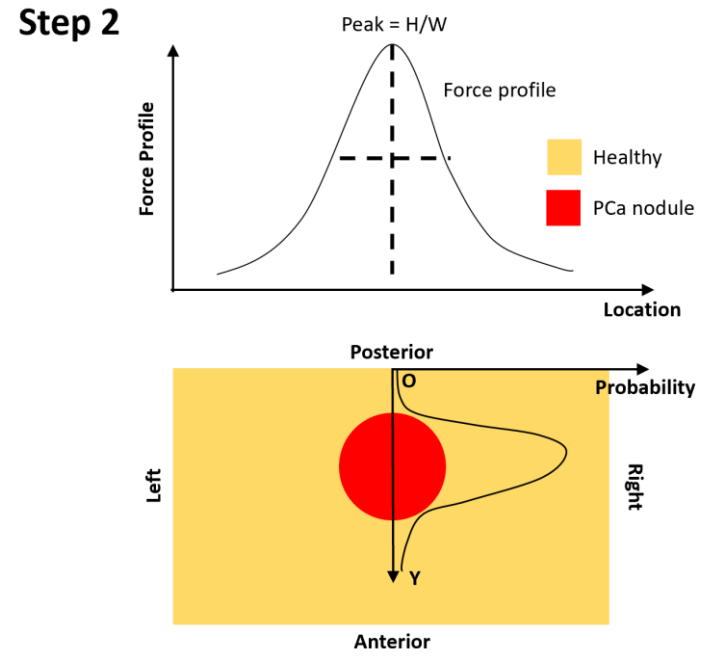

Fig. A.1-2. Step 2 – constructing the probability of PCa existence along the Y axis, using O as the origin.

Step 3: Along the anterior-posterior axis, the centre of the PCa nodule is identified using the median value of the probability distribution along the Y-axis.

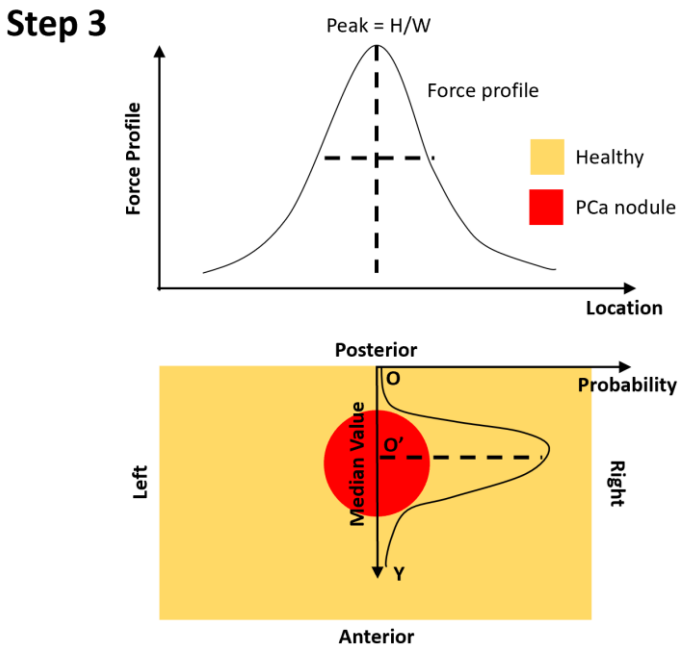

Fig. A.1-3. Step 3 – identification of the centre of depth of the PCa nodule.

Step 4: At the depth of the identified tumor centre, the probability of the nodule existence along the left-right axis is calculated, in a symmetrical fashion, using the O' as the origin. Note the probability along the left-right axis only depends on the PDF of the nodule size. (see Appendix A.2.2).

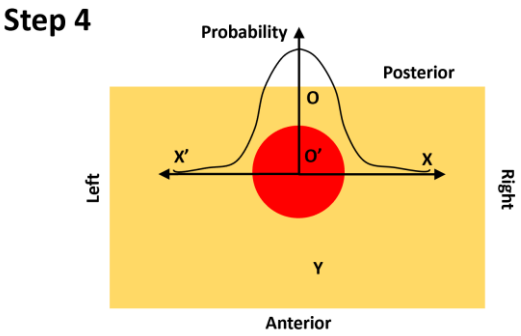

Fig. A.1-4. Step 4 – constructing the probability of PCa existence along the left-right axis, using O' as the origin, in a symmetrical fashion.

Step 5: if binary prediction, i.e. the outline of the PCa nodule, is needed, a probability threshold, as illustrated as a 'virtual plane' below, is adopted and the area along two major axes with probability values greater than the chosen threshold is believed to be the area of PCa nodule (i.e. the black circle projected onto the bottom plane).

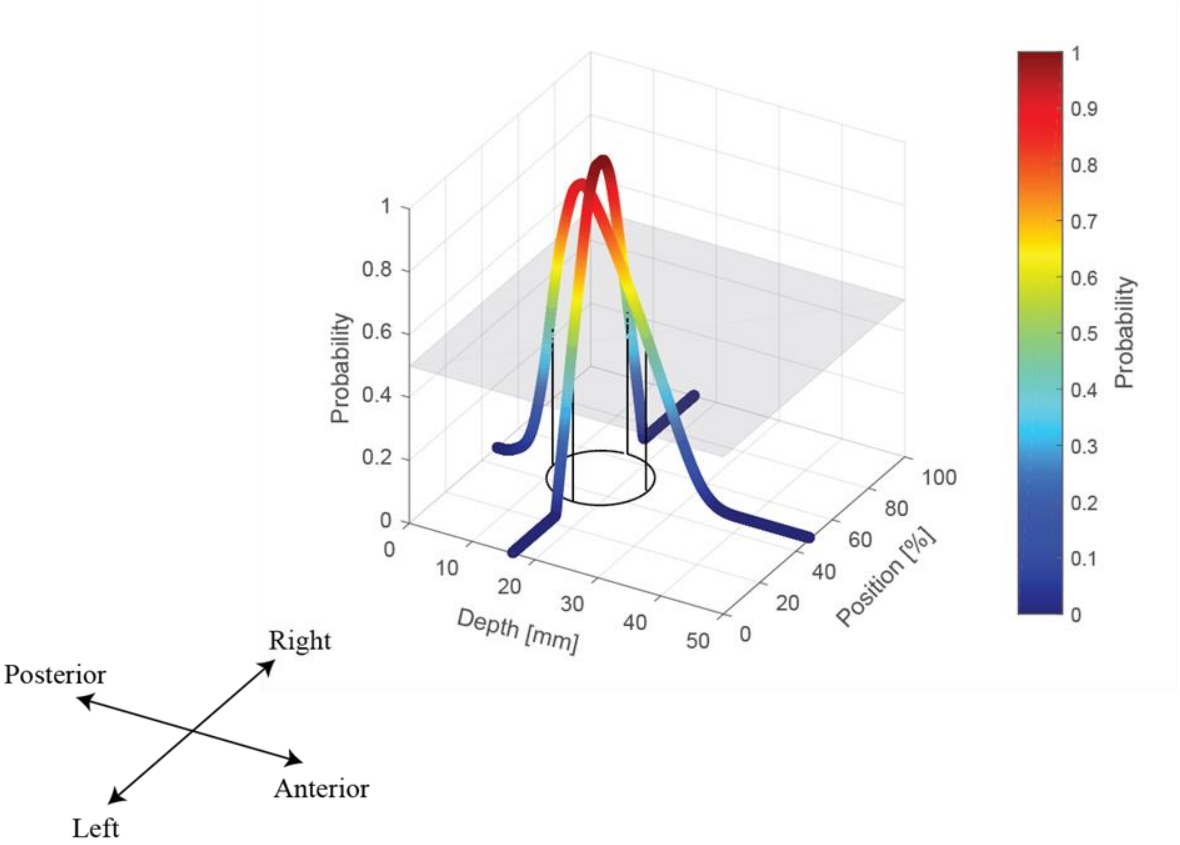

Fig. A.1-5. Step 5 – if necessary, binary identification of PCa nodule can be carried out using a probability threshold. |How to optimize the value of the probability threshold has been discussed in more details in Chapter 5 section 5.4. In this example the probability threshold was 0.5.

Appendix A.2. Framework to predict the probability of PCa existence along both the left-right and anterior-posterior axes

This section describes how the probabilities of the PCa nodule existence along both the left-right and anterior-posterior axes are derived. The probability is defined to be the likelihood of a given point in the prostate domain being a part of the PCa nodule. The following derivation follows a 1D simplification, using the coordinate systems defined in Appendix A.1, for both axes, respectively.

A.2.1. Probability along the anterior-posterior axis (Step 2 in Appendix A.1)

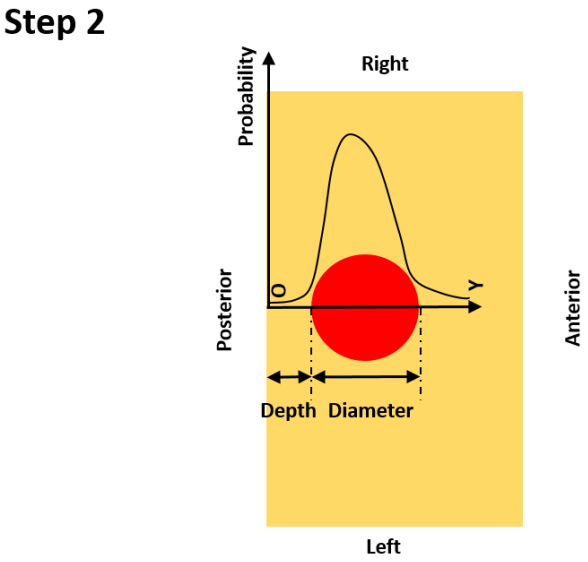

Fig. A.2-1. Schematic of the equivalent 1D problem for finding the probability along the Y-axis.

Finding the probability of the PCa nodule existence along the Y-axis, with the origin at the identified location on the posterior surface, becomes, effectively, a one-dimensional problem (Fig. B-1).

To maintain consistency and clarity through the explanation of the steps for solving the one-dimensional problem, the probability notation is adopted.

- Capital letters are used to denote random variables
- Realizations of a random variable are written in corresponding lower-case letters
- $f_X\ (x)$ - probability density function of (PDF) X
- $f_{X,Y}\ (x, y)$ – join probability density function of X and Y
- $f_{X|Y}\ (x|y)$ – conditional probability density function of X given Y
- $F_X\ (x)$ – cumulative density function (CDF) of X

Let define the nodule depth (d) and size (D) as two independent random variables X and Y, respectively, which can take non-negative real numbers. The question is now, what is the probability of a given location along the Y-axis of being cancerous? Mathematically, the solution could be the probability of any given non-negative real number $\boldsymbol{a}$ (constant) being no less than X and no greater than $X + Y$ or Z.

$$X \leq \boldsymbol{a} \leq X + Y = Z \tag{A.2-1}$$

Physically, this means the location of any given point falling in the red region along the Y-axis.

Let us draw the probability solution of this joint event

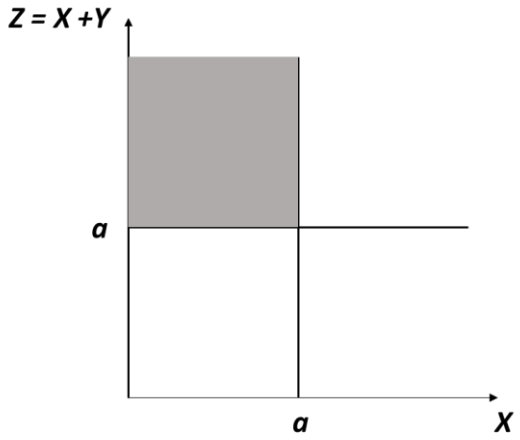

Fig. A.2-2. Probability solution of the joint event. The space from the vertical line (i.e. $X = \boldsymbol{a}$) represents the probability of the event $X \leq \boldsymbol{a}$. The space from the horizontal line ($Z = \boldsymbol{a}$) represents the probability of the event $a \leq Z$. The space in grey represents the probability of the joint event defined in equation A.2-1.

Therefore, the probability solution of the joint event, highlighted in grey in Fig. B-2, can be derived as

$$\Pr(X \leq \boldsymbol{a} \leq Z) = \Pr(X \leq \boldsymbol{a}) - \Pr(X \leq \boldsymbol{a}\ and\ Z \leq \boldsymbol{a}) \quad \text{(A.2-2)}$$

It should be noted that, the PDFs for the nodule depth, $f_X(x)$, and size, $f_Y(y)$, were calculated in Fig. 5-4. Therefore, the first term of equation A.2-3 is

$$\Pr(X \leq \boldsymbol{a}) = F_X(x) = \int_0^a f_X(x)dx \quad \text{(A.2-3)}$$

Moreover, we need to calculate the joint probability between *X* and *Z*, the second term of the equation A.2-3. The joint probability function between two continuous random variables is equal to

$$f_{X,Z}(x,z) = f_{Z|X}(z|x)f_X(x) = f_{X|Z}(x|z)f_Z(z) \quad \text{(A.2-4)}$$

where $f_{Z|X}(z|x)$ and $f_{X|Z}(x|z)$ are the conditional distributions of Z given $X = x$ and X given $Z = z$, respectively, and $f_X(x)$ and $f_Z(z)$ are the marginal distribution for X and Z, respectively.

However, it is later proved [see Proof 1 below] that the joint probability of $\Pr(X \leq \boldsymbol{a}\ and\ Z \leq \boldsymbol{a})$ takes, coincidentally due to the formulation of the Z, exactly the same form as $\Pr(Z \leq \boldsymbol{a})$. Therefore,

$$\Pr(X \leq \boldsymbol{a} \leq Z) = \Pr(X \leq \boldsymbol{a}) - \Pr(Z \leq \boldsymbol{a}) = \int_0^a f_X(x)dx - \int_0^a f_Z(z)dz \qquad \text{(A.2-5)}$$

For this, we will need the PDF of Z, $f_Z(z)$, which can be derived by the rule of the convolution among the PDFs of the nodule depth and size (already calculated in Fig. 5-4). The general formula for the distribution of the sum $Z = X + Y$ of two independent random variables with density functions $f_X(x)$ and $f_Y(y)$ is

$$f_Z(z) = \int_{-\infty}^{+\infty} f_X(z - y)\, f_Y(y)dy \qquad \text{(A.2-6)}$$

[Proof 1]

The joint probability, which is the $\Pr(X \leq \boldsymbol{a}\ and\ Z \leq \boldsymbol{a})$ as put earlier, is equal to the conditional distribution of $X \leq \boldsymbol{a}$ given $Z \leq \boldsymbol{a}$ multiplied by marginal dthe istribution of $Z \leq \boldsymbol{a}$. Note that the marginal CDF of Z is equal to

$$\Pr(Z \leq \boldsymbol{a}) = F_Z(z) = \int_0^a f_Z(z)dz \qquad \text{(A.2-7)}$$

On the other hand, the conditional distribution of $X \leq \boldsymbol{a}$ given $Z \leq \boldsymbol{a}$, in other words, the probability of $X \leq \boldsymbol{a}$ when $X + Y \leq \boldsymbol{a}$, is always 1. This is because, when $X + Y \leq \boldsymbol{a}$, X must be no greater than $\boldsymbol{a}$, if Y must take non-negative value. Therefore, the joint probability between X and Z takes the same form/value as that of Z.

A.2.2. Probability along the left-right axis (Step 4 in Appendix A.1)

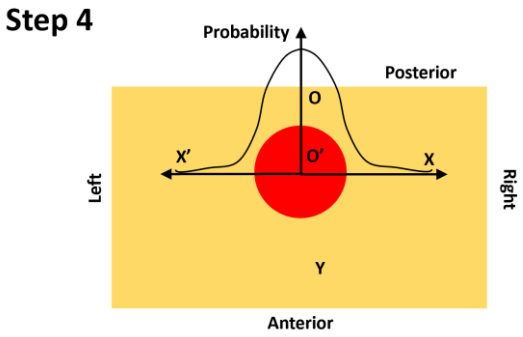

Fig. A.2-3. Step 4 – deriving the probability along the left-right axis.

It is evident that the probability along the left-right axis (X- and X'-axes as shown in Fig. B-3) is only dependent on the random variable *Y*, i.e. the diameter of the PCa nodule. Based on that, what is the probability of a given location along the X- or X'-axes of being cancerous? Mathematically, the solution could be the probability of any given non-negative real number $\boldsymbol{b}$ (constant) being no greater than *Y*/2 (i.e. radius of PCa nodule).

$$\boldsymbol{b} \leq Y/2 \tag{A.2-8}$$

Physically, this means the location of any given point falling in the red region along the X- and X'-axes.

The PDF of the nodule size shown in Fig..4-5, $f_Y(y)$, allows deriving the probability of the cancerous nodule existence along the left-right axis as

$$\Pr\left(\boldsymbol{b} \leq \frac{Y}{2}\right) = 1 - F_Y(y) = \int_b^{+\infty} f_Y(y)dy \tag{A.2-9}$$

Appendix B

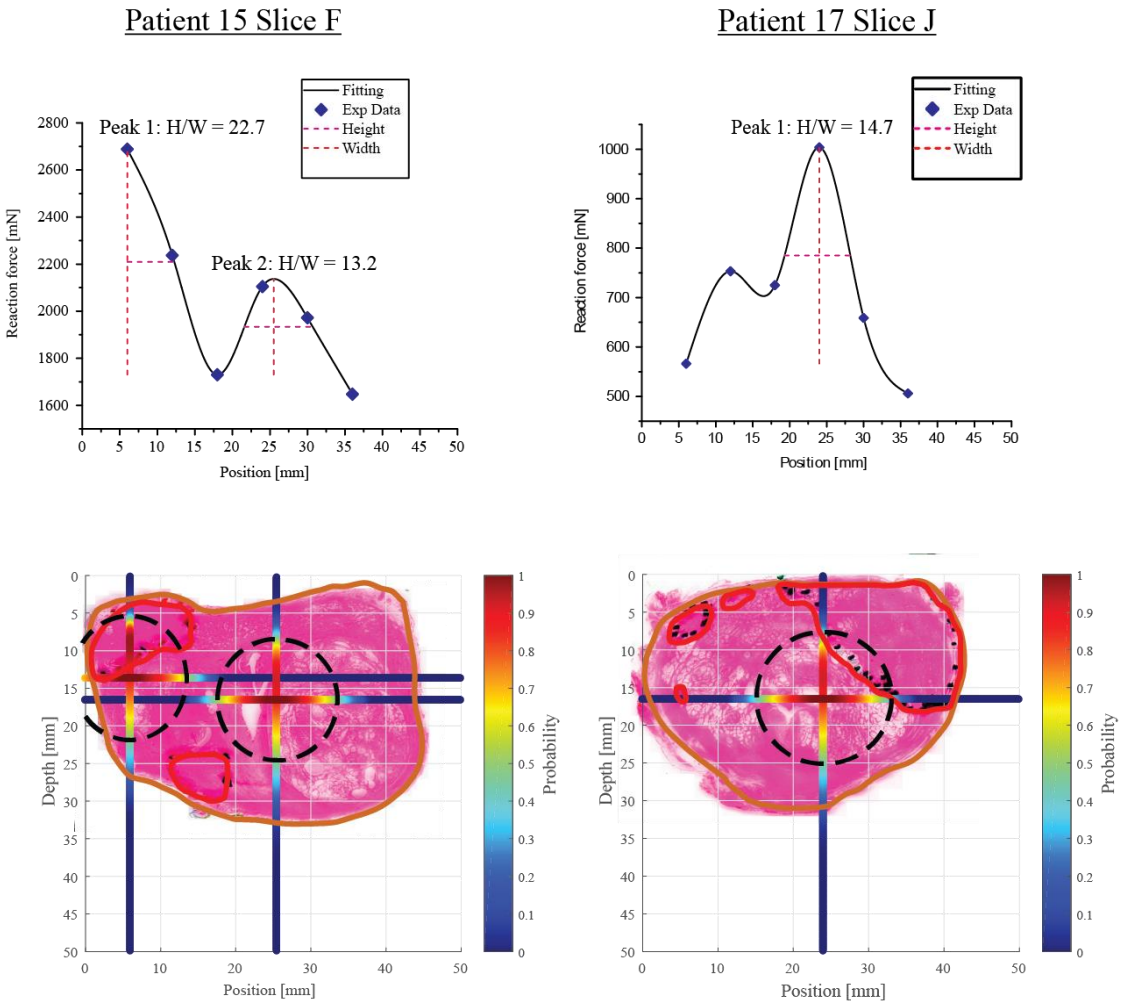

Fig. B-1. Results of prediction for Patient 15 slice F and Patient 17 slice J.

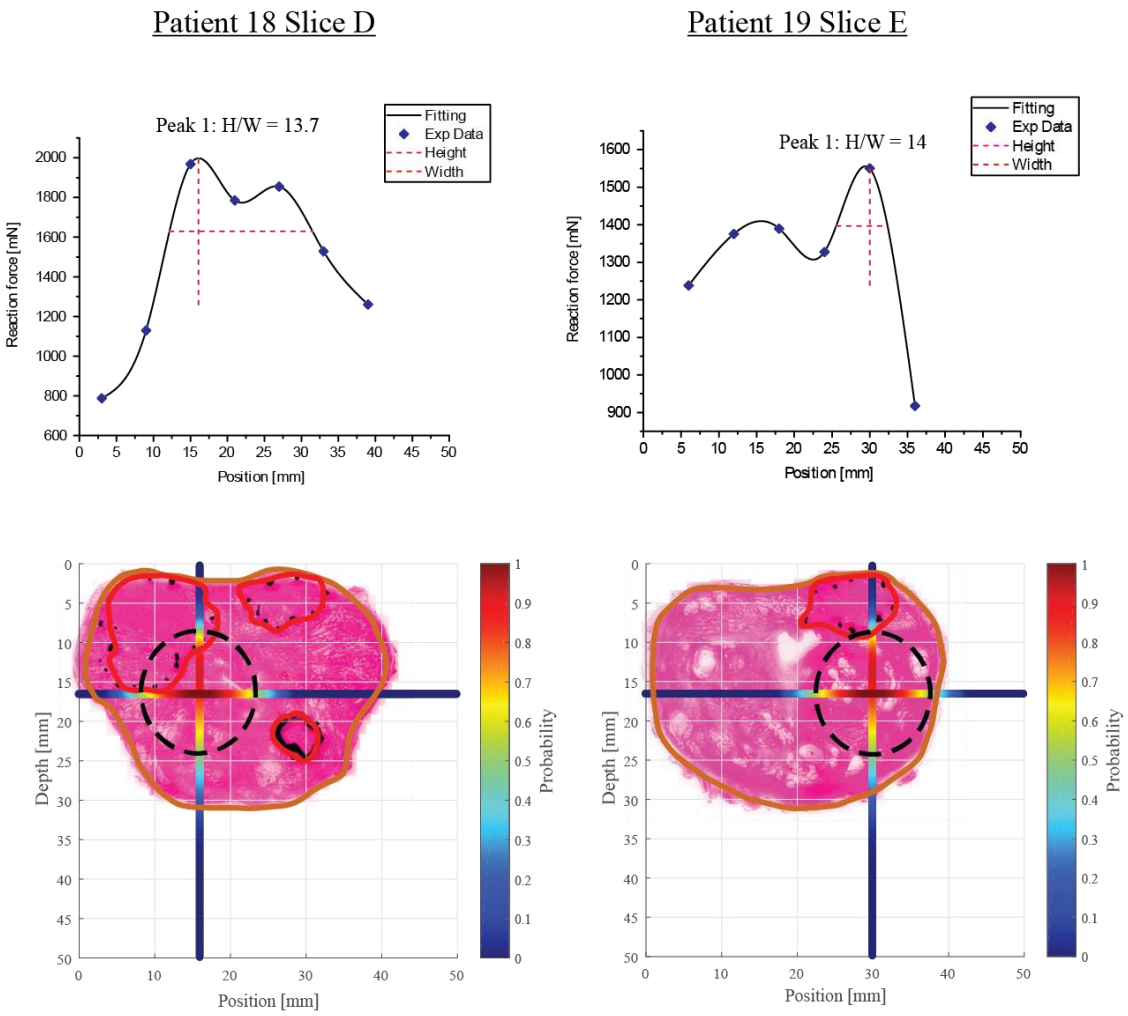

Fig. B-2. Results of prediction for Patient 18 slice D and Patient 19 slice E.

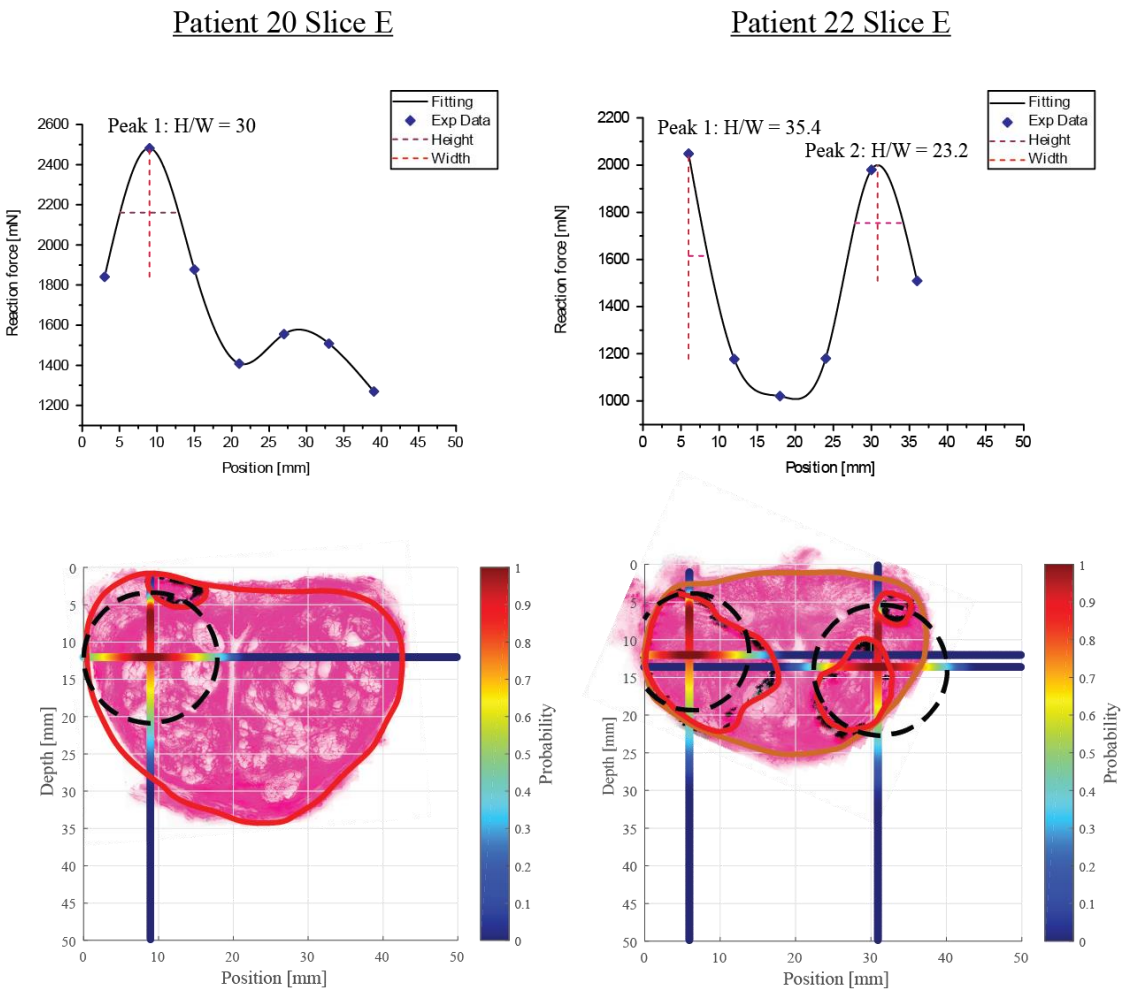

Fig. B-3. Results of the prediction for Patient 20 slice E and Patient 22 slice E.

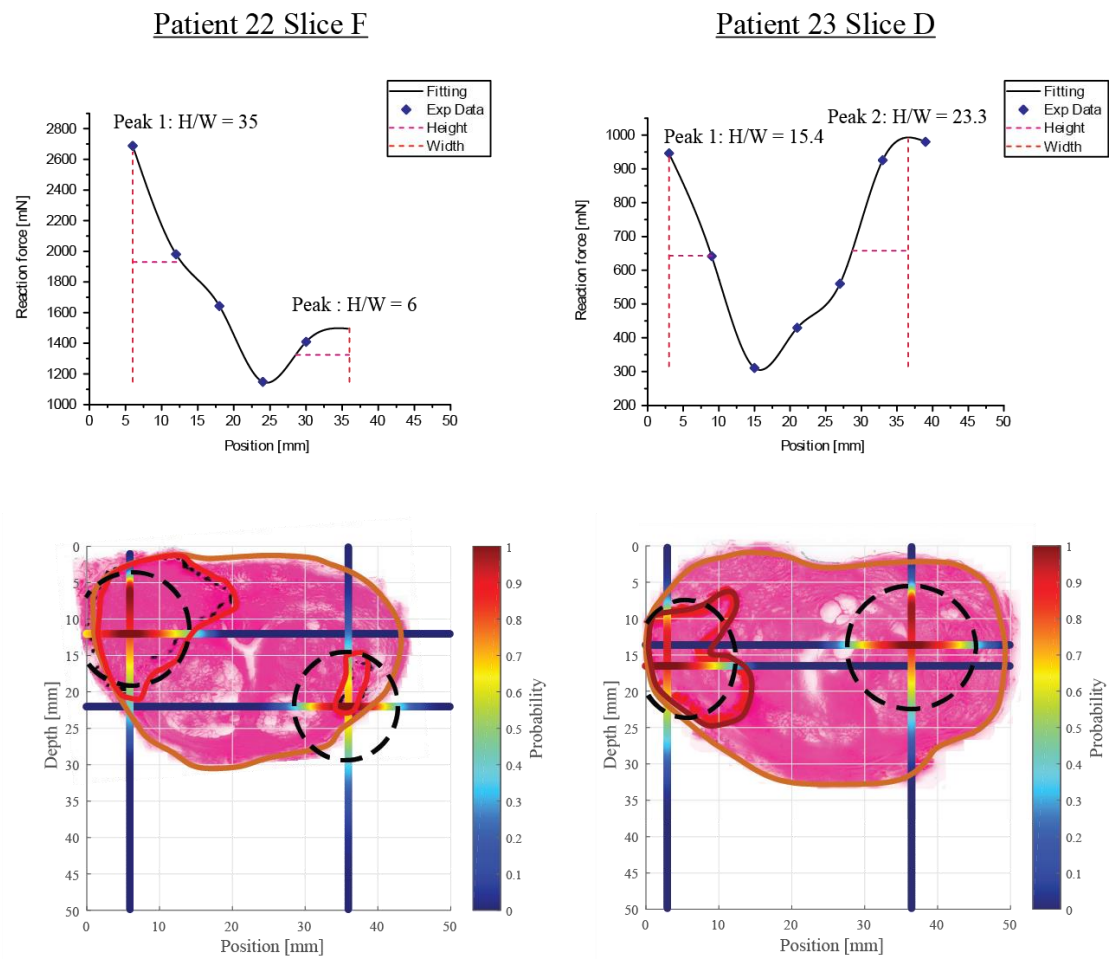

Fig. B-4. Results of the prediction for Patient 22 slice F and Patient 23 slice D.

Bibliography

[1] P. Kohl, D. Noble, R. L. Winslow, and P. J. Hunter, "Computational Modelling of Biological Systems : Tools and Visions Source," *R. Soc.*, vol. 358, no. 1766, pp. 579–610, 2016.

[2] V. Thondapu, C. V. Bourantas, N. Foin, I. K. Jang, P. W. Serruys, and P. Barlis, "Basic science for the clinician: Biomechanical stress in coronary atherosclerosis: Emerging insights from computational modelling," *Eur. Heart J.*, vol. 38, no. 2, pp. 81–92, 2017.

[3] Y. Chen, S. Zhou, and Q. Li, "Microstructure design of biodegradable scaffold and its effect on tissue regeneration," *Biomaterials*, vol. 32, no. 22, pp. 5003–5014, 2011.

[4] N. Famaey and J. Vander Sloten, "Soft tissue modelling for applications in virtual surgery and surgical robotics," *Comput. Methods Biomech. Biomed. Engin.*, vol. 11, no. 4, pp. 351–366, 2008.

[5] F. Migliavacca, L. Petrini, V. Montanari, I. Quagliana, F. Auricchio, and G. Dubini, "A predictive study of the mechanical behaviour of coronary stents by computer modelling," *Med. Eng. Phys.*, vol. 27, no. 1, pp. 13–18, 2005.

[6] D. W. Good, G. D. Stewart, S. Hammer, P. Scanlan, W. Shu, S. Phipps, R. Reuben, and A. S. McNeill, "Elasticity as a biomarker for prostate cancer: A systematic review," *BJU Int.*, vol. 113, no. 4, pp. 523–534, 2014.

[7] V. Parimi, R. Goyal, K. Poropatich, and X. J. Yang, "Neuroendocrine differentiation of prostate cancer: a review," *Am J Clin Exp Urol*, vol. 2, no. 4, pp. 273–285, 2014.

[8] J. P. Silletti, G. J. Gordon, R. Bueno, M. Jaklitsch, and K. R. Loughlin, "Prostate Biopsy: Past, Present, and Future," *Urology*, vol. 69, no. 3, pp. 413–416, 2007.

[9] C. B. Bozeman, B. S. Carver, G. Caldito, D. D. Venable, and J. A. Eastham, "Prostate cancer in patients with an abnormal digital rectal examination and serum prostate-specific antigen less than 4.0 ng/mL," *Urology*, vol. 66, no. 4, pp. 803–807, 2005.

[10] G. D. Friedman, R. A. Hiatt, C. P. Quesenberry, and J. V. Selby, "Case-control study of screening for prostatic cancer by digital rectal examinations," *Lancet*, vol. 337, no. 8756, pp. 1526–1529, 1991.

[11] S. A. Bigler, R. E. Deering, and M. K. Brawer, "Comparison of microscopic vascularity in benign and malignant prostate tissue," *Hum. Pathol.*, vol. 24, no. 2, pp. 220–226, 1993.

[12] D. S. Smith, W. J. Catalona, and J. D. Herschman, "Longitudinal Screening for Prostate Cancer With Prostate-Specific Antigen," *J. Adv. Pract. Oncol.*, vol. 276, no. 16, pp. 1309–1315, 1996.

[13] C. Mettlin, F. Lee, and J. Drago, "Findings on the detection of early prostate cancer in 2425 men," *Cancer*, vol. 67, no. 12, pp. 2949–2958, 1990.

[14] J. Nakashima, A. Tanimoto, Y. Imai, M. Mukai, Y. Horiguchi, K. Nakagawa, M.

Oya, T. Ohigashi, K. Marumo, and M. Murai, “Endorectal MRI for prediction of tumor site, tumor size, and local extension of prostate cancer,” *Urology*, vol. 64, no. 1, pp. 101–105, 2004.

[15] B. S. Garra, “Imaging and estimation of tissue elasticity by ultrasound,” *Ultrasound Q.*, vol. 23, no. 4, pp. 255–268, 2007.

[16] J. M. Correas, A. M. Tissier, A. Khairoune, G. Khoury, D. Eiss, and O. Hélénon, “Ultrasound elastography of the prostate: State of the art,” *Diagn. Interv. Imaging*, vol. 94, no. 5, pp. 551–560, 2013.

[17] W. F. Dähnert, U. M. Hamper, J. C. Eggleston, P. C. Walsh, and R. C. Sanders, “Prostatic evaluation by transrectal sonography with histopathologic correlation: the echopenic appearance of early carcinoma,” *Radiology*, vol. 158, no. 1, pp. 97–102, 1986.

[18] C. Mosquera-Lopez, S. Agaian, A. Velez-Hoyos, and I. Thompson, “Computer-Aided Prostate Cancer Diagnosis from Digitized Histopathology: A Review on Texture-Based Systems,” *IEEE Rev. Biomed. Eng.*, vol. 8, pp. 98–113, 2015.

[19] S. J. Hammer, D. W. Good, P. Scanlan, J. Palacio-Torralba, S. Phipps, G. D. Stewart, W. Shu, Y. Chen, S. A. McNeill, and R. L. Reuben, “Quantitative mechanical assessment of the whole prostate gland ex vivo using dynamic instrumented palpation,” *Proc. Inst. Mech. Eng. Part H J. Eng. Med.*, vol. 231, no. 12, pp. 1081–1100, 2017.

[20] J. Palacio-Torralba, E. Jiménez Aguilar, D. W. Good, S. J. Hammer, S. A. McNeill, G. D. Stewart, R. L. Reuben, and Y. Chen, “Patient specific modeling of palpation-based prostate cancer diagnosis: effects of pelvic cavity anatomy and intrabladder pressure,” *Int. j. numer. method. biomed. eng.*, vol. 32(1), p. e02734, 2015.

[21] Y. Kim, B. Ahn, J. W. Lee, K. H. Rha, and J. Kim, “Local property characterization of prostate glands using inhomogeneous modeling based on tumor volume and location analysis,” *Med. Biol. Eng. Comput.*, vol. 51, no. 1–2, pp. 197–205, 2013.

[22] M. A. Meyers, P.-Y. Chen, A. Y.-M. Lin, and Y. Seki, “Biological materials: Structure and mechanical properties,” *Prog. Mater. Sci.*, vol. 53, no. 1, pp. 1–206, 2008.

[23] N. Cho, W. K. Moon, H. Y. Kim, J. M. Chang, S. H. Park, and C. Y. Lyou, “Sonoelastographic strain index for differentiation of benign and malignant nonpalpable breast masses,” *J. Ultrasound Med.*, vol. 29, no. 1, pp. 1–7, 2010.

[24] L. C. H. Leong, L. S. J. Sim, Y. S. Lee, F. C. Ng, C. M. Wan, S. M. C. Fook-Chong, A. R. Jara-Lazaro, and P. H. Tan, “A prospective study to compare the diagnostic performance of breast elastography versus conventional breast ultrasound,” *Clin. Radiol.*, vol. 65, no. 11, pp. 887–894, 2010.

[25] A. Itoh, E. Ueno, E. Tohno, H. Kamma, H. Takahashi, T. Shiina, M. Yamakawa, and T. Matsumura, “Breast Disease: Clinical Application of US Elastography for Diagnosis,” *Radiology*, vol. 239, no. 2, pp. 341–350, 2006.

[26] W. K. Moon, C. S. Huang, W. C. Shen, E. Takada, R. F. Chang, J. Joe, M. Nakajima, and M. Kobayashi, “Analysis of Elastographic and B-mode Features at Sonoelastography for Breast Tumor Classification,” *Ultrasound Med. Biol.*, vol.

35, no. 11, pp. 1794–1802, 2009.

[27] J. Weickenmeier, R. de Rooij, S. Budday, P. Steinmann, T. C. Ovaert, and E. Kuhl, “Brain stiffness increases with myelin content,” *Acta Biomater.*, vol. 42, pp. 265–272, 2016.

[28] D. Chauvet, M. Imbault, L. Capelle, C. Demene, M. Mossad, C. Karachi, A.-L. Boch, J.-L. Gennisson, and M. Tanter, “In Vivo Measurement of Brain Tumor Elasticity Using Intraoperative Shear Wave Elastography,” *Ultraschall Med*, pp. 1–8, 2015.

[29] W.-C. Yeh, P.-C. Li, Y.-M. Jeng, H.-C. Hsu, P.-L. Kuo, M.-L. Li, P. M. Yang, and P. H. Lee, “Elastic Moduls Measurerments of Human Liver and Correlation With Pathology,” *Medicine (Baltimore).*, vol. 28, no. 4, pp. 467–474, 2002.

[30] M. Ziol, A. Handra-Luca, A. Kettaneh, C. Christidis, F. Mal, F. Kazemi, V. de Ledinghen, P. Marcellin, D. Dhumeaux, J.-C. Trinchet, and M. Beaugrand, “Noninvasive Assessment of Liver Fibrosis by Measurement of Stiffness in Patients With Chronic Hepatitis,” *Media Int. Aust.*, vol. 41, no. 1, pp. 48–54, 2005.

[31] S. C. Millasseau, R. P. Kelly, J. M. Ritter, and P. J. Chowienczyk, “Determination of age-related increases in large artery stiffness by digital pulse contour analysis,” *Clin. Sci.*, vol. 103, pp. 371–377, 2002.

[32] T. Kawasaki, C. H. I. Yagi, T. Asakawa, and T. Hirai, “Non-invasive assessment of the age related changes in stiffness of major branches of the human arteries,” *Cardiovasc. Res.*, vol. 21, pp. 678–687, 1987.

[33] T. Wada, K. Kodaira, K. Fujishiro, K. Maie, E. Tsukiyama, T. Fukumoto, T. Uchida, and S. Yamazaki, “Correlation of ultrasound-measured common carotid artery stiffness with pathological findings,” *Arterioscler. Thromb. Vasc. Biol.*, vol. 14, no. 3, pp. 479–482, 1994.

[34] J. R. Basford, T. R. Jenkyn, K. N. An, R. L. Ehman, G. Heers, and K. R. Kaufman, “Evaluation of healthy and diseased muscle with magnetic resonance elastography,” *Arch. Phys. Med. Rehabil.*, vol. 83, no. 11, pp. 1530–1536, 2002.

[35] S. F. Bensamoun, L. Robert, G. E. Leclerc, L. Debernard, and F. Charleux, “Stiffness imaging of the kidney and adjacent abdominal tissues measured simultaneously using magnetic resonance elastography,” *Clin. Imaging*, vol. 35, no. 4, pp. 284–287, 2011.

[36] S. Phipps, T. H. J. Yang, F. K. Habib, R. L. Reuben, and S. A. McNeill, “Measurement of the mechanical characteristics of benign prostatic tissue: A Novel method for assessing benign prostatic disease,” *Urology*, vol. 65, no. 5, pp. 1024–1028, 2005.

[37] A. B. Galosi, R. Montironi, A. Fabiani, V. Lacetera, G. Gallé, and G. Muzzonigro, “Cystic Lesions of the Prostate Gland: An Ultrasound Classification With Pathological Correlation,” *J. Urol.*, vol. 181, no. 2, pp. 647–657, 2009.

[38] J. A. Tuxhorn, G. E. Ayala, M. J. Smith, V. C. Smith, T. D. Dang, and D. R. Rowley, “Reactive stroma in human prostate cancer: Induction of myofibroblast phenotype and extracellular matrix remodeling,” *Clin. Cancer Res.*, vol. 8, no. 9, pp. 2912–2923, 2002.

[39] S. Phipps, T. H. J. Yang, F. K. Habib, R. L. Reuben, and S. A. McNeill, "Measurement of tissue mechanical characteristics to distinguish between benign and malignant prostatic disease," *Urology*, vol. 66, no. 2, pp. 447–450, 2005.

[40] Y. Zhang, S. Nojima, H. Nakayama, Y. Jin, and H. Enza, "Characteristics of normal stromal components and their correlation with cancer occurrence in human prostate," *Oncol. Rep.*, vol. 10, no. 1, pp. 207–211, 2003.

[41] A. M. De Marzo, V. L. Marchi, J. I. Epstein, and W. G. Nelson, "Proliferative inflammatory atrophy of the prostate: Implications for prostatic carcinogenesis," *Am. J. Pathol.*, vol. 155, no. 6, pp. 1985–1992, 1999.

[42] D. F. Gleason, "Histologic grading of prostate cancer: A perspective," *Hum. Pathol.*, vol. 23, no. 3, pp. 273–279, 1992.

[43] J. Palacio-Torralba, D. W. Good, S. A. McNeill, R. L. Reuben, and Y. Chen, "Histology-based homogenization analysis of soft tissue: Application to prostate cancer," *J. R. Soc. Interface*, vol. 14, no. 129, 2017.

[44] A. Tabesh, M. Teverovskiy, H. Pang, V. P. Kumar, D. Verbel, A. Kotsianti, and O. Saidi, "Multifeature Prostate Cancer Diagnosis and Gleason Grading of Histological Images," *IEEE Trans. Med. Imaging*, vol. 26, no. 10, pp. 1366–1378, 2007.

[45] J. M. Schwartz, M. Denninger, D. Rancourt, C. Moisan, and D. Laurendeau, "Modelling liver tissue properties using a non-linear visco-elastic model for surgery simulation," *Med. Image Anal.*, vol. 9, no. 2, pp. 103–112, 2005.

[46] L. Baggi, I. Cappelloni, M. Di Girolamo, F. Maceri, and G. Vairo, "The influence of implant diameter and length on stress distribution of osseointegrated implants related to crestal bone geometry: A three-dimensional finite element analysis," *J. Prosthet. Dent.*, vol. 100, no. 6, pp. 422–431, 2008.

[47] R. Langer and D. A. Tirrell, "Designing materials for biology and medicine," *Nature*, vol. 428, no. 6982, pp. 487–492, 2004.

[48] P. Scanlan, S. J. Hammer, D. W. Good, S. Phipps, G. D. Stewart, S. A. McNeill, W. Shu, and R. L. Reuben, "Development of a novel actuator for the dynamic palpation of soft tissue for use in the assessment of prostate tissue quality," *Sensors Actuators, A Phys.*, vol. 232, pp. 310–318, 2015.

[49] Y. C. Fung, *Biomechanics: Mechanical Properties of Living Tissues*. 1993.

[50] D. R. Veronda and R. A. Westmann, "Mechanical characterization of skin-Finite deformations," *J. Biomech.*, vol. 3, no. 1, 1970.

[51] B. J. D. Humphrey, "Continuum biomechanics soft biological tissues," *R. Soc.*, vol. 459, no. 2029, pp. 3–46, 2008.

[52] A. Ali, M. Hosseini, and M. M. Sahari, "A Review of Constitutive Models for Rubber-Like Materials," *Am. J. Eng. Appl. Sci. 3*, vol. 3, no. 1, pp. 232–239, 2010.

[53] A. Sadeghi Naini, R. V. Patel, and A. Samani, "Measurement of lung hyperelastic properties using inverse finite element approach," *IEEE Trans. Biomed. Eng.*, vol. 58, no. 10 PART 1, pp. 2852–2859, 2011.

[54] L. R. G. Treloar, “The elasticity of a network of long-chain molecules-II,” *Trans. Faraday Soc.*, vol. 39, pp. 241–246, 1943.

[55] M. Mooney, “A theory of large elastic deformation,” *J. Appl. Phys.*, vol. 11, no. 9, pp. 582–592, 1940.

[56] R. S. Rivlin, “Large elastic deformations of isotropic materials IV. further developments of the general theory,” *Philos. Trans. R. Soc.*, vol. 241, no. 835, pp. 379–397, 1948.

[57] R. W. Ogden, “Large Deformation Isotropic Elasticity - On the Correlation of Theory and Experiment for Incompressible Rubberlike Solids,” *Proc. R. Soc. Lond. A*, vol. 326, pp. 565–584, 1972.

[58] J. S. Bergström and M. C. Boyce, “Constitutive modeling of the time-dependent and cyclic loading of elastomers and application to soft biological tissues,” *Mech. Mater.*, vol. 33, no. 9, pp. 523–530, 2001.

[59] B. F. Millard, “Topics In Finite Elasticity: Hyperelasticity of rubber, elastomers, and biological tissues - with examples,” *Appl. Mech. Rev.*, vol. 40, no. 12, pp. 1699–1734, 1987.

[60] M. C. Boyce and E. M. Arruda, “Constitutive Models of Rubber Elasticity: A Review,” *Rubber Chem. Technol.*, vol. 73, no. 3, pp. 504–523, 2000.

[61] T. Beda, “Modeling Hyperelastic Behavior of Rubber: A Novel Invariant-Based and a Review of Constitutive Models,” *J. Polym. Sci. Part B Polym. Phys.*, vol. 45, pp. 1713–1732, 2007.

[62] W. C. Carson, G. J. Gerling, T. L. Krupski, C. G. Kowalik, J. C. Harper, and C. A. Moskaluk, “Material characterization of ex vivo prostate tissue via spherical indentation in the clinic,” *Med. Eng. Phys.*, vol. 33, no. 3, pp. 302–309, 2011.

[63] B. M. Ahn, J. Kim, L. Ian, K. H. Rha, and H. J. Kim, “Mechanical property characterization of prostate cancer using a minimally motorized indenter in an ex vivo indentation experiment,” *Urology*, vol. 76, no. 4, pp. 1007–1011, 2010.

[64] T. A. Krouskop, T. M. Wheeler, F. Kallel, B. S. Garra, and T. Hall, “Elastic moduli of breast and prostate tissue under compression,” *Ultrason. Imaging*, vol. 20, no. 4, pp. 260–274, 1998.

[65] K. Hoyt, B. Castaneda, M. Zhang, P. Nigwekar, P. A. di Sant’Agnese, J. V. Joseph, J. Strang, D. J. Rubensd, and K. J. Parkera, “Tissue elasticity properties as biomarkers for prostate cancer,” *Cancer Biomarkers*, vol. 4, no. 4–5, pp. 213–225, 2008.

[66] M. Zhang, P. Nigwekar, B. Castaneda, K. Hoyt, J. V. Joseph, A. di Sant’Agnese, E. M. Messing, J. G. Strang, D. J. Rubens, and K. J. Parker, “Quantitative Characterization of Viscoelastic Properties of Human Prostate Correlated with Histology,” *Ultrasound Med. Biol.*, vol. 34, no. 7, pp. 1033–1042, 2008.

[67] J. H. Fowke, S. S. Motley, M. S. Cookson, R. Concepcion, S. S. Chang, M. L. Wills, and J. A. Smith, “The association between body size, prostate volume and prostate-specific antigen,” *Prostate Cancer Prostatic Dis.*, vol. 10, no. 2, pp. 137–142, 2007.

[68] S. Bouyé, E. Potiron, P. Puech, X. Leroy, L. Lemaitre, and A. Villers, “Transition zone and anterior stromal prostate cancers: Zone of origin and intraprostatic patterns of spread at histopathology,” *Prostate*, vol. 69, no. 1, pp. 105–113, 2009.

[69] C. William J, S. Deborah S, R. Timothy L, D. Kathy M, C. Douglas E, Y. Jerry J J, J. Petros A, and G. Andriole L., “Measurement of prostate-specific antigen in serum as a screening test for prostate cancer,” *N Engl J Med*, vol. 324, no. 17, pp. 1156–1161, 1991.

[70] J. Oesterling, S. Jacobsen, C. Chute, H. Guess, and C. Girman, “Serum prostate-specific antigen in a community-based population of healthy men. Establishment of age-specific reference ranges,” *Jama*, vol. 270, 1993.

[71] A. W. Partin, W. J. Catalona, P. C. Southwick, E. N. P. Subong, G. H. Gasior, and D. W. Chan, “Analysis of percent free prostate-specific antigen (PSA) for prostate cancer detection: Influence of total PSA, prostate volume, and age,” *Urology*, vol. 48, no. 6 SUPPL., pp. 55–61, 1996.

[72] M. De Rooij, E. H. J. Hamoen, J. J. Fütterer, J. O. Barentsz, and M. M. Rovers, “Accuracy of multiparametric MRI for prostate cancer detection: A meta-analysis,” *Am. J. Roentgenol.*, vol. 202, no. 2, pp. 343–351, 2014.

[73] P. De Visschere, W. Oosterlinck, G. De Meerleer, and G. Villeirs, “Clinical and Imaging Tools in the Early Diagnosis of Prostate Cancer,” *Jbr-Brt*, vol. 93, no. 2, pp. 62–70, 2010.

[74] J. Zhang, H. Jing, X. Han, Z. Huang, Z. Cao, and Q. Liu, “Diffusion-Weighted Imaging of Prostate Cancer on 3T MR. Relationship between Apparent Diffusion Coefficient Values and Ki-67 Expression,” *Acad. Radiol.*, vol. 20, no. 12, pp. 1535–1541, 2013.

[75] J. Iwazawa, T. Mitani, S. Sassa, and S. Ohue, “Prostate cancer detection with MRI: Is dynamic contrast-enhanced imaging necessary in addition to diffusion-weighted imaging?,” *Diagnostic Interv. Radiol.*, vol. 17, no. 3, pp. 243–248, 2011.

[76] G. B. Chavhan, P. S. Babyn, B. Thomas, M. M. Shroff, and E. M. Haacke, “Principles, techniques, and applications of T2*-based MR imaging and its special applications.,” *Radiographics*, vol. 29, no. 5, pp. 1433–49, 2009.

[77] Y. K. Mariappan, K. J. Glaser, and R. L. Ehman, “Magnetic Resonance Elastography: A review,” *Clin Anat.*, vol. 23, no. 5, pp. 497–511, 2010.

[78] L. E. Quint, J. S. Van Erp, P. H. Bland, S. H. Mandell, E. A. Del Buono, H. B. Grossman, G. M. Glazer, and P. W. Gikas, “Carcinoma of the prostate: MR images obtained with body coils do not accurately reflect tumor volume,” *Clin. Oncol.*, vol. 156, pp. 511–516, 1991.

[79] S. Li, M. Chen, W. Wang, W. Zhao, J. Wang, X. Zhao, and C. Zhou, “A feasibility study of MR elastography in the diagnosis of prostate cancer at 3.0T,” *Acta radiol.*, vol. 52, no. 3, pp. 354–358, 2011.

[80] E. C. Ehman, P. J. Rossman, S. A. Kruse, A. V. Sahakian, and K. J. Glaser, “Vibration safety limits for magnetic resonance elastography,” *Phys Med Biol 2008*, vol. 53, pp. 925–935, 2008.

[81] A. Postema, M. Mischi, J. de la Rosette, and H. Wijkstra, “Multiparametric

ultrasound in the detection of prostate cancer: a systematic review," *World J. Urol.*, vol. 33, no. 11, pp. 1651–1659, 2015.

[82] M. D. Rifkin, W Dähnert, and A. B. Kurtz, "State of the art: endorectal sonography of the prostate gland," *Am. J. Roentgenol.*, 1990.

[83] A. Ozturk, J. R. Grajo, M. Dhyani, B. W. Anthony, and A. E. Samir, "Principles of ultrasound elastography," *Abdom. Radiol.*, vol. 43, no. 4, pp. 773–785, 2018.

[84] D. L. Cochlin, R. H. Ganatra, and D. F. R. Griffiths, "Elastography in the detection of prostatic cancer," *Clin. Radiol.*, vol. 57, no. 11, pp. 1014–1020, 2002.

[85] O. M. Aboumarzouk, S. Ogston, Z. Huang, A. Evans, A. Melzer, J. Stolzenberg, and G. Nabi, "Diagnostic accuracy of transrectal elastosonography (TRES) imaging for the review and meta-analysis," *Br. J. Urol. Int.*, vol. 110, no. 10, pp. 1414–1423, 2012.

[86] J. M. Correas, E. Drakonakis, A. M. Isidori, O. Hélénon, C. Pozza, V. Cantisani, N. Di Leo, F. Maghella, A. Rubini, F. M. Drudi, and F. D'Ambrosio, "Reprint of Update on ultrasound elastography: Miscellanea. Prostate, testicle, musculo-skeletal," *Eur. J. Radiol.*, vol. 83, no. 3, pp. 442–449, 2014.

[87] Z. Wu, L. S. Taylor, D. J. Rubens, and K. J. Parker, "Sonoelastographic imaging of interference patterns for estimation of the shear velocity of homogeneous biomaterials," *Phys. Med. Biol.*, vol. 49, no. 6, pp. 911–922, 2004.

[88] K. Hoyt, K. J. Parker, and D. J. Rubens, "Real-Time Shear Velocity Imaging Using Sonoelastographic Techniques," *Ultrasound Med. Biol.*, vol. 33, no. 7, pp. 1086–1097, 2007.

[89] K. J. Parker, D. Fu, S. M. Graceswki, F. Yeung, and S. F. Levinson, "Vibration sonoelastography and the detectability of lesions," *Ultrasound Med. Biol.*, vol. 24, no. 9, pp. 1437–1447, 1998.

[90] V. Jalkanen, B. M. Andersson, A. Bergh, B. Ljungberg, and O. A. Lindahl, "Resonance sensor measurements of stiffness variations in prostate tissue in vitro - A weighted tissue proportion model," *Physiol. Meas.*, vol. 27, no. 12, 2006.

[91] A. O. Sartor, H. Hricak, T. M. Wheeler, J. Coleman, D. F. Penson, P. R. Carroll, M. A. Rubin, and P. T. Scardino, "Evaluating Localized Prostate Cancer and Identifying Candidates for Focal Therapy," *Urology*, vol. 72, no. 6 SUPPL., pp. S12–S24, 2008.

[92] H. Tadayyon, A. Lasso, A. Kaushal, P. Guion, and G. Fichtinger, "Target motion tracking in MRI-guided transrectal robotic prostate biopsy," *IEEE Trans. Biomed. Eng.*, vol. 58, no. 11, pp. 3135–3142, 2011.

[93] L. Pallwein, M. Mitterberger, P. Struve, W. Horninger, F. Aigner, G. Bartsch, J. Gradl, M. Schurich, F. Pedross, and F. Frauscher, "Comparison of sonoelastography guided biopsy with systematic biopsy: Impact on prostate cancer detection," *Eur. Radiol.*, vol. 17, no. 9, pp. 2278–2285, 2007.

[94] J. A. Spencer, A. A. Alexander, L. Gomella, T. Matteucci, and B. B. Goldberg, "Clinical and US findings in prostate cancer: patients with normal prostate-specific antigen levels," *Radiology*, vol. 189, no. 2, pp. 389–393, 1993.

[95] K. Fujita, P. Landis, B. K. McNeil, and C. P. Pavlovich, “Serial Prostate Biopsies are Associated With an Increased Risk of Erectile Dysfunction in Men With Prostate Cancer on Active Surveillance,” *J. Urol.*, vol. 182, no. 6, pp. 2664–2669, 2009.

[96] B. Ahn, E. I. S. Lorenzo, K. H. Rha, H. J. Kim, and J. Kim, “Robotic Palpation-Based Mechanical Property Mapping for Diagnosis of Prostate Cancer,” *J. Endourol.*, vol. 25, no. 5, pp. 851–857, 2011.

[97] B. Ahn, H. Lee, Y. Kim, and J. Kim, “Robotic system with sweeping palpation andneedle biopsy for prostate cancer diagnosis,” *Int J Med Robot.*, vol. 10, no. 3, pp. 356–367, 2013.

[98] J. Li, H. Liu, M. Brown, P. Kumar, B. J. Challacombe, A. Chandra, G. Rottenberg, L. D. Seneviratne, K. Althoefer, and P. Dasgupta, “Ex vivo study of prostate cancer localization using rolling mechanical imaging towards minimally invasive surgery,” *Med. Eng. Phys.*, vol. 43, pp. 112–117, 2017.

[99] M. Beccani, C. Di Natali, L. J. Sliker, J. A. Schoen, M. E. Rentschler, and P. Valdastri, “Wireless tissue palpation for intraoperative detection of lumps in the soft tissue,” *IEEE Trans. Biomed. Eng.*, vol. 61, no. 2, pp. 353–361, 2014.

[100] J. C. Gwilliam, Z. Pezzementi, E. Jantho, A. M. Okamura, and S. Hsiao, “Human vs. robotic tactile sensing: Detecting lumps in soft tissue,” *2010 IEEE Haptics Symp. HAPTICS 2010*, pp. 21–28, 2010.

[101] L. A. Baumgart, G. J. Gerling, and E. J. Bass, “Characterizing the range of simulated prostate abnormalities palpable by digital rectal examination,” *Cancer Epidemiol.*, vol. 34, no. 1, pp. 79–84, 2010.

[102] S. Jeon and M. Harders, “Haptic tumor augmentation: Exploring multi-point interaction,” *IEEE Trans. Haptics*, vol. 7, no. 4, pp. 477–485, 2014.

[103] J. Palacio-Torralba, D. W. Good, G. D. Stewart, S. A. McNeill, R. L. Reuben, and Y. Chen, “A novel method for rapid and quantitative mechanical assessment of soft tissue for diagnostic purposes: A computational study,” *Int. j. numer. method. biomed. eng.*, vol. 34, no. 2, pp. 1–12, 2018.

[104] J. Palacio-Torralba, S. Hammer, D. W. Good, S. A. McNeill, G. D. Stewart, R. L. Reuben, and Y. Chen, “Quantitative diagnostics of soft tissue through viscoelastic characterization using time-based instrumented palpation,” *J. Mech. Behav. Biomed. Mater.*, vol. 41, pp. 149–160, 2015.

[105] M. Prabhune, G. Belge, A. Dotzauer, J. Bullerdiek, and M. Radmacher, “Comparison of mechanical properties of normal and malignant thyroid cells,” *Micron*, vol. 43, no. 12, pp. 1267–1272, 2012.

[106] B. Ahn and J. Kim, “Efficient soft tissue characterization under large deformations in medical simulations,” *Int. J. Precis. Eng. Manuf.*, vol. 10, no. 4, pp. 115–121, 2009.

[107] M. Ariza-Gracia, Ortillés, J. Cristóbal, J. F. Rodríguez Matas, and B. Calvo, “A numerical-experimental protocol to characterize corneal tissue with an application to predict astigmatic keratotomy surgery,” *J. Mech. Behav. Biomed. Mater.*, vol. 74, no. February, pp. 304–314, 2017.

[108] F. Martínez-Martínez, M. J. Rupérez, J. D. Martín-Guerrero, C. Monserrat, M. A. Lago, E. Pareja, S. Brugger, and R. López-Andújar, "Estimation of the elastic parameters of human liver biomechanical models by means of medical images and evolutionary computation," *Comput. Methods Programs Biomed.*, vol. 111, no. 3, pp. 537–549, 2013.

[109] M. P. Ottensmeyer, A. E. Kerdok, R. D. Howe, and S. L. Dawson, "The Effects of Testing Environment on the Viscoelastic Properties of Soft Tissues," in *Proceeding of Medical Simulation: International Symposium - ISMS 2004, Cambridge, MA*, 1887, vol. 3078, pp. 195–196.

[110] E. Samur, M. Sedef, C. Basdogan, L. Avtan, and O. Duzgun, "A robotic indenter for minimally invasive measurement and characterization of soft tissue response," in *Proceedings of the International Symposium on Medical Simulation*, 2000, pp. 9–18.

[111] J. Kim, B. Ahn, S. De, and M. A. Srinivasan, "An efficient soft tissue characterization algorithm from in vivo indentation experiments for medical simulation," *Int J Med Robot*, vol. 4(3), pp. 277–285, 2008.

[112] M. Kauer, V. Vuskovic, J. Dual, G. Szekely, and M. Bajka, "Inverse finite element characterization of soft tissues," *Med. Image Anal.*, vol. 6, pp. 275–287, 2002.

[113] A. Nava, E. Mazza, M. Furrer, P. Villiger, and W. H. Reinhart, "In vivo mechanical characterization of human liver," *Med. Image Anal.*, vol. 12, no. 2, pp. 203–216, 2008.

[114] S. R. Mousavi, H. Wang, S. M. Hesabgar, T. J. Scholl, and A. Samani, "A novel shape-similarity-based elastography technique for prostate cancer assessment," *Med. Phys.*, vol. 42, no. 9, pp. 5110–5119, 2015.

[115] A. Samani, J. Zubovits, and D. Plewes, "Elastic moduli of normal and pathological human breast tissues: An inversion-technique-based investigation of 169 samples," *Phys. Med. Biol.*, vol. 52, no. 6, pp. 1565–1576, 2007.

[116] J. J. O'Hagan and A. Samani, "Measurement of the hyperelastic properties of tissue slices with tumour inclusion," *Phys. Med. Biol.*, vol. 53, no. 24, pp. 7087–7106, 2008.

[117] B. Ahn, Y. Kim, C. K. Oh, and J. Kim, "Robotic palpation and mechanical property characterization for abnormal tissue localization," *Med. Biol. Eng. Comput.*, vol. 50, no. 9, pp. 961–971, 2012.

[118] K. Sangpradit, H. Liu, P. Dasgupta, K. Althoefer, and L. D. Seneviratne, "Finite-element modeling of soft tissue rolling indentation," *IEEE Trans. Biomed. Eng.*, vol. 58, no. 12, pp. 3319–3327, 2011.

[119] H. Liu, K. Sangpradit, M. Li, P. Dasgupta, K. Althoefer, and L. D. Seneviratne, "Inverse finite-element modeling for tissue parameter identification using a rolling indentation probe," *Med. Biol. Eng. Comput.*, vol. 52, no. 1, pp. 17–28, 2014.

[120] B. Ahn and J. Kim, "Measurement and characterization of soft tissue behavior with surface deformation and force response under large deformations," *Med. Image Anal.*, vol. 14, no. 2, pp. 138–148, 2010.

[121] V. Jalkanen, B. M. Andersson, A. Bergh, B. Ljungberg, and O. A. Lindahl,

"Indentation loading response of a resonance sensor-discriminating prostate cancer and normal tissue," *J. Med. Eng. Technol.*, vol. 37, no. 7, pp. 416–423, 2013.

[122] A. L. Trejos, J. Jayender, M. T. Perri, M. D. Naish, R. V. Patel, and R. A. Malthaner, "Robot-assisted tactile sensing for minimally invasive tumor localization," *Int. J. Rob. Res.*, vol. 28, no. 9, pp. 1118–1133, 2009.

[123] G. L. McCreey, A. L. Trejos, M. D. Naish, R. V. Patel, and R. A. Malthaner, "Feasibility of locating tumours in lung via kinaesthetic feedback," *Int. J. Med. Robot. Comput. Assist. Surg.*, vol. 4, pp. 58–68, 2008.

[124] H. Xie, H. Liu, L. D. Seneviratne, and K. Althoefer, "An optical tactile array probe head for tissue palpation during minimally invasive surgery," *IEEE Sens. J.*, vol. 14, no. 9, pp. 3283–3291, 2014.

[125] M. Li, S. Luo, T. Nanayakkara, L. D. Seneviratne, P. Dasgupta, and K. Althoefer, "Multi-fingered haptic palpation using pneumatic feedback actuators," *Sensors Actuators, A Phys.*, vol. 218, pp. 132–141, 2014.

[126] V. Egorov, S. Ayrapetyan, and A. P. Sarvazyan, "Prostate mechanical imaging: 3-D image composition and feature calculations," *IEEE Trans. Med. Imaging*, vol. 25, no. 10, pp. 1329–1340, 2006.

[127] Y. Murayama, M. Haruta, Y. Hatakeyama, T. Shiina, H. Sakuma, S. Takenoshita, S. Omata, and C. E. Constantinou, "Development of a new instrument for examination of stiffness in the breast using haptic sensor technology," *Sensors Actuators, A Phys.*, vol. 143, no. 2, pp. 430–438, 2008.

[128] M. Beccani, C. Di Natali, C. E. Benjamin, C. S. Bell, N. E. Hall, and P. Valdastri, "Wireless tissue palpation: Head characterization to improve tumor detection in soft tissue," *Sensors Actuators, A Phys.*, vol. 223, pp. 180–190, 2015.

[129] B. Li, Y. Shi, A. Fontecchio, and Y. Visell, "Mechanical Imaging of Soft Tissues with a Highly Compliant Tactile Sensing Array," *IEEE Trans. Biomed. Eng.*, vol. 65, no. 3, pp. 687–697, 2018.

[130] C. Van Nguyen and R. F. Saraf, "Tactile imaging of an imbedded palpable structure for breast cancer screening," *ACS Appl. Mater. Interfaces*, vol. 6, no. 18, pp. 16368–16374, 2014.

[131] Y. Kim, B. Ahn, Y. Na, T. Shin, K. Rha, and J. Kim, "Digital rectal examination in a simulated environment using sweeping palpation and mechanical localization," *Int. J. Precis. Eng. Manuf.*, vol. 15, no. 1, pp. 169–175, 2014.

[132] P. L. Yen, D. R. Chen, K. T. Yeh, and P. Y. Chu, "Lateral exploration strategy for differentiating the stiffness ratio of an inclusion in soft tissue," *Med. Eng. Phys.*, vol. 30, no. 8, pp. 1013–1019, 2008.

[133] J. H. Lee and C. H. Won, "The tactile sensation imaging system for embedded lesion characterization," *IEEE J. Biomed. Heal. Informatics*, vol. 17, no. 2, pp. 452–458, 2013.

[134] K. A. Nichols and A. M. Okamura, "Methods to Segment Hard Inclusions in Soft Tissue During Autonomous Robotic Palpation," *IEEE Trans. Robot.*, vol. 31, no. 2, pp. 344–354, 2015.

[135] M. Li, H. Liu, A. Jiang, L. D. Seneviratne, P. Dasgupta, K. Althoefer, and H. Wurdemann, "Intra-operative tumour localisation in robot-assisted minimally invasive surgery: A review," *Proc. Inst. Mech. Eng. Part H J. Eng. Med.*, vol. 228, no. 5, pp. 509–522, 2014.

[136] K. Miller, "Method of testing very soft biological tissues in compression," *J. Biomech.*, vol. 38, no. 1, pp. 153–158, 2005.

[137] D. W. Marquardt, "Algorithm for least-squares estimation of nonlinear parameters," *J. Soc. Ind. Appl. Math.*, vol. 11, no. 2, 1963.

[138] M. I. A. Lourakis and A. A. Argyros, "Is Levenberg-Marquardt the most efficient optimization algorithm for implementing bundle adjustment ?," in *IEEE International Conference on Computer Vision*, 2005.

[139] K. Madsen, H. B. Nielsen, and O. Tingleff, *Methods for non-linear least squares problems*, vol. 2. Copenhagen, Denmark, 2004.

[140] S. R. Mousavi, A. Sadeghi-Naini, G. J. Czarnota, and A. Samani, "Towards clinical prostate ultrasound elastography using full inversion approach," *Med. Phys.*, vol. 41, no. 3, 2014.

[141] T. A. Stamey, J. E. McNeal, C. M. Yemoto, B. M. Sigal, and I. M. Johnstone, "Biological determinants of cancer progression in men with prostate cancer," *J. Am. Med. Assoc.*, vol. 281, no. 15, pp. 1395–1400, 1999.

[142] M. A. J. Cox, N. J. B. Driessen, R. A. Boerboom, C. V. C. Bouten, and F. P. T. Baaijens, "Mechanical characterization of anisotropic planar biological soft tissues using finite indentation: Experimental feasibility," *J. Biomech.*, vol. 41, no. 2, pp. 422–429, 2008.

[143] G. Torlakovic, V. K. Grover, and E. Torlakovic, "Easy method of assessing volume of prostate adenocarcinoma from estimated tumor area: using prostate tissue density to bridge gap between percentage involvement and tumor volume.," *Croat. Med. J.*, vol. 46, no. 3, pp. 423–428, 2005.

[144] D. Beyersdorff, M. Taupitz, B. Winkelmann, T. Fischer, S. Lenk, S. A. Loening, and B. Hamm, "Patients with a History of Elevated Prostate-Specific Antigen Levels and Negative Transrectal US–guided Quadrant or Sextant Biopsy Results: Value of MR Imaging," *Radiology*, vol. 224, no. 3, pp. 701–706, 2002.

[145] G. Antoch, F. M. Vogt, L. S. Freudenberg, F. Nazaradeh, S. C. Goehde, J. Barkhausen, G. Dahmen, Andreas Bockisch, Jorg F. Debatin, and S. G. Ruehm, "Whole-Body Dual-Modality PET/CT and Whole-Body MRI for Tumor Staging in Oncology," *Am. Med. Assoc.*, vol. 290, no. 24, pp. 3199–3206, 2003.

[146] T. Franiel, L. Lüdemann, B. Rudolph, H. Rehbein, A. Staack, M. Taupitz, D. Prochnow, and D. Beyersdorff, "Evaluation of normal prostate tissue, chronic prostatitis, and prostate cancer by quantitative perfusion analysis using a dynamic contrast-enhanced inversion-prepared dual-contrast gradient echo sequence," *Invest. Radiol.*, vol. 43, no. 7, pp. 481–487, 2008.

[147] J. Xu, P. A. Humphrey, A. S. Kibel, A. Z. Snyder, V. R. Narra, J. J. H. Ackerman, and S. K. Song, "Magnetic resonance diffusion characteristics of histologically defined prostate cancer in humans," *Magn. Reson. Med.*, vol. 61, no. 4, pp. 842–

850, 2009.

[148] I. F. Lissbrant, P. Stattin, J. E. Damber, and A. Bergh, “Vascular density is a predictor of cancer-specific survival in prostatic carcinoma,” *Prostate*, vol. 33, no. 1, pp. 38–45, 1997.

[149] C. M. Groh, M. E. Hubbard, P. F. Jones, P. M. Loadman, N. Periasamy, B. D. Sleeman, S. W. Smye, C. J. Twelves, and R. M. Phillips, “Mathematical and computational models of drug transport in tumours,” *J. R. Soc. Interface*, vol. 11, no. 94, 2014.

[150] A. Quarteroni, A. Manzoni, and C. Vergara, “The cardiovascular system: Mathematical modelling, numerical algorithms and clinical applications,” *Acta Numer.*, vol. 26, pp. 365–590, 2017.